Angular momentum transport: from magnon currents to orbital currents

Dissertation

for the purpose for obtaining the degree of Doctor

at the University of the Basque Country

by

Montserrat Xochitl Aguilar Pujol

performed under the supervision of

Prof. Dr. Fèlix Casanova & Prof. Dr. Luis. E. Hueso

2025

To Nathan

Abstract

From the first experiments in the seventeenth century to understand electricity to the present day, where devices surround us at every moment, the charge of the electron has long been at the heart of electronics. Electronics exploits this degree of freedom to transport and store information. To achieve this, chips have been continuously scaled down, allowing an increase in transistor density, the main components of devices, within the same area. However, this miniaturization has led to challenges such as quantum effects and energy dissipation. To reduce energy consumption and overcome the limitations of scaling, new technologies such as spintronics, spin-orbitronics, or most recently orbitronics have emerged to complement or replace conventional charge-based CMOS technology. These fields exploit the spin or orbital angular momentum of the electron instead of, or in addition to, its charge.

Spintronics exploits the flow of spin angular momentum, which can be carried by moving electrons in a non-magnetic conductor or by collective excitations of magnetization of localized electrons (magnons) in a magnetic material. In contrast, orbitronics operates with the flow of orbital angular momentum. All of these can be integrated with conventional electronics. A key mechanism enabling this integration is the spin Hall effect (SHE), which converts a charge current into a spin current. Similarly, the orbital Hall effect (OHE) converts a charge current into an orbital current. These two effects form the basis of this thesis, serving as fundamental tools to investigate spin- and orbital-related phenomena.

In this context, this thesis explores both the transport of spin and orbital angular momentum. In the first part, Chapters 4 and 5, we investigate the propagation of magnon spin currents in a pure ferromagnetic insulator, providing insights into a textbook ferromagnetic insulator: europium sulphide (EuS). The SHE is employed to generate and detect spin currents, providing a robust platform to probe magnon transport. We demonstrate the excitation and transport of thermally-induced magnons and extract the magnon diffusion length in this system, in contrast to previously explored ferrimagnetic and antiferromagnetic materials. Furthermore, we study the low-temperature magnetic

dynamics of EuS, largely unexplored and reported only in bulk crystals. Ferromagnetic resonance measurements on polycrystalline and epitaxial EuS thin films reveal a Gilbert damping of 10^{-3} for temperatures below 10 K, comparable to that of permalloy films.

In the second part, Chapter 6, we study the large Hanle magnetoresistance in Vanadium, a 3d metal, with weak spin-orbit coupling, and reveal its orbital origin. This phenomenon is intimately connected to the OHE, which mediates the conversion between charge and orbital currents. Using magnetotransport and ferromagnetic resonance measurements, we determine the key orbital transport parameters, providing a comprehensive characterization of orbital current propagation in this material. These results highlight the role of the orbital degree of freedom in metals and open new possibilities for orbitronics.

Overall, this thesis advances our understanding of spin and orbital transport, providing a solid foundation for future developments in spintronics and orbitronics.

Resumen

Desde los primeros experimentos en el siglo XVII para comprender la electricidad hasta la actualidad, donde los dispositivos nos rodean en todo momento, la carga del electrón ha estado durante mucho tiempo en el corazón de la electrónica. La electrónica explota este grado de libertad para transportar y almacenar información. Para lograrlo, los chips se han ido reduciendo continuamente de tamaño, permitiendo un aumento de la densidad del transistor, el componente principal de los dispositivos, dentro de una misma área. Sin embargo, esta miniaturización ha generado desafíos como los efectos cuánticos y la disipación de energía. Para reducir el consumo energético y superar las limitaciones de la miniaturización, han surgido nuevas tecnologías como la espintrónica (spintronics), la spin-orbitrónica (spin-orbitronics) o, más recientemente, la orbitrónica (orbitronics), que complementan o sustituyen a la tecnología CMOS convencional basada en la carga. Estos campos aprovechan el spin o momento angular orbital del electrón en lugar de, o además de, su carga.

La espitrónica explota el flujo de momento angular de espín, que puede ser transportado por electrones en movimiento en un conductor no magnético o por excitaciones colectivas de la magnetización de electrones localizados (magnones) en un material magnético. En cambio, la orbitrónica opera con el flujo de momento angular orbital. Todos estos enfoques pueden integrarse con la electrónica convencional. Un mecanismo clave que permite esta integración es el efecto Hall de espín (SHE), que convierte una corriente de carga en una corriente de espín. De manera similar, el efecto Hall orbital (OHE) convierte una corriente de carga en una corriente orbital. Estos dos efectos constituyen la base de esta tesis, sirviendo como herramientas fundamentales para investigar fenómenos relacionados con el espín y con el momento angular orbital.

En este contexto, esta tesis explora tanto el transporte de momento angular de espín como de momento angular orbital. En la primera parte, capítulos 4 y 5, investigamos la propagación de corrientes de espín de magnones en un aislante ferromagnético puro, proporcionando información sobre un aislante ferromagnético de referencia: el sulfuro de europio (EuS). El SHE se utiliza para generar y detectar corrientes

de espín, ofreciendo una plataforma robusta para estudiar el transporte de magnones. Demostramos la excitación y el transporte de magnones inducidos térmicamente y extraemos la longitud de difusión de magnones en este sistema, en contraste con los materiales ferrimagnéticos y antiferromagnéticos explorados previamente. Además, estudiamos la dinámica magnética a bajas temperaturas del EuS, en gran medida inexploradas y reportada únicamente en cristales volumétricos. Las medidas de resonancia ferromagnética en películas delgadas policristalinas y epitaxiales de EuS revelan un amortiguamiento de Gilbert del orden de 10^{-3} para temperaturas por debajo de 10 K, comparable al de las películas de permaloy.

En la segunda parte, capítulo 6, estudiamos la gran magnetorresistencia de Hanle en el vanadio, un metal 3d con acoplamiento espín-órbita débil, y revelamos su origen orbital. Este fenómeno está íntimamente ligado al OHE, que media la conversión entre corrientes de carga y corrientes orbitales. Mediante medidas de magnetotransporte y resonancia ferromagnética, determinamos los parámetros clave del transporte orbital, proporcionando una caracterización exhaustiva de la propagación de corrientes orbitales en este material. Estos resultados ponen de relieve el papel del grado de libertad orbital en los metales y abren nuevas posibilidades para la orbitrónica.

En conjunto, esta tesis amplía nuestra comprensión del transporte de espín y de orbital, proporcionando una base sólida para futuros desarrollos en espintrónica y orbitrónica.

Table of contents

Chapter 1 Introduction 1
Chapter 2 From spintronics to orbitronics 8
2.1 Spintronics 8
2.1.1 Charge and spin currents 9
2.1.2 Generation and detection of pure spin currents 13
2.1.3 Diffusion of spin currents 16
2.1.4 Spin Hall magnetoresistance 17
2.1.5 Hanle magnetoresistance 20
2.1.6 Spin Seebeck effect 24
2.1.7 Magnon transport: electrical and thermal (SSE) generation 25
2.1.8 Spin dynamics 28
2.2 Orbitronics 34
2.2.1 Orbital currents 34
2.2.2 Generation and detection of orbital currents 36
2.2.3 Experimental evidence of orbital currents 39
2.2.4 Orbital Hall magnetoresistance 43
2.2.5 Orbital Hanle magnetoresistance 43
Chapter 3 Experimental techniques 47
3.1 Device fabrication 47
3.1.1 Cleaning of the substrates 48
3.1.2 Lithography 48
3.1.3 Thin film deposition 50
3.1.4 Resist and thin film removal 51

3.2 Characterization techniques 52
3.2.1 X-ray characterization 52
3.2.2 Electrical measurements 54
3.2.3 Ferromagnetic resonance measurements 58
Chapter 4 Magnon currents excited by the spin Seebeck effect in ferromagnetic EuS thin films 60
4.1 Introduction 60
4.2 Experimental details 62
4.3 Results and discussion 62
4.3.1 Angle dependence of the electrical and thermal response 65
4.4 Conclusions 72
4.5 Appendices 73
4.5.1 Longitudinal magnetoresistance measurements 73
4.5.2 Current-dependent measurements 74
4.5.3 Electrical excitation of magnons 77
4.5.4 Thermal excitation of magnons 78
4.5.5 Magnetic characterization 79
Chapter 5 Gilbert damping in EuS thin films by ferromagnetic resonance spectroscopy 80
5.1 Introduction 80
5.2 Experimental details 82
5.3 Results and discussion 83
5.4 Conclusions 90
5.5 Appendices 91
5.5.1 Out of plane measurements 91
5.5.2 Magnetic characterization of EuS without capping layer 92

Chapter 6 Orbital Hall conductivity and orbital diffusion length of Vanadium thin films by Hanle magnetoresistance 94
6.1 Introduction 94
6.2 Methods 96
6.3 Results and discussion 96
6.4 Conclusions 106
6.5 Appendices 106
6.5.1 Resistivity of V thin films 106
6.5.2 Longitudinal magnetoresistance measurements 107
6.5.3 Transverse magnetoresistance measurements 108
6.5.4 Hanle magnetoresistance of high resistive samples 109
6.5.5 Orbital transport parameters of high resistivity samples 110
6.5.6 Magnetoresistance measurements on YIG 112
6.5.7 Structural characterization of V samples 113
6.5.8 Orbital transport parameters of 8-nm-thick low-resistivity sample 114
Chapter 7 Conclusions and outlook 116
Bibliography 120
List of Publications 142

Chapter 1
Introduction

The first experiments to understand the basic principles of electricity started in the seventeenth century, but it was in 1891 when G. J. Stoney suggested the name "electron" for a hypothetical small unit of electric charge [1]. The electron, one of the elementary particles that form the atoms, was discovered six years later by Professor J.J. Thomson, who determined its charge to mass ratio. The investigation and development of electronic devices were based on the electron most known intrinsic property, the electric charge, whose value corresponds to the negative elementary electric charge ($-e$). It was the beginning of the age of electronics, based on the control and manipulation of electrons in movement. This was achieved during the early 20th century by means of the vacuum tube, a glass tube which contained electrodes in near-vacuum, enabling the development of electronic devices. Vacuum tubes were used in early telecommunication systems, radios and televisions.

Later, with the discovery of transistors in the mid-20th century, followed by the invention of the integrated circuit, electronics experienced a breakneck development. Transistors were smaller, more efficient and more reliable than vacuum tubes, enabling the miniaturization of electronic devices. Of utmost importance was the complementary metal-oxide-semiconductor (CMOS) integrated circuit, which included metal-oxide-semiconductor field effect transistors (MOSFET), announced in 1963 [2,3]. In 1965, G. E. Moore realized that the number of components per chip of an integrated circuit increased by a factor of two every year [4], which later updated to a factor of two every two years [5]. This trend, known as Moore's law, comes from the combination of shrinking the size of individual transistors and increasing chip area. Throughout all this time, industry has been looking for higher performance, cheaper manufacturing, and miniaturization. As a result, microprocessors, firstly introduced by Intel in the early 1970s, now incorporate billions of transistors in a single device.

Microprocessors have revolutionized information and communication technologies (ICTs) and, therefore, our society: we can find

microprocessors in our daily life in a variety of devices including smartphones, laptops, industrial apparatus and space-based equipment. Although microprocessors continuously improve, energy efficiency became the focal point after the 1990s. To reduce energy consumption, techniques such as dynamic voltage, frequency scaling and power gating were implemented, contributing to environmental sustainability [6,7]. However, the shrinkage of transistors, that nowadays is at sub-10-nanometre scale, encounters barriers like leakage currents at the gate dielectric due to quantum tunnelling, which increase idle power usage, or increasing heat generation, requiring more advanced cooling devices [8]. Although electronics and ICTs have transformed our lives, the physical limitations of the current CMOS technology make Moore's law more and more difficult to maintain. Therefore, we are at the limit of continuing using the same technology. Of particular importance, we need to find new ways to make ICTs more efficient. In this regard, spintronics, spin-orbitronics, and more recently orbitronics have arisen as new possibilities to replace or complement conventional charge-based CMOS technology [9–11].

To understand the basics of spintronics and orbitronics, we need to consider another property of electrons, the angular momentum, which has two distinct sources, the orbital $\boldsymbol{L}$ and the spin $\boldsymbol{S}$, sometimes referred as extrinsic and intrinsic angular momentum, respectively. The orbital angular momentum is a characteristic property of the rotational motion of an electron around the nucleus (see Figure 1.1). Classically, an electron circulating in its orbit, of radius r and with velocity v, is equivalent to a current loop where the current direction I is opposite to the sense of circulation because of the negative electronic charge. According to Ampère, the elementary magnetic moment m resulting from the circulating current can be represented by $m = IA$, where A is the area of the current loop and the current is $I = -e/T$, where $T = 2\pi r/v$ is the period of rotation. The orbital magnetic moment is then $\boldsymbol{m_L} = -\frac{1}{2}e\boldsymbol{r} \times \boldsymbol{v}$ which, in terms of the angular momentum, $\boldsymbol{L} = m_e\boldsymbol{r} \times \boldsymbol{v}$, where m_e is the mass of the electron, results:

$$\boldsymbol{m_L} = -\frac{e}{2m_e}\boldsymbol{L} \tag{1.1}$$

In Quantum Mechanics, the orbital angular momentum is quantized as $L = \sqrt{l(l+1)}\hbar$, where l is the orbital quantum number and $\hbar$ is the Planck´s constant h divided by 2π. Then, it is convenient to express the quantum orbital angular momentum as:

$$\boldsymbol{m_L} = -\frac{g_L \mu_B}{\hbar}\boldsymbol{L} \tag{1.2}$$

where g_L is the orbital g-factor (the ratio of the magnetic moment of a particle to that expected classically, i.e., Eq. (1.1), that for the electron is 1), and $\mu_B = e\hbar/(2m_e)$ is the Bohr magneton.

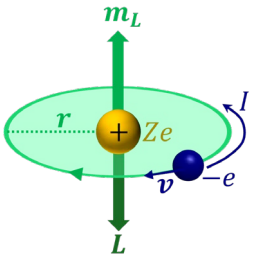

Figure 1.1. Classically, an electron with charge -e and velocity v orbits a nucleus with positive charge Ze forming a current loop. The orbital motion creates an orbital angular momentum $\boldsymbol{L}$ with the orbital moment $\boldsymbol{m_L}$ pointing in the opposite direction.

Moreover, the electron has a spin angular momentum $\boldsymbol{S}$, which does not have a classical equivalent. The spin is a universal property of the electron in all states of matter at all temperatures. It was postulated in 1925 by G. Uhlenbeck and S. Goudsmit [12]. Electrons, like protons and neutrons, are fermions. Such particles have half-integer values of spin and obey the Pauli exclusion principle. The quantum spin magnetic moment $\boldsymbol{m_s}$ due to the electron spin is equal to:

$$\boldsymbol{m_s} = -\frac{g_S e}{2m_e}\boldsymbol{S} = -\frac{g_S \mu_B}{\hbar}\boldsymbol{S} \tag{1.3}$$

where g_S is the spin g-factor that for the electron is close to 2. The spin possess discrete quantized values presented as the projection along an axis, usually the z-axis, that is $S_z = \hbar m_s$ being m_s the magnetic quantum number that can take two discrete values $m_s = \pm 1/2$, so

there are only two possible spin angular momentum states, generally named spin-up (↑) and spin down (↓).

Moreover, the electron spin and orbital momentum can couple by spin-orbit coupling (SOC), generating an important source of spin dynamics. To understand this coupling, we can take the electron's frame of reference and assume the electron to be at the centre with the nucleus Ze circling around it with a given velocity v (Figure 1.2a). The motion is equivalent to a current which creates a magnetic field B_{soc}:

$$B_{soc} = \frac{\mu_0 Zev}{4\pi r^2} \tag{1.4}$$

being μ_0 the permeability of free space. B_{soc} interacts with the electron spin with an energy $E_{soc} = -\mu_B B_{soc}$. E_{soc} can be rewritten in terms of the Bohr radius a_0 by using $r \simeq a_0/Z$, and $m_e vr \approx \hbar$ giving:

$$E_{soc} \approx -\frac{\mu_0 \mu_B^2 Z^4}{4\pi a_0^3} \tag{1.5}$$

According to this simplified picture that leads to the equation, the SOC scales as Z^4, indicating that it becomes more important for heavy elements. Then, it is expected to be smaller for 3*d* transition metals and higher for 4*d* and, especially, 5*d* transition metals. In fact, the 3*d* series follow quite well the expected Z^4 behaviour (see Figure 1.2b). However, 4*d* elements in the left part of the periodic table have lower SOC than 3*d* elements in the right part, even though for each column of the periodic table the 4*d* element has stronger SOC than the corresponding 3*d* element, which accounts for a more complicated connection of the SOC strength. In fact, the SOC strength for the outermost electrons increases much more slowly as Z^2, which agrees with the Landau-Lifshitz scaling (see Figure 1.2b) [13].

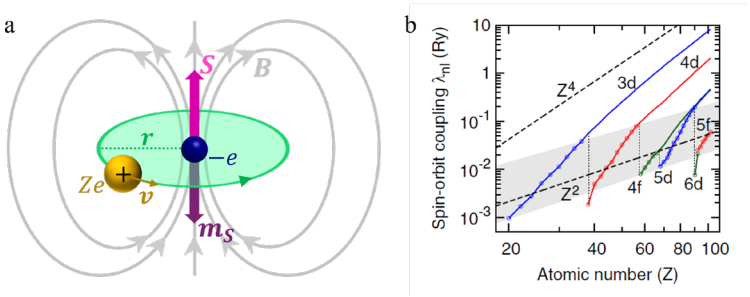

Figure 1.2. a) Spin-orbit coupling from the viewpoint of the electron. The nucleus is orbiting around the electron and the resulting orbital magnetic moment interacts with the spin of the electron, leading to the spin-orbit coupling. b) Spin-orbit coupling strength λ_{nl} for atoms as a function of their atomic number Z. Calculated results using the Hartree-Fock method (solid lines) are compared to the hydrogenic Z^4 dependence (upper dashed line) which is computed for the 3*d* series. For the outermost electrons (indicated by the circles and the shaded area), the spin-orbit coupling increases much more slowly, roughly following the Landau-Lifshitz Z^2 scaling (lower dashed line), although within each series, the dependence remains closer to Z^4. Figure adapted from [13].

The correct version of the SOC, resulting from a relativistic calculation, is represented by the Hamiltonian:

$$\mathcal{H}_{soc} = \lambda_{nl} \boldsymbol{L} \cdot \boldsymbol{S} \tag{1.6}$$

where λ_{nl} is the strength of the SOC, and $\boldsymbol{L}$ and $\boldsymbol{S}$ are operators.

Up to now, we have considered that we have only one electron, but every solid contains a very large number of electrons. The attractive electrostatic interaction between the negative charges of the electrons and the positive charge of the nuclei is responsible for the cohesion in solids. There, the electrons are arranged in energy bands separated by regions in energy for which no wavelike electron orbitals exist (energy gaps) [14]. Moreover, in solids, electrons are the main source of magnetic moments. The nucleus also has a small magnetic moment, but it is insignificant compared to that of the electrons, and it does not affect the gross magnetic properties. The microscopic theory of magnetism is based on the quantum mechanics of electronic angular momentum, which means that it is based on the orbital motion and spin as well as on the SOC.

Given the fact that electrons possess not only charge but also angular momentum, new ways to exploit this property gave rise to a new generation of electronics named spintronics, which takes advantage of the flow of spin (see Figure 1.3b) [10,15]. Later, several subfields emerged. One direction focuses on the collective excitations of spins leading to the development of magnonics (also illustrated in Figure 1.3b) [16]. Another approach to manipulating spin involves exploiting the SOC, which lead to the evolution of spintronics into spin-orbitronics [17]. Finally, it has very recently been found that the orbital angular momentum can be directly exploited in a similar way as the spin, giving rise to the emerging field of orbitronics (see Figure 1.3c) [18].

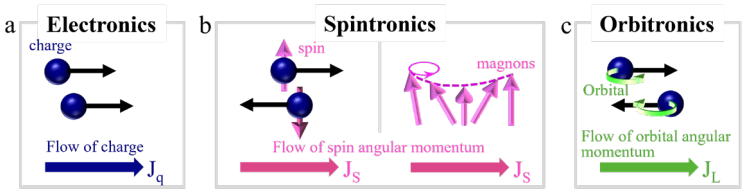

Figure 1.3. a) Electronics is based on the transport and manipulation of the electron charge. b) Spintronics is based on the transport and manipulation of the spin angular momentum of the electron, which can be realized by conduction electrons or by quasiparticles like magnons. c) Orbitronics is based on the transport and manipulation of the orbital angular momentum of the electron.

The aim of this thesis is to study the spin and orbital transport in metallic and insulating systems:

Chapter 1 (*Introduction*) gives a brief overview of the evolution of electronics since its birth to the present day. Although the charge of the electron was the main property used in electronics, over time and increased demand from the technological industry and society new fields arise, such as spintronics and orbitronics.

Chapter 2 (*From spintronics to orbitronics*) provides a theoretical background of spin and orbital physics, introducing concepts such as spin and orbital injection, transport and detection.

Chapter 3 (*Experimental techniques*) gives details about the techniques used for the fabrication, characterization and analysis of the spintronic and orbitronic devices used in this thesis.

The following three chapters present different approaches to study spin and orbital transport in various systems. First, **Chapters 4** and **5** focus on magnetic insulators, where magnon spin currents can propagate. **Chapter 4** (*Magnon currents excited by the spin Seebeck effect in ferromagnetic EuS thin films*) shows how magnon spin currents propagate in a pure ferromagnetic insulator. **Chapter 5** (*Gilbert damping in EuS thin films by ferromagnetic resonance spectroscopy*) explores further spin dynamics in EuS thin films with different thicknesses and crystallinity. **Chapter 6** (*Orbital Hall conductivity and orbital diffusion length of Vanadium thin films by Hanle magnetoresistance*) investigates Vanadium, a transition metal with weak SOC, where the orbital Hall conductivity is expected to be orders of magnitude higher than the spin Hall conductivity.

Chapter 7 (*Conclusions and outlook*) summarizes the main results of this thesis.

Chapter 2
From spintronics to orbitronics

2.1 Spintronics

The starting point of spintronics is that, in an electrical conductor, charge carriers possess a charge and a spin degree of freedom which can be used not only to transport charge in the form of an electrical current, but also to transport spin angular momentum in the form of a spin current. In this case, the spin current can be viewed as the flow of spin angular momentum mediated by electrons. Precisely, the discovery of giant magnetoresistance (GMR) exploited the influence of the spin in the mobility of the electrons through a current flowing between two ferromagnetic elements separated by a thin non-magnetic spacer (see Figure 2.1) [19,20], starting the era of spintronics. The phenomenon of GMR was implemented in magnetoresistive read heads on hard disk drives (HDDs) that detect the sign and magnitude of the magnetic fields above the disk with high resolution [21]. The increased sensitivity resulted in a quick growth of the storage density in HDDs, and in 2007 Albert Fert and Peter Grunberg received the Nobel prize in Physics for their discovery, independently, of the GMR.

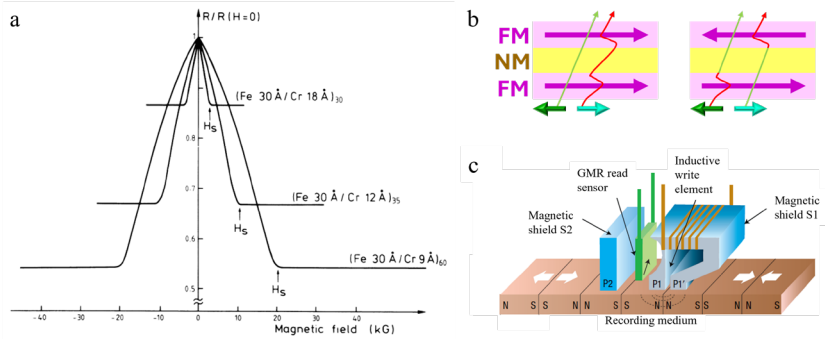

Figure 2.1. a) Discovery of GMR in Fe/Cr(001) multilayers (Fig. taken from [19]). b) Schematic of the mechanism of the GMR. In the parallel configuration (left), the electrons with one of the spin directions can go easily through all the magnetic layers and this leads to a low resistance. In the antiparallel configuration (right), the electrons of each spin channel are slowed down at one of the magnetic layers and the resistance is high. c) Schematic of a GMR read head introduced for HDDs (Fig. adapted from [15]).

Whereas spintronics was first used to read information being stored in HDDs, later other possibilities arose, such as magnetic random-access memories (MRAM) [22], which instead uses tunnel magnetoresistance, or spin-based logic [9–11,23]. Furthermore, the intensive investigation of spin currents in order to look for higher information processing speeds, denser information storage and lower power consumption opened new ways to propagate spin currents such as magnon-mediated spin currents in magnetic insulators [24–26]. In insulators, spin currents propagate with significantly reduced dissipation since there are no conduction electrons dissipating heat.

2.1.1 Charge and spin currents

To start with, we consider charge currents. When an electric field $\boldsymbol{E}$ is applied in a conductor, a force $e\boldsymbol{E}$ is exerted on the conduction electrons, generating an electron drift motion with an associated density charge current $\boldsymbol{J_{drift}}$ given by:

$$\boldsymbol{J_{drift}} = \sigma_e \boldsymbol{E} \,, \tag{2.1}$$

where σ_e is the electrical conductivity. This is the well-known Ohm's law. Moreover, electrons can also be driven by a spatial variation in their density n, called diffusive motion, that results in a diffusion current density $\boldsymbol{J_{diff}}$ given by Fick's law [27]:

$$\boldsymbol{J_{diff}} = -eD\boldsymbol{\nabla} n \,, \tag{2.2}$$

where D is the diffusion coefficient. Then, using the Einstein relation $\sigma_e = e^2 DN(E_F)$, where $N(E_F)$ is the density of states (DOS) at the Fermi level, that is, the electrons that contribute to the current, and the relation between the field and the electrochemical potential μ:

$$\boldsymbol{\nabla}\mu = -e\boldsymbol{E} + \frac{\boldsymbol{\nabla} n}{N(E_F)} \,, \tag{2.3}$$

we can express the total current density $\boldsymbol{J_q}$ in terms of the gradient of μ [28]:

$$\boldsymbol{J_q} = \boldsymbol{J_{drift}} + \boldsymbol{J_{diff}} = -\frac{\sigma_e}{e}\boldsymbol{\nabla}\mu \,. \tag{2.4}$$

Now, to consider spin currents, we need to account for the spin degree of freedom carried by mobile conduction electrons that can give rise to two types of (electronic) spin currents: pure spin currents and spin-polarized currents.

In ferromagnetic (FM) conductors, carriers with spin-up and spin-down electrons behave as being flowing in two independent transport channels, one for each spin. This is known as the "two-channel model" proposed by Mott in 1936 [29]. Evidence of the spin dependence of the resistivity of magnetic metals was later found [30–32]. Within the model, in FM metals, spin-up and spin-down electrons carry current in parallel with different conductivities ($\sigma_\uparrow \neq \sigma_\downarrow$) [32]. With this approach, the total charge current density J_q is the sum of the charge current density for the spin-up electrons $J_\uparrow$ and the charge current density for the spin-down electrons $J_\downarrow$:

$$\boldsymbol{J}_q = \boldsymbol{J}_\uparrow + \boldsymbol{J}_\downarrow \tag{2.5}$$

Correspondingly, the spin current density can be defined as:

$$\boldsymbol{J}_S = \boldsymbol{J}_\uparrow - \boldsymbol{J}_\downarrow \tag{2.6}$$

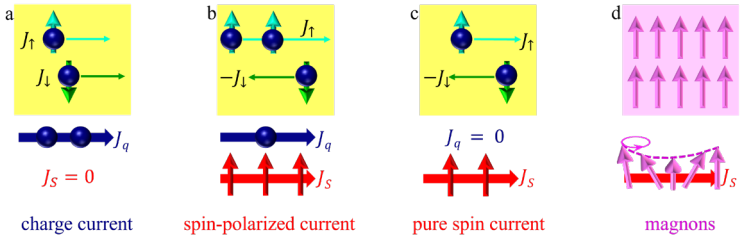

Figure 2.2. Illustration of different types of currents. a) A flow of charge carriers with equal spin-up and spin-down densities generates a pure charge current. b) An unequal DOS between spin-up and spin-down carriers at the Fermi level generates a spin-polarized current. c) Equal number of charges flowing in opposite directions for opposite spins creates a pure spin current. d) A perturbation in a magnetically ordered system produces a spin wave (or magnon).

If we now define the charge current density in terms of the spin-up/down conductivity $\sigma_{\uparrow,\downarrow}$ and the spin-dependent electrochemical potential $\mu_{\uparrow,\downarrow}$, we have:

$$\boldsymbol{J}_{\uparrow,\downarrow} = -\sigma_{\uparrow,\downarrow}\frac{\boldsymbol{\nabla}\mu_{\uparrow,\downarrow}}{e} \tag{2.7}$$

where the conductivities can be expressed as:

$$\sigma_{\uparrow,\downarrow} = \frac{1}{3}N_{\uparrow,\downarrow}(E_F)e^2 v_{F\uparrow,\downarrow}\ell_{\uparrow,\downarrow} \tag{2.8}$$

being $N_{\uparrow,\downarrow}(E_F)$ the electron DOS at the Fermi level for each spin subband, $v_{F\uparrow,\downarrow}$ the Fermi velocity for each spin subband, and $\ell_{\uparrow,\downarrow}$ the mean free path for each spin-up and spin-down population. Then, in a non-magnetic (NM) conductor, where $N(E_F)$ is the same for both spin-up and spin-down electrons, as shown in Figure 2.3a, as well as the electrochemical potential ($\mu_\uparrow = \mu_\downarrow$), the charge current is equally distributed in both channels. As a result, there is no spin current, $\boldsymbol{J}_S = 0$ (see Figure 2.2a). However, if there is an imbalance between the populations of spin-up and spin-down electrons, a spin-polarized current arises (Figure 2.2b). This is the case for metallic FMs, where there is an unequal DOS at the Fermi level, $N_\uparrow(E_F) \neq N_\downarrow(E_F)$ (see Figure 2.3b and c). Then, if a voltage is applied to the FM metal to produce a charge current, this charge current will be spin polarized (Figure 2.2b). In certain conditions, see Sec. 2.1.2, pure spin currents can be generated, in which spin-up electrons move in one direction and the same amount of spin-down electrons move in the opposite direction (see Figure 2.2c).

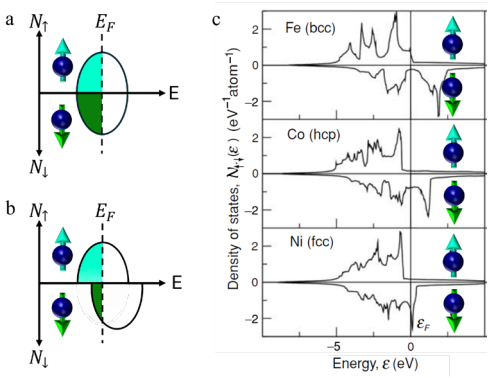

Figure 2.3. a) Sketch of the DOS in a NM metal with spin-up and spin-down electrons having the same values at the Fermi energy. The shaded areas represent the occupied energy states up to the Fermi energy. b) DOS in a FM metal with band splitting, where the energy subband of the spin-up electrons is

shifted to lower energies relative to the spin-down subband. Here, spin-up and spin-down electrons have different DOS at the Fermi energy. c) DOS for some 3d elements (Fe, Co, Ni) in the FM state (adapted from Ref. [33]).

Spin angular momentum can also be carried by other particles and quasiparticles in solid-state systems, extending the concept of spin currents beyond conducting electronics. For instance, a second class of spin flow is due to the spins of core electrons which display a net magnetization with long range order in magnetically ordered systems, which can be either electrically insulating or electrically conducting. In these systems, we have a collection of spins embedded on a lattice in which they can interact with external magnetic fields and with one another. Thermal excitations of the localized spins in these materials give rise to a spin wave, which can directly transport heat and spin but not charge (see Figure 2.2d). This quantized spin wave, also known as a magnon, is a quasiparticle obeying Bose-Einstein statistics. These quantized bosonic excitations of the magnetic lattice carry an angular momentum of $\hbar$ [34].

One can distinguish between two kinds of magnon currents, coherent (or ballistic) and incoherent (or diffusive) currents. For coherent currents, the frequency, wavelength and phase are well defined. By contrast, for incoherent diffusive magnon currents, the driving mechanisms are magnon density gradients and temperature, and no well-defined frequency or phase exist [35].

The propagation of an incoherent magnon spin current density $\boldsymbol{J_m}$ in a magnetic medium can occur because of a nonequilibrium magnon density gradient, which induces a diffusive magnon flow $\boldsymbol{J_m^{diff}}$, or because of a temperature gradient, that gives rise to a magnon flow $\boldsymbol{J_m^{\nabla T}}$. Then, the total magnon current, $\boldsymbol{J_m} = \boldsymbol{J_m^{diff}} + \boldsymbol{J_m^{\nabla T}}$, in terms of the nonequilibrium magnon chemical potential (μ_m), and the magnon spin conductivity (σ_m), is expressed as:

$$\left[\frac{2e}{\hbar}\right] \boldsymbol{J}_m = -\left(\sigma_m \boldsymbol{\nabla}\mu_m + \frac{S_s}{T}\boldsymbol{\nabla}T_m\right) \tag{2.9}$$

where S_s is the spin Seebeck coefficient of the medium, T is the average equilibrium temperature of the magnon bath and $\boldsymbol{\nabla}T_m$ is the temperature gradient applied to the system [36].

2.1.2 Generation and detection of pure spin currents

A great deal of attention has been focused on pure spin currents, which represents a promising new avenue to reduce dissipation, since they use minimal charge carriers thus diminishing Joule heating. But, for that, it is necessary to be able to generate such spin currents, transport them as far as possible (as they are not conservative currents), and finally detecting them. Concerning the generation of pure spin currents, different possibilities have arisen, such as the spin Hall effect (SHE), spin pumping (SP) [37,38], electrical spin injection [39], or spin Seebeck effect (SSE) [40,41].

Let us focus on the SHE. SHE was predicted in 1971 by Dyakonov and Perel [42], and it refers to an effect where a charge current is converted into a transverse pure spin current in a material without magnetic order, but with finite SOC:

$$\boldsymbol{J}_S = \left[\frac{\hbar}{2e}\right] \theta_{SH} \boldsymbol{J}_q \times \hat{\boldsymbol{s}} \tag{2.10}$$

where $\hat{\boldsymbol{s}}$ is the orientation of the spin angular momentum $\boldsymbol{S}$ and θ_{SH} is the spin Hall angle which quantifies the efficiency of the charge to spin current conversion. This angle is defined as the ratio between the transverse spin Hall conductivity ($\sigma_{xy} = \sigma_{SH}$) and the longitudinal charge conductivity (σ_{xx}) [43]:

$$\theta_{SH} = \left[\frac{2e}{\hbar}\right] \frac{\sigma_{xy}}{\sigma_{xx}} \tag{2.11}$$

A larger spin Hall angle indicates a more efficient conversion from charge to spin current, which is desirable in spintronic applications.

In a conductor with SHE, when $\boldsymbol{J}_q$ is applied, the same number of spin-up and spin-down electrons move in the same direction but, while traveling along the conductor, they acquire a spin-dependent transverse velocity. In consequence, spin-up and spin-down electrons are deflected into opposite directions, creating a spin accumulation at the sample

edges, and thus a pure spin current flows along this transverse direction with the spin orientation $\hat{\boldsymbol{s}} \perp \boldsymbol{J}_q \perp \boldsymbol{J}_S$ (see Figure 2.4a) [44].

The reciprocal effect, known as the inverse spin Hall effect (ISHE), converts a spin current into a charge current, permitting the detection of spin currents (see Figure 2.4b). The conversion is given by:

$$\boldsymbol{J}_q = \left[\frac{2e}{\hbar}\right] \theta_{ISH} \boldsymbol{J}_S \times \hat{\boldsymbol{s}} \tag{2.12}$$

where $\theta_{SH} = \theta_{ISH}$ due to Onsager reciprocity [45].

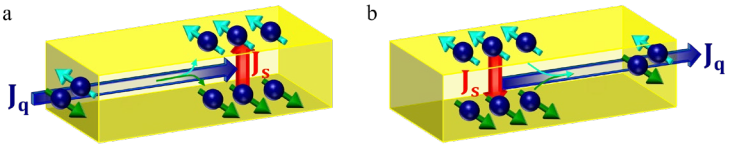

Figure 2.4. Schematic illustrations of a) the SHE that converts an applied charge current density $\boldsymbol{J}_q$ into a transverse pure spin current density $\boldsymbol{J}_s$ because electrons with opposite spins deflect in opposite directions, and b) the ISHE, the reciprocal effect that converts an applied $\boldsymbol{J}_s$ into a transverse $\boldsymbol{J}_q$.

The origin of the SHE and the ISHE is the SOC of the conduction electrons, making the conversion between charge and spin currents possible. The spin-dependent transverse velocities have their origin in intrinsic effects (Berry curvature of the band structure) and extrinsic effects (skew scattering and side-jump scattering) [46]. Consequently, since SOC scales with Z^4, the conversion between $\boldsymbol{J}_s$ and $\boldsymbol{J}_q$ by the SHE and ISHE is expected to be larger in heavy metals such as Pt, W, or Ta.

The SHE and ISHE generate and detect spin currents in electrical conductors without magnetic order, but we may also want spin currents in insulators. In this case, we need to generate magnon currents. Spin angular momentum can flow between NM metals and magnetic insulators (MI). This occurs because, despite the distinct character of electrons and magnons, both carry spin angular momentum and, at the interface between the MI and the NM, the spin angular momentum can be transferred between the electrons and magnons by spin-flip scattering processes via the exchange coupling. At the interface, a conduction electron with spin ½ of the NM can excite a magnon with spin 1 by flipping its spin. On the other hand, if a magnon reaches the

interface, the inverse process will occur. The spin-flip scattering processes in combination with the SHE and the ISHE will allow us to generate and detect magnon spin currents, respectively. Interfacial pure spin currents across the NM/MI interface give rise not only to magnon transport but also to the manifestation of the SP effect, the SSE and the spin Hall magnetoresistance (SMR) (see Ref. [47]).

To understand the spin current across the NM/MI interface, we need to consider a spin accumulation at the NM side of the interface, parametrized by the spin accumulation, defined as $\mu_S(z) = \mu_\uparrow(z) - \mu_\downarrow(z)$, and with spin orientation $\hat{\boldsymbol{s}}$. On the other hand, at the MI side, $\boldsymbol{M}$ represents the magnetic order parameter where the unit vector $\boldsymbol{n}$ describes its orientation $\boldsymbol{n} = \boldsymbol{M}/M$ and the accumulation of magnons is given by the magnon chemical potential μ_m. Moreover, the temperature T_{NM} of the NM system is assumed to be different from the one of the magnon system T_m. With these considerations, the pure spin current flowing from the NM into the MI across the interface is [25,44]:

$$\begin{aligned}\boldsymbol{J}_{S,int} = \frac{1}{4\pi}\left(\tilde{g}_i^{\uparrow\downarrow} + \tilde{g}_r^{\uparrow\downarrow}\boldsymbol{n}\times\right)(\mu_S(0)\hat{\boldsymbol{s}}\times\boldsymbol{n} - \hbar\dot{\boldsymbol{n}}) + \\ [G_s(\mu_m + \mu_S(0)\hat{\boldsymbol{s}}\cdot\boldsymbol{n}) + S_s(T_m - T_{NM})]\boldsymbol{n}\end{aligned} \tag{2.13}$$

Here, G_s is the interfacial spin conductance and $\tilde{g}_i^{\uparrow\downarrow}$and $\tilde{g}_r^{\uparrow\downarrow}$ are the imaginary and real parts of the effective interfacial spin-mixing conductance $\tilde{g}^{\uparrow\downarrow} = \tilde{g}_r^{\uparrow\downarrow} + i\tilde{g}_i^{\uparrow\downarrow}$, including the effects of finite temperature and the magnon band structure of the MI. The first term on the right describes the flow of spin current due to $\tilde{g}^{\uparrow\downarrow}$ that persists even at $T = 0$, while the second term is thermally activated ($T \neq 0$). The physical principles behind the contributions to the spin current across the interface are elastic and inelastic spin-flip scattering processes at the interface for the electrons in the NM [25]. For $\tilde{g}_i^{\uparrow\downarrow}$and $\tilde{g}_r^{\uparrow\downarrow}$ elastic spin-flip scattering is the dominant contribution, and angular momentum is transferred via torque onto the magnetic order parameter $\boldsymbol{n}$. The first term is responsible for the manifestation of the SP and the SMR effects. In the second term on the right, G_s and S_s originate from inelastic electron spin-flip scattering. The spin accumulation in the NM transfers angular momentum to thermal fluctuations of the magnetic lattice changing the number of magnons at the NM/MI interface. The second term is responsible for the SSE and magnon transport.

2.1.3 Diffusion of spin currents

Generally, spins "flip" within a distance characteristic of the metal, its purity, and temperature. This means that spin angular momentum is only conserved on the scale of the spin-flip time τ_{sf} because, as electrons diffuse in the metal and undergo collisions, there is a finite probability to flip its spin. Besides, they can also flip at interfaces.

In an isolated NM, there are different characteristic lengths that we must take into account: the mean free path ℓ, the spin-flip length ℓ_{sf} and the spin diffusion length λ_{SD}. ℓ is the mean distance between collisions or scattering events, where defining a mean time τ between scattering events (momentum scattering time) gives $\ell = v_F\tau$. On the other hand, ℓ_{sf} is the mean distance that electrons travel between spin-flipping collisions and τ_{sf} is the corresponding spin-flip scattering time. It is also convenient to introduce λ_{SD}, which corresponds to the decay length at which an excess of spins exponentially diffuses away. In a single NM metal, the standard form is [48]:

$$\lambda_{SD} = \sqrt{D\tau_{sf}} = \sqrt{(1/3)\ell v_F \tau_{sf}} \tag{2.14}$$

If an excess of spins can be created in the NM, for instance at the interface with a FM in which a current is applied, or at the edge due to the SHE, there will be a difference between the electrochemical potential for spins up ($\mu_\uparrow$) and down ($\mu_\downarrow$), leading to a spin accumulation μ_S. In the limit $\ell \ll \lambda_{SD}$, the spin accumulation is governed by a diffusion equation with length scale λ_{SD}:

$$\frac{\partial^2 \mu_S}{\partial z^2} = \frac{\mu_S}{\lambda_{SD}^2} \tag{2.15}$$

In one dimension, the solution to this equation has the form:

$$\mu_S = Ae^{-z/\lambda_{SD}} + Be^{+z/\lambda_{SD}} \tag{2.16}$$

where the coefficients A and B are determined by boundary conditions and λ_{SD} varies from a few nanometres in heavy metals like Pt, Ta, and W to hundreds of nanometres in Cu, Al, and Au [49].

Similarly, the magnon propagation in magnetic systems driven by the non-equilibrium follows the diffusive equation:

$$\frac{\partial^2 \mu_m}{\partial z^2} = \frac{\mu_m}{\lambda_m^2} \tag{2.17}$$

being λ_m the magnon diffusion length and the solution of the same form as Eq. (2.16). λ_m varies from a few hundreds of nanometres to microns in ferrimagnetic and antiferromagnetic insulators such as $Y_3Fe_5O_{12}$ (yttrium iron garnet, YIG) [50,51], Cr_2O_3 [52,53], and Fe_2O_3 [54,55].

2.1.4 Spin Hall magnetoresistance

The property of a material to change the value of its electrical resistance under an external magnetic field is called magnetoresistance (MR).

When a NM metal is put in contact with a MI, the spin transport between them can influence the charge transport properties of the conductor. The SMR is related to the absorption/reflection of a spin current density J_S flowing perpendicular to the NM/MI interface. When a charge current J_q is applied through the NM, a transverse spin current is induced by SHE (see Figure 2.4a), resulting in a spin accumulation at the NM/MI interface. Then, a spin-angular-momentum exchange (spin-mixing) occurs between the magnetization $\boldsymbol{M}$ of the MI and the polarization $\boldsymbol{s}$ of the spin accumulation of the NM, $\mu_S(0) \neq 0$, that modifies the behaviour of the spin current. The spin current can be absorbed and/or reflected by the MI at the NM/MI interface depending on the orientation of $\boldsymbol{M}$ with respect to $\hat{\boldsymbol{s}}$. The spin current at the interface, $J_{S,int}^{SMR}$, is described assuming that $\mu_m = \dot{\boldsymbol{n}} = T_m - T_{NM} = 0$ in Eq. (2.13):

$$J_{S,int}^{SMR} = \frac{1}{4\pi}\left(\tilde{g}_i^{\uparrow\downarrow} + \tilde{g}_r^{\uparrow\downarrow}\boldsymbol{n}\times\right)(\mu_S(0)\hat{\boldsymbol{s}}\times\boldsymbol{n}) + G_s\mu_S(0)(\hat{\boldsymbol{s}}\cdot\boldsymbol{n})\boldsymbol{n} \tag{2.18}$$

The first term in Eq. (2.18) vanishes when $\boldsymbol{n} \parallel \hat{\boldsymbol{s}}$ and the second term is zero when $\boldsymbol{n} \perp \hat{\boldsymbol{s}}$. This is illustrated in Figure 2.5. When $\boldsymbol{M} \parallel y$, the magnetization is parallel to the spin polarization, so $J_{S,int}^{SMR}$ will be reflected (see Figure 2.5a). However, when $\boldsymbol{M} \parallel x$ or $\boldsymbol{M} \parallel z$, the magnetization is perpendicular to the spin polarization, so $J_{S,int}^{SMR}$ will be

absorbed (Figure 2.5b illustrates the case for $\boldsymbol{M} \parallel x$). At other orientations of $\boldsymbol{M}$ ($\boldsymbol{M} \nparallel x, y, z$), $J_{S,int}^{SMR}$ will be partially absorbed and reflected. If $J_{S,int}^{SMR}$ is reflected, the spin current will induce an extra charge current due to the ISHE, reducing the resistivity of the NM. However, if $J_{S,int}^{SMR}$ is absorbed, no extra charge current will be generated, increasing the resistivity of the NM. In summary, depending on the alignment of $\boldsymbol{M}$, the spin current across the interface is absorbed and/or reflected, resulting in a modulation of the resistivity of the NM layer giving rise to the SMR effect.

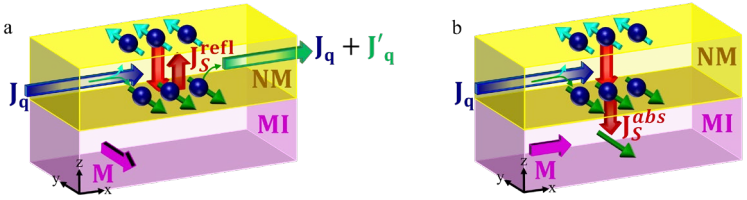

Figure 2.5. Schematic illustration of SMR, where an electric current J_q is sent through a NM material adjacent to a MI. A spin accumulation arises at the interface due to the SHE and, depending on the orientation of the magnetization of the adjacent MI, we have different possibilities. a) When $\boldsymbol{M} \parallel \hat{\boldsymbol{s}}$, the spin current is reflected (J_S^{refl}) and induces an additional current J'_q by the ISHE, which reduces the longitudinal resistance. b) When $\boldsymbol{M} \perp \hat{\boldsymbol{s}}$, the spin current is absorbed (J_S^{abs}), transferring angular momentum into the MI by exerting a torque on $\boldsymbol{M}$ and leading to a higher resistance.

According to the theory, first postulated by Y. -T. Chen et al. [56], the resistivity ρ of the NM layer in the longitudinal ρ_L and transverse ρ_T configuration changes depending on the orientation of the magnetization of the adjacent MI layer as follows:

$$\rho_L^{SMR} = \rho_{L0} + \Delta\rho_1\left(1 - n_y^2\right) \tag{2.19}$$

$$\rho_T^{SMR} = \Delta\rho_1 n_x n_y + \Delta\rho_2 n_z \tag{2.20}$$

where ρ_{L0} is the baseline resistivity of the NM layer and n_x, n_y, n_z are the components of the magnetization $\boldsymbol{M}$ in the x-, y- and z-direction, respectively, of the MI. The amplitude $\Delta\rho_1$ represents the SMR effect which is quadratic in the θ_{SH} since the underlying mechanism is the combination of the SHE and ISHE. The amplitude $\Delta\rho_2$ corresponds to an anomalous Hall-like contribution appearing due to the spin

precession around the exchange field generated by the out-of-plane component of the magnetization (n_z) in the MI.

From Eq. (2.19), it results that angular-dependent magnetoresistance (ADMR) measurements in the three main rotating planes allows to distinguish the existence of the SMR effect. We obtain a specific modulation of ρ_L that follows a $\cos^2(\alpha, \beta)$ modulation in α-plane (xy-plane) and β-plane (yz-plane) with the same amplitude ($\Delta\rho_1$) and no modulation in γ-plane (xz-plane) because $\boldsymbol{M}$ is always perpendicular to $\hat{\boldsymbol{s}}$ (see Figure 2.6a, b). Therefore, SMR enables sensing the magnetic properties such as the $\boldsymbol{M}$ direction of a MI by measuring ρ_L of the adjacent NM layer.

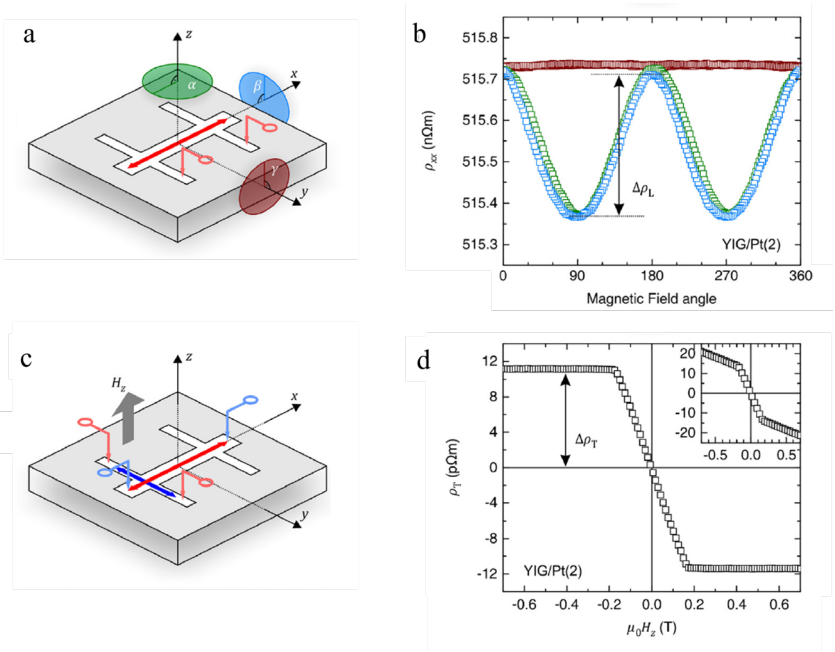

Figure 2.6. a) Main magnetic field rotation angles and longitudinal measurement configuration where the red double-arrow indicates the charge current flowing in x-direction. b) Longitudinal ADMR for YIG/Pt(2 nm) at a magnetic field strength of 1 T measured using the configurations of panel a. c) Transverse resistivity measurement while sweeping the magnetic field along the z-direction and current alternatingly in the x- and y-directions (zero-offset Hall measurement). d) Zero-offset Hall measurement after subtracting the ordinary Hall effect for YIG/Pt(2 nm). The inset shows the data before the subtraction of the ordinary Hall signal. Figure extracted from [57].

From Eq. (2.20), two distinct transverse resistivity contributions can be identified. The first term, $\Delta\rho_1 n_x n_y$, is analogous to the planar Hall effect and results from the anisotropy of the longitudinal resistivity in the NM layer described in Eq. (2.19). The second term, $\Delta\rho_2 n_z$, resembles an anomalous Hall effect as explained above. These contributions manifest in ρ_T and can be experimentally accessed through ADMR or field-dependent magnetoresistance (FDMR) measurements. As shown in Figure 2.6d, the value of $\Delta\rho_2$ (labelled $\Delta\rho_T$ in the figure) is extracted from the FDMR data, confirming the presence of the anomalous Hall-like contribution.

Moreover, the amplitudes of the SMR, $\Delta\rho_1$ and $\Delta\rho_2$, can be expressed in terms of the spin properties of the NM layer via θ_{SH}, λ_{SD}, the bulk conductivity $\sigma = 1/\rho_{L0}$ of the NM and the film thickness t_{NM}:

$$\Delta\rho_1 = \rho_{L0}\theta_{SH}^2 \frac{\lambda_{SD}}{t_{NM}} Re\left[\frac{2\lambda_{SD}\tilde{G}^{\uparrow\downarrow}\tanh^2\frac{t_{NM}}{2\lambda_{SD}}}{\sigma + 2\lambda_{SD}\tilde{G}^{\uparrow\downarrow}\coth\frac{t_{NM}}{\lambda_{SD}}}\right] \tag{2.21}$$

$$\Delta\rho_2 = -\rho_{L0}\theta_{SH}^2 \frac{\lambda_{SD}}{t_{NM}} Im\left[\frac{2\lambda_{SD}\tilde{G}^{\uparrow\downarrow}\tanh^2\frac{t_{NM}}{2\lambda_{SD}}}{\sigma + 2\lambda_{SD}\tilde{G}^{\uparrow\downarrow}\coth\frac{t_{NM}}{\lambda_{SD}}}\right] \tag{2.22}$$

being $\tilde{G}^{\uparrow\downarrow} = \frac{e^2}{h}\tilde{g}^{\uparrow\downarrow}$. Consequently, SMR allows to non-invasively access to fundamental spin transport parameters such as θ_{SH}, λ_{SD} of different NM layers and $\tilde{g}^{\uparrow\downarrow}$ of different NM/MI interfaces by using a wide variety of NM/MI combinations. SMR has been studied in several NM/MI bilayers, being YIG/Pt one of the key reference combinations, with an amplitude $\Delta\rho_1/\rho_{L0}$ of the order of 10^{-4} [57–59] and $\Delta\rho_2/\rho_{L0}$ of the order of 10^{-5} [57], since $\tilde{G}_i^{\uparrow\downarrow}$ is one order of magnitude smaller than $\tilde{G}_r^{\uparrow\downarrow}$ in YIG [59,60].

2.1.5 Hanle magnetoresistance

Similar to the SMR, Hanle magnetoresistance (HMR) arises because of the interaction of the spin accumulation generated by the SHE within the NM layer, with an external source [61]. In this case, it is the action of an external magnetic field H what produces a modulation in the

resistivity due to precession so that, contrary to the SMR, HMR appears in single NM layers. The equations that describe the HMR are as follow:

$$\rho_L^{HMR} = \rho_{L0} + \Delta\rho_1^{HMR}\left(1 - n_y'^2\right) \tag{2.23}$$

$$\rho_T^{HMR} = \Delta\rho_1^{HMR} n_x' n_y' + \Delta\rho_2^{HMR} n_z' \tag{2.24}$$

where $\boldsymbol{n}'$ denotes the orientation of the magnetization of the external magnetic field $\boldsymbol{n}' = \boldsymbol{H}/H$. As shown in Figure 2.8a, the same ADMR dependencies as in the SMR appear but, in this case, the amplitude depends on the strength of H.

When a charge current J_q is applied, a spin accumulation appears at the boundaries due to the SHE. However, due to the presence of an external H, the spins precess due to Hanle effect, but only when $\boldsymbol{H}$ is not collinear with the spin polarization (see Figure 2.7). If $\boldsymbol{H} \parallel \hat{\boldsymbol{s}}$, no precession will occur, giving a state of minimum ρ_L (Figure 2.7a and Figure 2.7c). On the contrary, if $\boldsymbol{H} \nparallel \hat{\boldsymbol{s}}$, precession occurs and the original spin accumulation is reduced due to the dephasing of diffusing spins reducing the extra charge current generated due to ISHE and increasing ρ_L (Figure 2.7b and Figure 2.7d), as described by Eq. (2.23).

The transverse magnetoresistance is described by Eq. (2.24) which depends on the magnetic field projections along the three axis and the amplitude is given by $\Delta\rho_1^{HMR}$and $\Delta\rho_2^{HMR}$. $\Delta\rho_1^{HMR}$ arises because magnetoresistance is anisotropic in plane, while $\Delta\rho_2^{HMR}$ appears because the magnetic field out of plane induces the precession of $\boldsymbol{s}$ allowing for the ISHE to produce a transverse charge current.

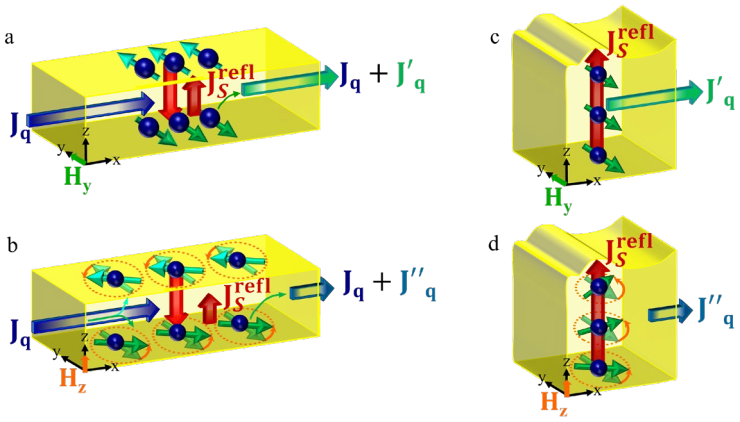

Figure 2.7. Schematic illustration of Hanle magnetoresistance. a) In the presence of an external magnetic field H_y, paralell to the spin polarization $\boldsymbol{s}$, no precession occurs, but the combination of SHE and ISHE generates an extra current J'_q which gives a state of minimum ρ_L. b) Zoom of the spin current reflected J_s^{refl} that diffuses generating, by ISHE, a final charge current J'_q. c) Because of the presence of H_z perpendicular to the initial spin polarization, spin precession around H_z occurs which decreases the initially aligned spin polarization, so the contribution to J''_q will be reduced, increasing ρ_L. d) Zoom of J_s^{refl}, spin dephasing arises from simultaneous spin precession and diffusion when $\boldsymbol{H} \perp \hat{\boldsymbol{s}}$.

HMR provides a way to quantify spin transport parameters in NMs in a similar way to SMR, but without the complication of magnetic interfaces. We can express $\Delta\rho_{1,2}^{HMR}$ as:

$$\Delta\rho_1^{HMR} = 2\rho_{L0}\theta_{SH}^2\left\{\frac{\lambda_{SD}}{t_{NM}}tanh\left(\frac{t_{NM}}{2\lambda_{SD}}\right) - Re\left[\frac{\Lambda}{t_{NM}}tanh\left(\frac{t_{NM}}{2\Lambda}\right)\right]\right\} \tag{2.25}$$

$$\Delta\rho_2^{HMR} = 2\rho_{L0}\theta_{SH}^2 Im\left[\frac{\Lambda}{t_{NM}}tanh\left(\frac{t_{NM}}{2\Lambda}\right)\right] \tag{2.26}$$

where $\Lambda^{-1} = \sqrt{\frac{1}{\lambda_{SD}^2} + i\frac{g_S\mu_B H}{D\hbar}}$ [62,63].

According to Eq. (2.25), the amplitude of the longitudinal HMR depends on the strength of the magnetic field. In the limit of weak

precession, the effect is quadratic with magnetic field, so a parabolic increase can be observed when performing a FDMR measurement, with $\boldsymbol{H} \perp \hat{\boldsymbol{s}}$, as illustrated in Figure 2.8b. However, as $\boldsymbol{H} \perp \hat{\boldsymbol{s}}$ is increased, the strong precession reduces the spin accumulation along y and in consequence the resulting charge current diminishes too. Because of that, the longitudinal magnetoresistance tends to saturate in the strong precession limit following the $tanh$ dependence described by Eq. (2.25).

The amplitude of the transverse HMR with out-of-plane field, given by Eq. (2.26), also follows a field-dependent behaviour. It increases with the magnetic field in the weak precession regime and tends to saturate when strong precession fully suppresses the spin accumulation along the transverse direction. This behaviour is observed as an antisymmetric signal in FDMR measurements (see Fig. 2.8c).

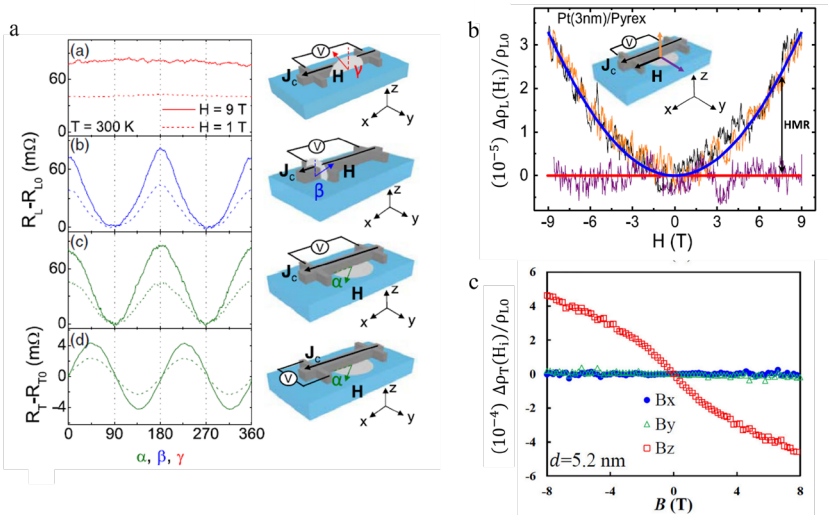

Figure 2.8. a) ADMR measurements in a Pt(7 nm)/YIG sample at 300 K and 1 T (dashed lines) or 9 T (solid lines) in the three relevant H-rotation planes (α, β, γ). Sketches on the right side indicate the definition of the angles, the axes, and the measurement configuration. b) Normalized longitudinal FDMR curves along the 3 main axes in Pt(3 nm)/Pyrex at 100 K. c) Normalized transverse FDMR curves for a 5.2-nm-thick epitaxial Pt(111) film grown on Al_2O_3(0001), measured at room temperature. Panels a) and b) extracted from [62], and c) adapted from [63].

2.1.6 Spin Seebeck effect

The history of thermoelectric generation, which refers to the generation of electricity from heat, began with the discovery of the Seebeck effect by T. J. Seebeck in 1821 [64]. In analogy to this conventional "charge" Seebeck effect, where a charge current is driven by an applied temperature gradient in a conductor, a spin current is driven by a temperature gradient in the spin Seebeck effect (SSE). The SSE, first demonstrated in 2008 by Uchida et al. [41], has been observed in various magnetic materials ranging from metallic ferromagnets [41,65] to insulating magnets [66–68].

A typical system used for measuring the SSE is a NM/MI bilayer. When a temperature gradient ($\nabla T = T_m - T_{NM} \neq 0$) is applied perpendicular to the interface, a magnon spin current is generated along ∇T due to the thermally excited dynamics of localized magnetic moments. At the NM side of the NM/MI interface, it will give rise to an electron spin current J_S. Then, by virtue of the ISHE, J_S will be converted into a transverse charge current J_q (see Figure 2.9) that, under electrical open circuit conditions, can be measured as a voltage drop [69].

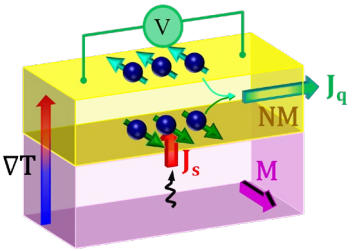

Figure 2.9. Illustration of the SSE. The temperature gradient ∇T applied gives rise to a temperature difference $T_m - T_{NM}$ between the magnons in the MI and the electrons in the NM at the interface. This results in a pure spin current J_S injected across the interface, which is transformed into a charge current J_q via the ISHE and detected as a voltage.

2.1.7 Magnon transport: electrical and thermal (SSE) generation

To investigate magnon transport due to incoherent magnon currents, the most common device comprises two strips of a NM used to generate and detect magnons, placed in contact with a MI for the propagation of magnons (see Figure 2.10). When a charge current density J_q^{in} is applied through a NM strip (called injector), a spin accumulation along the y-axis appears due to the SHE associated to a spin current J_S^{in}, as already discussed in section 2.1.2. Two main phenomena can then occur. First, J_S^{in} may be either absorbed or reflected back at the NM/MI interface, giving rise to the SMR (see Sec. 2.1.4). Second, magnons can be created/annihilated (represented by black arrows in Figure 2.10), through spin-flip scattering processes (see Figure 2.10b and Figure 2.10c), resulting in electrically induced magnons producing a magnon accumulation/depletion at the MI side of the NM/MI interface. In addition to these electrically generated magnons, thermally induced magnons due to SSE can also be excited by the thermal gradient at the interface caused by Joule heating.

Regardless of their origin, electrical or thermal, the resulting non-equilibrium magnon population diffuses in the MI on the length scale of the magnon diffusion length λ_m. Then, if the second NM strip (the detector) is close enough, magnons can reach it and, through reciprocal spin-flip processes, inject a pure spin current J_S^{det} into the NM. By means of the ISHE, it will be transformed back into a charge current J_q^{det} that can be electrically detected.

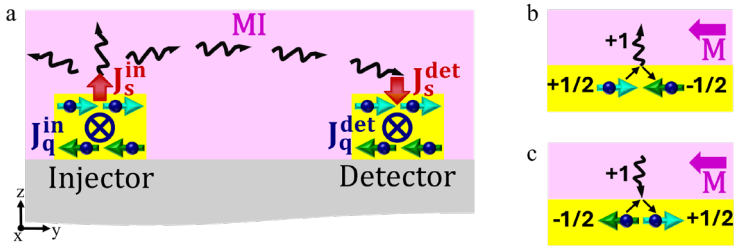

Figure 2.10. a) Schematic representation of the magnon transport device. A charge current density J_q^{in} through the injector generates a spin current density J_S^{in} due to the SHE and the corresponding spin accumulation at the NM/MI

interface. By exchange coupling, angular momentum is transferred from the NM to the MI, exciting magnons (black arrows). Magnons diffuse and can reach the detector, where they are annihilated, and a spin accumulation is generated. Through the ISHE, the spin current density J_S^{det} at the detector interface is converted into a charge current density J_q^{det}. b) Magnon creation. An electron in the NM transfers angular momentum to the MI by flipping its spin, which results in the creation of a magnon and c) magnon annihilation, where the inverse process occurs.

As discussed before, the second term in Eq. (2.13) accounts for magnon-mediated spin transport. It contains both an electrically excited contribution, related to the magnon chemical potential μ_m, and a thermally excited contribution, driven by the temperature difference $T_m - T_{NM}$, directly associated with the SSE [24].

Focusing first on the electrically excited magnons, Eq. (2.13) requires $\boldsymbol{M}$ and $\hat{\boldsymbol{s}}$ to be collinear to generate magnons. When a charge current density J_q^{in} is applied through the injector, $\hat{\boldsymbol{s}}$ is along y, but only the component of it collinear to $\boldsymbol{M}$, $\hat{\boldsymbol{s}} \parallel \boldsymbol{M}$, will contribute to excite the magnons, as illustrated in Figure 2.11a. Then, magnons diffuse through the MI and can reach the detector. An electron spin accumulation μ_s with $\hat{\boldsymbol{s}}$ parallel to $\boldsymbol{M}$ will be generated due to the transfer of spin angular momentum from the magnons. Now, due to the symmetry of ISHE, only the component of the spin accumulation along y will contribute to the induced charge current density, which under open-circuit conditions generates a non-local voltage V_{NL} [25]. Because only the component $\hat{\boldsymbol{s}} \parallel \boldsymbol{M}$ contributes to magnon injection and detection, V_{NL} depends on the angle of rotation in the sample plane, α, as $V_{NL} \propto \sin^2 \alpha$ (see Fig. 2.11a and b). This is known as the electrical (or first harmonic) non-local response V_{NL}^e.

Moreover, the applied $\boldsymbol{J}_{q,in}$ not only excites magnons electrically, as previously discussed, but also induces Joule heating at the NM/MI interface. This heating creates a temperature gradient proportional to the square of the current (I^2), as shown in Figure 2.11c. When the thermal gradient appears, the magnon population is driven out of equilibrium and a magnon current can flow between the hot and the cold side of the system, resulting in the SSE (see Sec. 2.1.6). This leads to a depletion ($\mu_m < 0$) of magnons at the MI side of the injector/MI interface and due to magnon diffusion they accumulate ($\mu_m > 0$) further away from the injector. For these thermally excited magnons,

the same process discussed for the electrically excited magnons occur at the detector strip, based on the orientation of $\boldsymbol{M}$. Because the injection depends on the thermal gradient, which is independent of α, the dependence on the angle α only at the detector, which results in this case in $V_{NL} \propto \sin\alpha$ (Figure 2.11c and Figure 2.11d). Moreover, the detection of thermally excited magnons can occur at the same injector strip, local SSE (V_{LOC}^{th}) or at the detector strip, non-local SSE (V_{NL}^{th}). The latter is known as the thermal (or second harmonic) response. Due to the redistribution of magnon population, a sign change can appear between the local and non-local SSE measured. The sign of μ_m determines de direction of the interfacial spin current $\boldsymbol{J}_{S,int}$, as well as the sign of the detected voltage [70].

To separate the first (V_{LOC}^{e}, V_{NL}^{e}) and second harmonic (V_{LOC}^{th}, V_{NL}^{th}) response, we applied the DC current reversal technique, as described in Sec. 3.2.2.

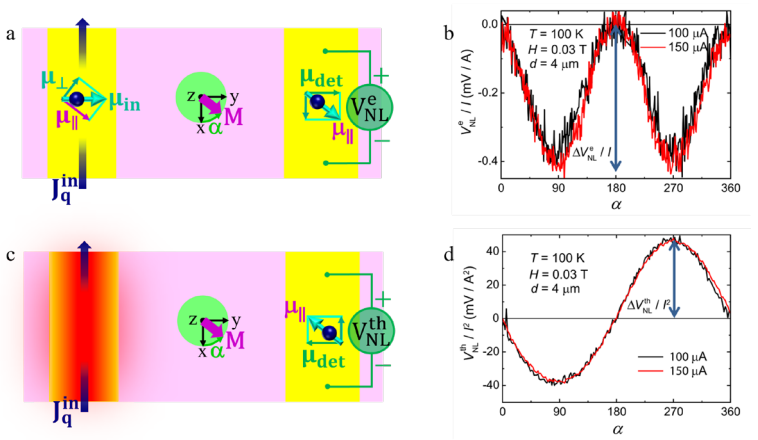

Figure 2.11. a) Schematic top-view of the magnon transport device in the case of electrically excited magnon generation. A charge current density J_q^{in} through the injector generates a spin accumulation μ_{in}. The component parallel to the MI magnetization $\mu_{\parallel}$ generates non-equilibrium magnons in the MI that diffuse through the MI. At the detector, a spin accumulation $\mu_{\parallel}$ parallel to $\boldsymbol{M}_{MI}$ is generated. Then, due to the ISHE, only the component μ_{det} contributes to the voltage. b) Representative angular-dependent non-local voltage detected, normalized to the applied current, for electrically excited magnons, in a YIG/Pt(5nm) device, using the measurement configuration shown in a) (from Ref. [71]). c) Schematic top-view of the magnon transport device on the case of thermally excited magnon generation. At the injector/MI interface, magnons

are excited thermally, and then diffuse and reach the detector where the process depends on the angle, as in a). d) Representative angular-dependent non-local voltage detected, normalized to the square of the applied current, for thermally excited magnons, in a YIG/Pt(5nm) device, using the measurement configuration shown in c) (from Ref. [71]).

In non-local experiments, the quality of the interface is important for the optimal excitation and detection of magnon currents flowing through the MI. As shown in Sec. 2.1.3, the magnon diffusion length λ_m is the key parameter which defines the transport of magnons. In order to extract λ_m, it is necessary to use the non-local configuration, shown in Figure 2.10 and Figure 2.11, and change the distance d between injector and detector. Depending on d, different regimes must be considered [72]. At very short distances, $d \ll \lambda_m$, magnon transport is diffusive and the signal decays as $\mu_m \sim 1/d$. At intermediate distances, magnon transport is dominated by magnon relaxation which translates into an exponential decay of the signal $\sim e^{-d/\lambda_m}$. Finally, at very long distances, $d \gg \lambda_m$, the system enters the $1/d^2$ regime, where the signal no longer depends on λ_m, since it arises by a temperature gradient induced at the detector by geometric thermal diffusion [72].

2.1.8 Spin dynamics

Spin dynamics, commonly referred as magnetization dynamics in ferromagnetic thin films and confined structures, refers to the dynamics of either the population and the phase of the spin of an ensemble of particles, or a coherent spin manipulation of a single- or a few-spin system. Understanding the spin dynamics is essential for future applicability of spintronic devices.

To understand the basis, we first consider a single electron spin. Under the influence of a static magnetic field $\boldsymbol{H}$, the spin magnetic moment $\boldsymbol{m_S}$ aligns along $\boldsymbol{H}$ acquiring an energy:

$$E_{Zeeman} = -\mu_0 \boldsymbol{m_S} \cdot \boldsymbol{H} \tag{2.27}$$

Moreover, $\boldsymbol{H}$ interacts with $\boldsymbol{m_S}$, exerting a torque $\boldsymbol{\Gamma}$, which is given by:

$$\boldsymbol{\Gamma} = \mu_0 \boldsymbol{m_S} \times \boldsymbol{H} \tag{2.28}$$

This torque can also be described as the time evolution of the spin angular momentum, $\boldsymbol{\Gamma} = d\boldsymbol{S}/dt$. Since $\boldsymbol{m_S}$ and $\boldsymbol{S}$ are related by Eq. (1.3) substituting this relation into Eq. (2.28) yields:

$$\frac{d\boldsymbol{m_S}}{dt} = -\gamma_S \mu_0 \boldsymbol{m_S} \times \boldsymbol{H} \tag{2.29}$$

where the gyromagnetic ratio is defined as $\gamma_S = \frac{g_S \mu_B}{\hbar}$. This form shows that the dynamics of the spin magnetic moment is governed by a precessional motion around $\boldsymbol{H}$, if they are initially non-collinear, with the Larmor frequency $\omega_L = \gamma_S H$.

Moving on from a single electron spin to an ensemble of spins, Eq. (2.29) takes the form:

$$\frac{d\boldsymbol{M}}{dt} = -\gamma_S \mu_0 \boldsymbol{M} \times \boldsymbol{H} \tag{2.30}$$

This expression describes the coherent precessional motion of the collective magnetization vector $\boldsymbol{M}$ around $\boldsymbol{H}$.

In order to account also for the relaxation of the magnetization, Landau and Lifshitz (LL) proposed in 1935 a phenomenological model which incorporates damping. The resulting equation describes the magnetization precession and subsequent relaxation towards its equilibrium position [73]:

$$\frac{d\boldsymbol{M}}{dt} = -\gamma_{LL} \mu_0 \boldsymbol{M} \times \boldsymbol{H}_{eff} - \frac{\lambda_{LL}}{M_S^2} \boldsymbol{M} \times (\boldsymbol{M} \times \boldsymbol{H}_{eff}) \tag{2.31}$$

where γ_{LL} is an effective gyromagnetic ratio [which differs from the intrinsic spin gyromagnetic ratio γ_S, see Eq. (2.33)], $\lambda_{LL} > 0$ is a phenomenological damping constant with units of frequency and M_S is the saturation magnetization. The effective magnetic field $\boldsymbol{H}_{eff}$ contains not only the external applied magnetic field H_{DC} but also the internal contributions such as anisotropy, demagnetizing and exchange fields.

Although LL equation works well for several experimental observations, T. L. Gilbert later refined the damping description in

1955, to take into account systems with large enough damping. This led to the Landau-Lifshitz-Gilbert (LLG) equation [74]:

$$\frac{d\boldsymbol{M}}{dt} = -\gamma_S \mu_0 \boldsymbol{M} \times \boldsymbol{H}_{eff} + \frac{\alpha_G}{M_s} \boldsymbol{M} \times \frac{d\boldsymbol{M}}{dt} \tag{2.32}$$

where α_G is the Gilbert damping parameter and γ_S is the gyromagnetic ratio as defined in Eq. (2.29). Although structurally different, the LL and LLG equations are mathematically equivalent under the assumption that the damping is sufficiently small ($\alpha_G \ll 1$). One can show that the LL equation can be obtained from the LLG formulation by a rearrangement and rescaling of parameters. The following relations link both formalisms:

$$\gamma_{LL} = \frac{\gamma_S}{1+\alpha_G^2}\,;\, \lambda_{LL} = \frac{\alpha_G \gamma_S \mu_0 M_s}{1+\alpha_G^2} \tag{2.33}$$

Low damping materials are required to achieve low energy loss, high sensitivity, and long spin-wave propagation. However, in FM metals, spin excitations are strongly attenuated due to the dominant scattering with conduction electrons [24,75–78]. In MIs, on the other hand, a low damping is typically measured because spin scattering processes from conduction electrons are absent [24,79].

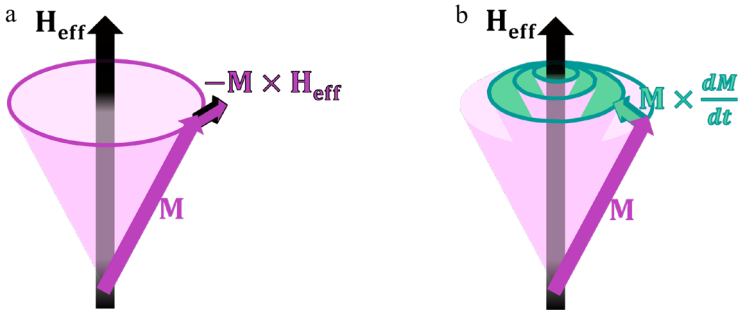

Figure 2.12. a) Magnetization dynamics where a torque causes the precession of $\boldsymbol{M}$ around the effective magnetic field describing a cone. b) Magnetization dynamics in presence of damping, as described by the LLG equation.

Historically, ferromagnetic resonance (FMR) spectroscopy, dating back to the first half of the 20th century, has been one of the standard tools to study the magnetization dynamics in magnetic structures [80]. In FMR experiments, an oscillating external electromagnetic field is applied to

the sample to sustain the precession. If the frequency of this electromagnetic field coincides with the precession frequency of the FM, the material undergoes resonance. FMR allows investigation of the magnetization precession and the associated energy dissipation, providing important parameters such as the saturation magnetization and damping of thin magnetic films and magnetic heterostructures [81,82].

Starting from the equation of motion for the precession of magnetization, Eq. (2.30), Kittel determined the resonance frequency for magnetization canted at a sufficiently small precession-cone angle [83]. In the case of a thin film, that can be considered as infinitely extended in its plane, the resonance frequency is a special case of the Kittel formula with a value given by:

$$f = \frac{\gamma_S \mu_0}{2\pi} \sqrt{H_{res}\left(H_{res} + M_{eff}\right)} \tag{2.34}$$

where H_{res} is the effective field at resonance condition, M_{eff} is the effective magnetization and $\gamma_S/2\pi \approx 28$ GHz/T sets the frequency scale for the FMR phenomenon.

The broadening of the FMR peak linewidth ΔH is a direct measurement of the magnetic damping of the system and can be described by a linear dependence on the frequency:

$$\mu_0 \Delta H = \mu_0 \Delta H_0 + \frac{4\pi\alpha_G}{\gamma_S} f \tag{2.35}$$

In this expression, the frequency-independent inhomogeneous linewidth broadening ΔH_0 arises from the presence of magnetic inhomogeneities. The second term arises from the total Gilbert damping α_G, which contains intrinsic and extrinsic damping contributions.

Intrinsic Gilbert damping effects are inherent to the fundamental physical state of a FM system and cause damping even in materials which have a perfect crystal structure. Indeed, the damping considered by LL was described to be due to the relativistic interaction [73] or, in other words, to the SOC which is an intrinsic process [84]. Intrinsic damping due to SOC arises because spin and orbital moments can exchange momentum back and forth during the precession of

magnetization [85]. In 1976, Kamberský proposed a SOC torque-correlation model where the damping is governed by intraband and interband transitions in magnetic metals [86].

In addition to the intrinsic Gilbert damping, several pervasive extrinsic Gilbert damping mechanisms exist, such as two-magnon scattering, eddy current damping, radiative damping, and interfacial contributions [87].

Two-magnon scattering was proposed in the 1960s to explain the extrinsic contribution observed in YIG spheres [88]. Later, Arias and Mills developed a theory for ultrathin films, where the two-magnon scattering is induced by defects at surfaces and interfaces [89]. Two-magnon scattering is caused by the scattering-centres for magnon scattering. In the two-magnon process, a uniform precession magnon (wave vector $k = 0$) is annihilated and a ($k \neq 0$) magnon is created, the total number of magnons remaining unchanged.

Moreover, in a FM material which is electrically conducting, any change in the magnetization induces eddy currents which tend to oppose this change and thus provide a damping mechanism [90,91]. This mechanism is known as screening of the electromagnetic microwave field by the conduction electrons, and dissipation in this process is proportional to the conductivity of the sample. Eddy currents become important when the film thickness (t_{FM}) is larger than or comparable to the skin depth, which is described as the depth below the surface of the conductor at which the current density decays to $1/e$ of the current density at the surface [85]. Eddy current damping is expressed as [92]:

$$\alpha_{eddy} = \frac{\mu_0^2 M_S \gamma_S \sigma t_{FM}^2}{12} \tag{2.36}$$

As the eddy current damping is proportional to t_{FM}^2, it is significantly reduced for thin samples.

Another source of extrinsic damping is the radiative damping which is caused by eddy currents induced in the waveguide used to measure the damping of the sample. Unlike eddy current damping, radiative damping depends on the properties and dimensions of the waveguide

and the sample, so it is relevant for both ferromagnetic insulators and conductors. The damping contribution is given by [93]:

$$\alpha_{rad} = \frac{\mu_0^2 M_S \gamma_S t_{FM} l}{2 Z_0 w_{cc}} \tag{2.37}$$

where Z_0 and w_{cc} are the conductor impedance and width, respectively; and l is the sample length. Because it depends linearly on M_S and t_{FM}, for very thin films or films with low M_S, α_{rad} is not a significant contribution to the total Gilbert damping and can be neglected [94]. On the contrary, in FM with very low damping, the contribution can become significant.

Moreover, magnetization dynamics can also be explored through the SP effect in a FM/NM bilayer system. When FMR occurs in the FM, precession of the magnetization transfers spin angular momentum to the NM at the interface, generating a spin current J_S into the adjacent NM. As a result, spin transport reduces the magnetization of the FM and hence enhances damping (see Figure 2.13). Therefore, SP allows to determine the spin-mixing conductance ($\tilde{g}^{\uparrow\downarrow}$) across the interface, which describes the number of spin channels per unit area of the interface, through α_G. The real part of the spin-mixing conductance, $\tilde{g}_r^{\uparrow\downarrow}$, determines the ability of the interface to transmit spins. Then, from the Gilbert damping constants of a FM single layer, α_{FM}, and a FM/NM bilayer, $\alpha_{FM/NM}$, we can obtain $\tilde{g}_r^{\uparrow\downarrow}$ [95]:

$$\tilde{g}_r^{\uparrow\downarrow} = \frac{4\pi M_S t_{FM}}{g\mu_B}\left(\alpha_{FM/NM} - \alpha_{FM}\right) \tag{2.38}$$

where g is the Landé g-factor, which quantifies the ratio between the magnetic moment and the total angular momentum in the ferromagnetic system, accounting for both spin and orbital contributions. While early theoretical models of magnetization dynamics (Landau & Lifshitz, 1935 [73] ; Gilbert, 1955 [74]; and Kittel, 1948 [83]) considered only the spin contribution (g_S), Eqs. (2.29)-(2.35), experimental such as FMR and spin pumping require the full Landé g-factor to relate observed damping and precession to the total magnetic moment [37,96].

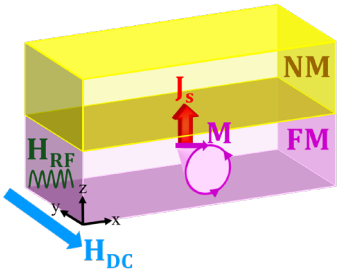

Figure 2.13. Schematic of FMR spin pumping in a FM/NM bilayer. The FM magnetization precesses when resonantly excited by an rf magnetic field, H_{RF}, in the precense of a DC field, H_{DC}. The precession of the magnetization, M, in the FM layer transfers spin angular momentum across the interface to the conduction electrons in the NM and a spin current J_S is created.

2.2 Orbitronics

Orbitronics is a new field which exploits the orbital degree of freedom in a similar way as spintronics does with the spin. Therefore, the orbital angular momentum (OAM) can be viewed as an information carrier. However, contrary to spintronics, this is an emerging field with much less background.

First studies on the possible exploitation of the OAM dated back to 2005 [97–99], when B. A. Bernevig *et al.* proposed the term "orbitronics" to refer to a hypothetical field based on "the possibility of replacing the spin degree of freedom by the orbital degree or freedom" [97].

As in spintronics, the development of orbitronic devices relies on the ability to generate, transport and detect OAM in solid-state systems. Achieving efficient control over these processes is essential for the realization of functional orbitronic technologies.

2.2.1 Orbital currents

A clear difference between orbital and spin currents is that, unlike spin, orbital currents cannot be defined in vacuum because OAM arises from the motion of electrons in the periodic potential of a crystal lattice.

Classically, in the presence of an electric field, conduction electrons drift in the field direction while also experiencing rotational motion around the atoms they pass by. The electron motion perceived by an external observer is the combination of linear translation and successive gyrations around the atoms encountered by the electron along its path. This rotational motion corresponds to the non-equilibrium OAM carried by the electrons, and their collective motion constitutes an orbital current [100].

The orbital diffusion length λ_{OD} is the key parameter that determines how far orbital currents can propagate and thus determines the efficiency of orbital information transport in device architectures. However, reported values for λ_{OD} vary widely, ranging from a few nanometres, in materials with either strong or weak SOC [101–103], to several tens of nanometres in certain cases [104–106]. This wide disparity reflects the challenges in accurately measuring λ_{OD}.

Recent theoretical work by M. Rang and P. J. Kelly has provided new insight into this issue [107]. Using quantum mechanical scattering calculations in thermally disordered solids with large scattering geometries (thousands of atoms), they found that the decay of the orbital current occurs over only a few atomic layers (see Figure 2.14). The orbital polarization decays to less than 1/e of its injected value within less than a nanometre. Moreover, the orbital current can be converted into a spin current within a similarly short length, suggesting that this process may be interface mediated. Importantly, the orbital diffusion length in transition metals is as short as expected from classical orbital quenching arguments and does not depend on the orbital or spin Hall angle, nor the polarization. These findings contrast with the longer λ_{OD} values inferred from some experiments. The results suggest that what is often interpreted experimentally as long λ_{OD} may correspond to the λ_{SD} generated by orbital-to-spin conversion [107].

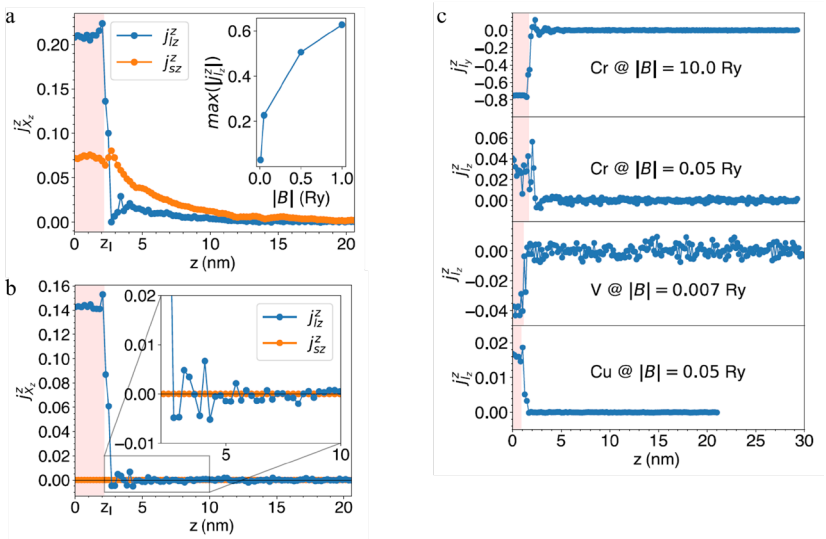

Figure 2.14. a) A current of orbital angular momentum polarized in the z direction, J_L^z, and injected into a room temperature thermally disordered Pt in the z direction, J_{Lz}^z, is converted into J_S within a few atomic layers after which it decays on a length scale consistent with the spin diffusion length of Pt. For the orbital Zeeman term in the lead, a value of B = 0.05 Ry was used. To visualize the current in the lead, the interface between ballistic (pink) and diffusive Pt is displaced into the scattering region to $z = z_I$. The inset shows how the degree of orbital polarization depends on the size of the orbital Zeeman splitting in the lead. b) Same as a) but with the SOC switched off. c) J_{Lz}^z injected from an orbitally polarized left lead decays within a few atomic layers in thermally disordered Cr, V and Cu. (Fig. adapted from [107]).

2.2.2 Generation and detection of orbital currents

In 2008, new theoretical studies explored the orbital degree of freedom by examining the orbital Hall effect (OHE), which is the orbital analogue of the SHE [108,109]. In the OHE, electrons with opposite OAM deflect in opposite directions when a charge current J_q is applied through a metal, giving rise to a transverse orbital current J_L (see Figure 2.15a) [108–112].

Complementarily, the reciprocal effect, known as the inverse orbital Hall effect (IOHE), allows the conversion of J_L into J_q, enabling the detection of orbital currents (see Figure 2.15b).

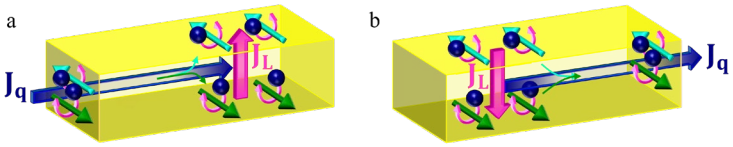

Figure 2.15. a) Schematic illustrations of the OHE. An applied charge current density J_q generates a transverse orbital current density J_L, because electrons with opposite OAM deflect in opposite directions. b) In the IOHE, an applied J_L is converted into a transverse J_q.

According to these early theoretical studies on the OHE, the orbital Hall conductivity (σ_{OH}), which quantifies the efficiency of the OHE in a given material, was found to be positive for all 4d and 5d transition metals and almost 1 order of magnitude higher than σ_{SH} (see Figure 2.16) [108]. Remarkably, the OHE can occur even in the absence of SOC [108,113]. These findings suggested that orbitronic devices could be fabricated using transition metals. But, at that time, orbital transport did not receive too much attention.

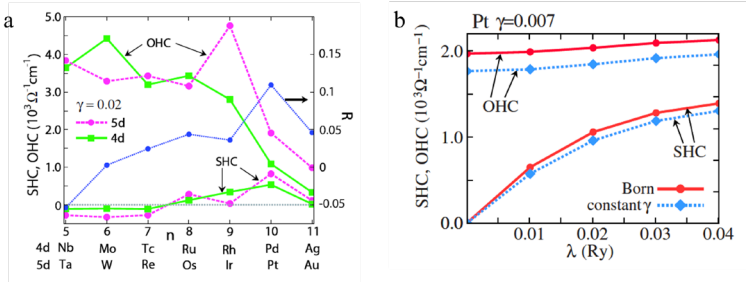

Figure 2.16. a) Dependence of the spin Hall (SHC) and orbital Hall (OHC) conductivity on the electron number n, for the quasiparticle damping rate $\gamma = 0.02$ (taken from Ref. [109]). b) Dependences of the OHC and the SHC on SOC strength λ in Pt, computed using the Born approximation and constant γ approximation (taken from Ref. [108]).

In recent years, the interest in orbitronics has surged due to new theoretical and experimental advances [101–107,110,111]. Recent theoretical studies have expanded beyond transition metals, to include sp metals [110,111], and transition-metal dichalcogenides [114–116]. Moreover, weak SOC metals, that were ruled out in the search for efficient spin Hall materials, have taken a step forward to be considered ideal candidates to explore orbital physics. According to theoretical

calculations, 3d transition metals exhibit orbital Hall conductivities on the order of $\sigma_{OH} \approx 10^3 - 10^4(\hbar/e)(\Omega cm)^{-1}$, which significantly exceed their spin Hall counterparts $\sigma_{SH} \approx 10^2(\hbar/e)(\Omega cm)^{-1}$ (see Figure 2.17) [111,112]. Indeed, σ_{OH} of 3d transition metals are comparable or even larger than σ_{SH} of Pt, where $\sigma_{SH}^{Pt} \approx 10^3(\hbar/e)(\Omega cm)^{-1}$, which is favourable for large SHE.

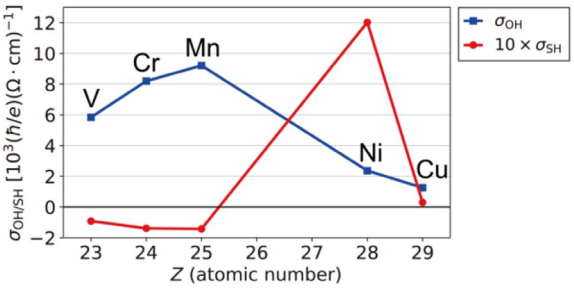

Figure 2.17. σ_{OH} (blue square) and σ_{SH} (red circle) for several 3d transition metals. For clarity, σ_{SH} has been multiplied by a factor of 10. Here V, Cr, Mn have bcc structures, and Ni (ferromagnetic) and Cu have fcc structures. Figure adapted from [111].

Although the generation of orbital currents has primarily focused on the OHE and the orbital Rashba-Eldestein effect (OREE) [117], theorists have also predicted "orbital pumping", which has already been observed experimentally [118]. This phenomenon is analogous to the SP effect (see Sec. 2.1.8 for more details). In the orbital pumping, a precessing magnet can emit a significant orbital current without requiring an associated charge current (see Figure 2.18a) [119].

Its Onsager reciprocal effect, the orbital torque (OT), involves the generation of spin currents from orbital currents [120]. This is possible because magnetization dynamics is governed by the transfer of angular momentum, not only restricted to the spin. However, unlike spin, OAM does not interact directly with the magnetization $\boldsymbol{M}$ because there is no exchange coupling between the OAM and the local magnetic moment, which is dominated by the spin contribution and with negligible orbital contribution [101]. Therefore, to exert a torque on $\boldsymbol{M}$, at least a partial conversion of the orbital current into a spin current is required, which can be achieved with the presence of SOC [119].

Given this, the OT mechanism begins with the generation of orbital currents, which can be achieved efficiently in light metals (LMs) such as 3d transition metals, where SOC is weak. These orbital currents are then absorbed by an adjacent FM layer through orbit-to-spin conversion mediated by SOC. The resultant spin current interacts with the local magnetic moments via exchange coupling, generating a torque (see Figure 2.18b).

An alternative approach is to insert a spacer layer with strong SOC, which can enhance the OT relative to the spin torque by converting the orbital current into a spin current before it reaches the FM, as shown in Figure 2.18c [121].

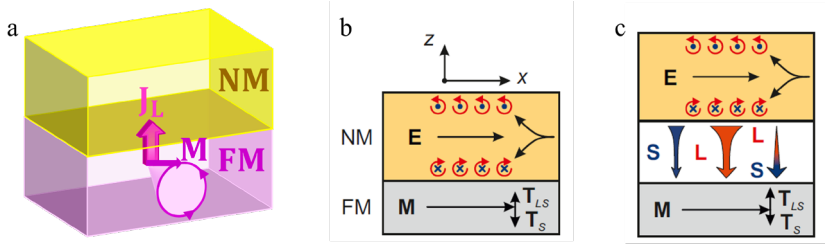

Figure 2.18. a) Schematic representation of orbital pumping. b) Orbital torque. An electric field applied in a NM along x induces an orbital current along z with orbital polarization along y. If SOC is sizable, the orbital current is accompanied by a spin current. The resulting interfacial orbital and spin accumulations produce orbital (Γ_{LS}) and spin (Γ_S) torques on the magnetization $\boldsymbol{M}$ of an adjacent ferromagnet. The strength of Γ_{LS} depends on both the intensity of the orbital current and the SOC of the FM. The schematic shows the direction of the induced spin ($\boldsymbol{S}$) and orbital ($\boldsymbol{L}$) angular momenta when $\sigma_{SH,OH} > 0$. c) The insertion of a buffer layer may increase the orbital torque relative to the spin torque by converting the orbital current (red) into a spin current (blue) prior to their injection into the FM. Panels b and c adapted from [121].

2.2.3 Experimental evidence of orbital currents

Experimental evidence of the presence of orbital currents has been proven through independent studies in the last five years.

Although a large spin-orbit torque (SOT) had been observed in CuO_x, a material with weak SOC, as early as 2016, its origin was not well understood at the time [122]. In 2020, a further enhancement of the SOT was observed in experiments involving this material [123]. The study

showed that adding a CuO_x top layer to a thulium iron garnet (TmIG)/Pt system increased the SOT efficiency (see Figure 2.19). This enhancement was attributed to an additional torque generated by an orbital current arising at the CuO_x layer (see Sec. 2.2.2). This orbital current was converted into a spin current in the Pt layer due to its strong SOC, which then exerted a torque on the adjacent FM layer.

Similar findings have been reported in other CuO_x-based heterostructures [124–129], or NM/FM bilayers using Cr [101], Nb [130], V [131] or Zr [132] as the NM layer, as well as in a systematic study involving heterostructures comprising 3d, 5d and 4f metals [121]. Notably, efficient OTs have also been found in systems where both the NM and FM layers possess weak SOC. For instance, in Ti/Ni bilayers, the observed torques were attributed to the OHE, despite the weak SOC of Ti [106]. In this case, the orbital current generated in the Ti layer is directly injected into the Ni layer, where it exerts a torque on the magnetization. However, when the Ni layer is replaced by a $Ni_{81}Fe_{19}$ (permalloy) layer, known for its high spin transport efficiency, the torque is significantly reduced, highlighting the orbital nature of the effect.

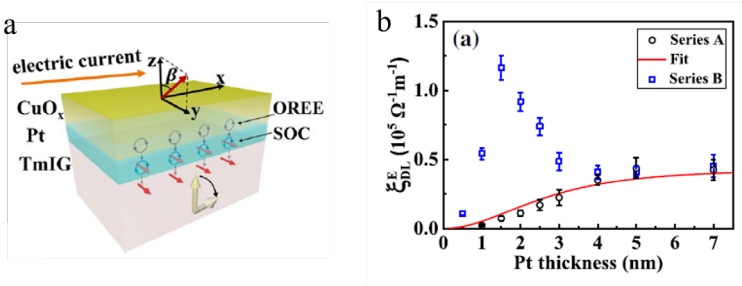

Figure 2.19. a) Schematic illustration of generation of SOTs in TmIG/Pt/CuO_x structures. The OAM (indicated by blue circulations) is generated via the OREE at the Pt/CuO_x interface and injected into the Pt. By the large SOC of the Pt, the OAM is converted to spin angular momentum (indicated by red arrows), which diffuses across the Pt and exerts a torque on the local moments (yellow arrow) of the magnetic TmIG layer. b) Effective SOT efficiency as a function of Pt thickness for sample series A without CuO_x (black circles) and sample series B with CuO_x (blue squares). Figure adapted from [123].

Other approaches use the magneto-optical Kerr effect (MOKE) as a detection method. The OHE was first observed in titanium (Ti) [104] and chromium (Cr) [103], and later in vanadium (V) [133]. MOKE

occurs when a polarized light reflects off a magnetized surface, causing a change in the polarization of the reflected beam. This change can be quantified through the Kerr angle θ_K, defined as the rotation of the polarized light after hitting the sample. In OHE experiments, MOKE serves as a detection tool. A charge current is first applied to induce the OHE (see Sec. 2.2.2.), resulting in the accumulation of OAM at the sample boundaries. This accumulation generates an orbital magnetization that can be detected via MOKE. The interaction of light with this orbital magnetization leads to a Kerr rotation of the reflected light, with an amplitude proportional to the amount of accumulated OAM. The presence of the OHE is manifested by a linear dependence of θ_K on the applied current. This linearity arises because the orbital accumulation induced by the OHE is proportional to the current density, if the orbital magnetization is in the plane of incidence of the light. The Kerr rotation is maximum when the OAM is aligned with the direction of light propagation.

As shown in Figure 2.20a, the linear dependence appears when the charge current is applied along the x-direction and linearly polarized light is incident in the zy-plane. This geometry ensures that the OHE induces an accumulation of OAM in the z-direction which can be detected by MOKE. Conversely, when the sample is rotated, such that the orbital polarization is perpendicular to the direction of the light propagation, Kerr rotation vanishes (Figure 2.20b).

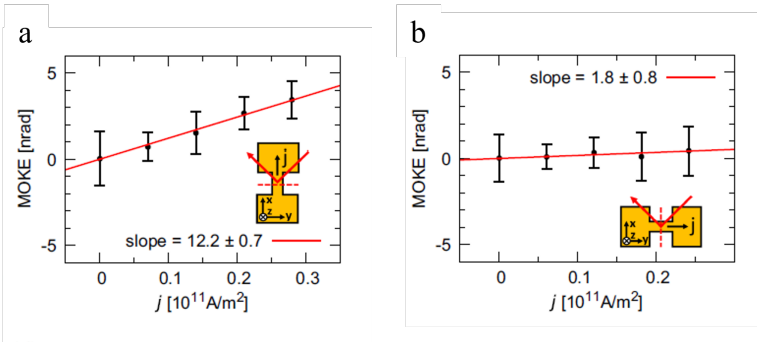

Figure 2.20. MOKE signal on Cr(001) films grown on MgO(001) substrates as a function of curent density: a) for the laser beam incidence along the zy plane and charge current j along z (30 nm sample), b) for device rotated 90º about the surface normal (40 nm sample). Figure adapted from [103].

Another technique proposed to detect OAM induced by the OHE is electron magnetic circular dichroism (EMCD), performed in a scanning transmission electron microscope (STEM), which enables nanometer-scale spatial resolution. EMCD, combined with electron energy-loss spectroscopy (EELS), has been used to directly observe OAM accumulation at the edges of a metallic Ti sample [134]. Under an applied bias, the spin and orbital accumulations induced by the SHE and OHE appear at the top and bottom edges with opposite signs, as revealed by STEM scanning. The combination of EELS, which provides information about the total magnetization, and EMCD, which allows distinguishing between spin and orbital contributions, makes it possible to identify the OHE.

The generation of orbital currents has also been demonstrated through THz emission, resulting from the conversion of light-induced spin and orbital currents into ultrafast charge currents in various bilayers and multilayers containing LMs [105,135,136].

Additional experiments using LMs have confirmed the presence of the OHE. The orbital analogue of the spin Hall magnetoresistance (Sec. 2.1.4) was demonstrated in Ni/Ti bilayers (see Sec. 2.2.4) [137]. Another study provided evidence of the OHE through Hanle magnetoresistance experiments (see Sec. 2.1.5), performed in Mn [102]. In materials with weak SOC, OAM dominates over spin. Consequently, the precession of OAM under an external magnetic field leads to a detectable change in resistance. This phenomenon will be discussed in further detail in Sec. 2.2.5.

Through all these different approaches, orbital Hall conductivities and orbital diffusion lengths of different materials have been measured, as summarized in Table 2.1.

Table 2.1. Orbital diffusion length (λ_{OD}) and orbital Hall conductivity (σ_{OH}) of different 3d transition metals. *From first-principles calculations.

3d metal	ρ_{L0} (μΩ cm)	λ_{OD} (nm)	σ_{OH} $(\hbar/e)(\Omega\ cm)^{-1}$	Technique	Refs.
Ti	~60–100	47 ± 11	---	ST-FMR	[106]

	~60–70	74 ± 24	260–360	MOKE	[104]
	---	7.3	---	EMCD	[134]
V	---	3.61	---	ST-FMR	[131]
	41	0.7	4180*	MOKE	[133]
	41	35	196*		
Cr	19.7	6.6 ± 0.6	---	MOKE	[103]
Mn	225	2.1	55	HMR	[102]
Cu	---	9	---	THz emission	[136]

2.2.4 Orbital Hall magnetoresistance

The orbital Hall magnetoresistance (OMR) is the orbital analogue of the SMR (see Sec. 2.1.4). OMR arises due to the reflection and absorption of orbital currents generated by the OHE in a LM in contact with a FM with an important orbital response. Similar to the SMR, when the direction of the magnetization $\boldsymbol{M}$ is parallel to the direction of OAM polarization ($\hat{\boldsymbol{l}}$), the orbital current $J_{L,int}^{OMR}$ at the interface is reflected, resulting in an extra charge current due to the IOHE. On the other hand, when $\boldsymbol{M}$ is perpendicular to $\hat{\boldsymbol{l}}$, $J_{L,int}^{OMR}$ will be absorbed. Then, depending on the orientation of the magnetization, a modulation in the resistivity of the LM will arise, giving rise to the OMR effect.

The OMR has been reported in the Ni/Ti bilayer [137]. This bilayer is comprised by Ti, that has a significant σ_{OH} as compared to its σ_{SH}, and Ni, which is predicted to show the strongest orbital response among the conventional 3d transition ferromagnetic metals [138].

2.2.5 Orbital Hanle magnetoresistance

The orbital Hanle magnetoresistance is the orbital analogue of the HMR (see Sec. 2.1.5), which arises because the OAM, as the spin, precess under a magnetic field, producing a change in the resistivity and giving

rise to the magnetoresistance effect [61]. Due to the orbital origin of the magnetoresistance, we can observe it in elements with much larger σ_{OH} than σ_{SH}, such as 3d transition metals. HMR from orbital origin has been observed for the first (and only) time in Mn [102]. The phenomenon has also been theoretically investigated in two-dimensional materials, further extending the understanding of the orbital HMR [139].

When a charge current J_q is applied in a NM, both a spin and an orbital angular momentum current are created via the SHE and OHE, respectively (see Figure 2.21a). Focusing on the OAM (spin angular momentum was discussed in Sec. 2.1.5), in the presence of an external H, the OAM precesses due to Hanle effect under $\boldsymbol{H}$, but only when $\boldsymbol{H}$ is not collinear with $\hat{\boldsymbol{l}}$. If $\boldsymbol{H} \parallel \hat{\boldsymbol{l}}$, no precession occurs, leading to a state of minimum ρ_L (see Figure 2.21a). In contrast, if $\boldsymbol{H} \nparallel \hat{\boldsymbol{l}}$, precession takes place which causes dephasing. As a result, the orbital accumulation at the interface is reduced, leading to a decrease in the additional charge current generated due to IOHE (see Figure 2.21b).

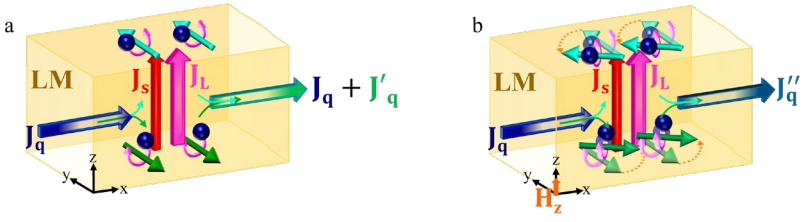

Figure 2.21. Schematic illustration of the Hanle magnetoresistance considering both spin and OAM contributions. a) Influence of the SHE and OHE and their inverse effects in the decrease of the resistivity of a LM thin film, when there is no precession (in absence of magnetic field H or with H along the spin/OAM polarization (y-direction). b) The spin and OAM accumulated at the edges precess due to Hanle effect around a perpendicular H (z- or x-direction, in the sketch, the former example is shown), reducing the extra current generated by the ISHE and IOHE and, thus, increasing the resistivity of the LM thin film.

Since the OAM, as the spin, may undergo precession in presence of $\boldsymbol{H}$, the equations that govern the resistivity in the orbital HMR take the same form as those describing the HMR (see Eqs. (2.25) and (2.26) in Sec. 2.1.5). Now, in a LM with weak SOC, it is expected that the HMR arises predominantly from the OHE rather than from the SHE.

Therefore, we can express the amplitudes $\Delta\rho_1^{HMR}$ and $\Delta\rho_2^{HMR}$ of the orbital HMR as a function of the orbital transport parameters:

$$\Delta\rho_1^{HMR} = 2\rho_{L0}\theta_{OH}^2\left\{\frac{\lambda_{OD}}{t_{LM}}tanh\left(\frac{t_{LM}}{2\lambda_{OD}}\right) - Re\left[\frac{\Lambda}{t_{LM}}tanh\left(\frac{t_{LM}}{2\Lambda}\right)\right]\right\} \tag{2.39}$$

$$\Delta\rho_2^{HMR} = 2\rho_{L0}\theta_{OH}^2 Im\left[\frac{\Lambda}{t_{LM}}tanh\left(\frac{t_{LM}}{2\Lambda}\right)\right] \tag{2.40}$$

where θ_{OH} is the orbital Hall angle, λ_{OD} the orbital diffusion length, t_{LM} the thickness of the light metal (LM), and $\Lambda^{-1} = \sqrt{\frac{1}{\lambda_{OD}^2} + i\frac{g_S\mu_B H}{D_o\hbar}}$ with D_O the orbital diffusion coefficient.

HMR allows to non-invasively access to fundamental orbital transport parameters and to be able to quantify them from the HMR equations.

Because of the form of the orbital HMR equations, the ADMR and FDMR exhibit a characteristic behaviour similar to that discussed in Sec. 2.1.5. An example of orbital HMR can be observed in Figure 2.22 for a Mn thin film [102], where a $\cos^2(\beta)$ modulation related to the HMR geometry appears in *yz*-plane, where H is rotated by an angle β from the out-of-plane direction (z), and no modulation appears in *xz*-plane where H is rotated by an angle γ from the out-of-plane direction (z). For the field scan, the longitudinal resistance increases monotonically with H only if it is applied along x or z, and remains flat when H is parallel to the OAM (see Figure 2.22c). The transverse resistance shows a strong non-linear field dependence when H is applied out of plane (Figure 2.22d). From Eqs. (2.39) and (2.40), λ_{OD} and θ_{OH} are obtained (see Table 2.1).

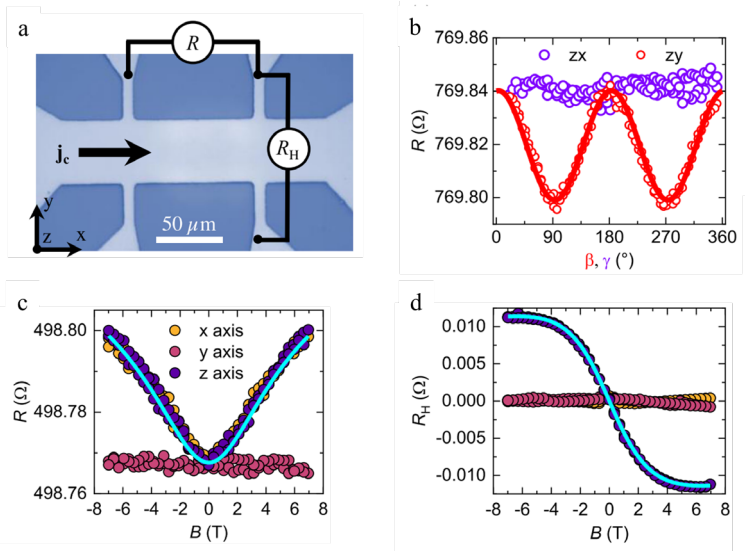

Figure 2.22. Orbital Hanle magnetoresistance in Mn. a) Optical image of a Hall bar device and sketch of the measurement configuration. R is the longitudinal resistance and R_H is the transverse one. b) Longitudinal ADMR measurements in a Mn(6 nm) thin film at 7 T in the H-rotation planes (β, γ). c) Longitudinal resistance and d) transverse resistance in Mn(9 nm) measured with H along the main three axes. The solid line in c) is a fit with shared parameters of Eq. (2.39) to both x- and z-field-scan magnetoresistance. The solid line in d) is a fit of the z-field-scan magnetoresistance to Eq. (2.40). Figure adapted from [102].

Chapter 3
Experimental techniques

In this chapter, we summarize the device fabrication and characterization. In particular, we used Hall bars for the SMR and HMR experiments, non-local devices for the magnon spin transport measurements, and thin films for FMR.

3.1 Device fabrication

The fabrication of the Pt and V electrodes, with a specific design (see Figure 3.1), has been carried out entirely in cleanroom facilities (ISO 5, 6 and 7). In these environments, the concentration of airborne particles per cubic meter is maintained below specified thresholds, according to ISO cleanroom standards.

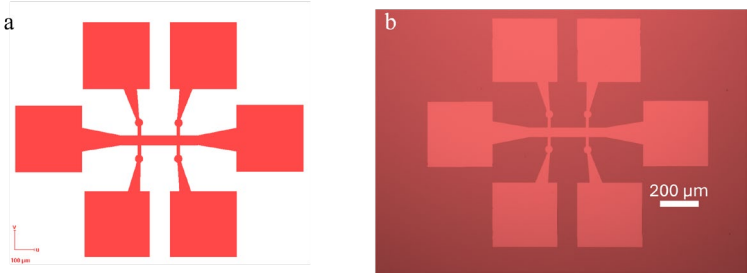

Figure 3.1. a) Pattern design of a Hall bar. b) Final device after the fabrication process.

For the nanofabrication of the devices, we always begin with the cleaning of the substrate. Subsequently, two possible lithography procedures were employed:

- *Lift-off procedure*. This was the one used in most of the samples (see Fig. 3.2). The series of steps is as follows: 1) spin coating of a positive resist, 2) e-beam lithography (eBL) exposure, 3) developing, 4) material deposition, 5) lift-off.
- *Etching procedure*. This was used only for the Hall bars fabricated on YIG substrates. The different steps include: 1) material deposition, 2) spin coating of a negative resist, 2) direct laser writer (DLW) exposure, 3) developing, 4) Ar-ion milling, 5) resist removal.

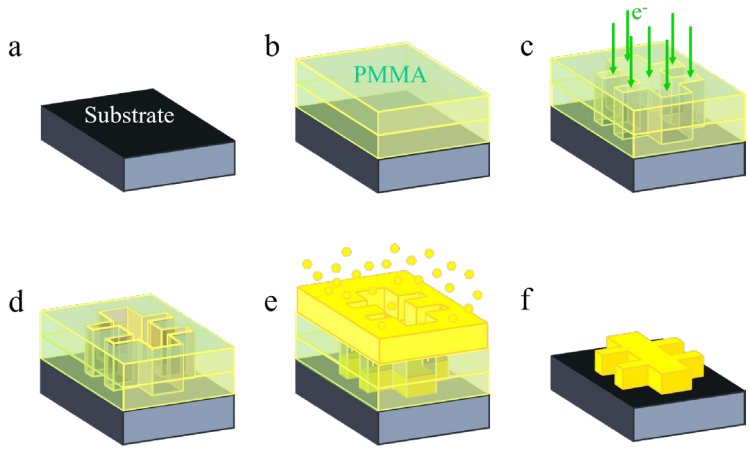

Figure 3.2. Illustration of the fabrication of a Hall bar by the lift-off procedure. a) Cleaning of the substrate. b) Spin coating of a double-layer positive resist. c) Exposure by an electron beam. d) Developing of the exposed resist. e) Deposition of the material. f) Lift-off.

3.1.1 Cleaning of the substrates

The first step in the fabrication is the cleaning of the substrates. The devices are fabricated on top of Pyrex for the magnon transport EuS devices (Chapter 4), whereas Si/SiO_2(150 nm) and GGG/YIG(318 nm), where GGG corresponds to gadolinium gallium garnet, are used for the vanadium Hall bars (Chapter 6).

To start with, the substrate is immersed in acetone, then in isopropanol and finally in deionized water, each step for 5 minutes and in ultrasound. To finish, the substrate is placed in a hot plate at temperatures higher than 100ºC to evaporate the last water drops.

3.1.2 Lithography

3.1.2.1 *Spin coating*

In order to implement the Hall bars and non-local devices, we need to cover the substrate with a resist sensitive to radiation, which will allow us to shape the electrodes of Pt and V (see Figure 3.2b).

The spin coating of the resist is done at a certain speed, acceleration and time to achieve the optimized thickness. For Pyrex and Si/SiO_2 substrates, we use a double layer polymethil methcrylate (PMMA) to

improve the precision of the device structure. PMMA is a positive resist with a long polymer chain that, when exposed to the radiation, in our case an electron beam, it is broken into shorter ones which are easier to be dissolved. In the case of Pyrex substrates, which are insulating, a conductive polymeric layer (Electra), consisting of a polyaniline derivative dissolved in water and isopropanol, is applied on top of the PMMA resist. This protective conductive coating facilitates the dissipation of electrostatic charges generated during electron beam exposure and can be easily removed afterwards by rinsing with water.

In the case of vanadium on top of YIG, a negative resist (AZ® nLof 2020) layer is used in order to follow the etching procedure and have a cleaner interface between vanadium and YIG. In this case, the exposed part becomes extremely difficult to dissolve and is the non-exposed part that is being removed after exposure.

3.1.2.2 *Resist exposure by electron-beam lithography or direct laser writing*

The designed structures (Hall bars and non-local devices) are patterned using either electron-beam lithography (eBL) or direct laser writing (DLW). Most structures are fabricated using eBL, while vanadium deposited on top of YIG is patterned with DLW. In eBL (see Figure 3.2c), a focused electron beam scans the target area of the resist, whereas in DLW, a laser combined with a spatial light modulator is used to project the pattern directly onto the surface.

Due to the different nature of these techniques, the eBL system enables the definition of very fine features, with resolutions below 10 nm, while DLW offers faster patterning of microscale structures.

Prior to exposure, the desired pattern is previously designed with a specific software (see Figure 3.1a). The resist, previously deposited by spin coating, undergoes a change in its chemical properties when exposed to either the electron beam or the laser. The pattern is therefore engraved, enabling the subsequent development.

3.1.2.3 *Developing*

For samples on Pyrex substrates, the exposed resist is first rinsed in deionized water to remove the Electra coating. After exposure, the samples are developed by immersion in a developer solution: methyl

isobutyl ketone (MIBK) for positive resists and AZ® 726 MIF for negative resists, removing the areas that were exposed during either eBL or DLW, as shown in Figure 3.2d.

3.1.3 Thin film deposition

3.1.3.1 *Sputtering*

Pt or V Hall bars and/or non-local devices are grown by magnetron sputtering (see Figure 3.3). The moment at which we perform the deposition depends on the procedure as specified at the beginning of the section.

Sputtering deposition is a common technique to deposit thin films of different materials on substrates. It is based on the bombardment of the desired material, the target, with energetic ions that have been produced by an electric discharge in form of a plasma. In the case of magnetron sputtering, magnetic fields are used to control the behaviour of the ions in the process and enhance the density of the plasma which increases the velocity of the process.

First, an inert gas, normally Ar, is inserted in the system that is made up of positive (anode) and negative (cathode) electrodes. The anodes are the vacuum chamber and the sample holder, while the cathode is the target (magnetron source). Then, a negative voltage is applied between cathode and anode to start the ionization of the inert gas (Ar^+). Deposition is possible because collisions within the plasma accelerate energetic ions, which then strike the target. As a result, momentum is transferred, causing atoms from the target surface to be ejected and deposited onto the surface of the substrate.

The electric discharge responsible for ionizing the Ar atoms can either be continuous (DC) or alternating within the radio frequency (RF) range. DC sputtering enables the deposition of conductive materials (such as Pt or V in our case), whereas RF sputtering allows for the deposition of insulating materials (such as SiO_2 and SiN in our case).

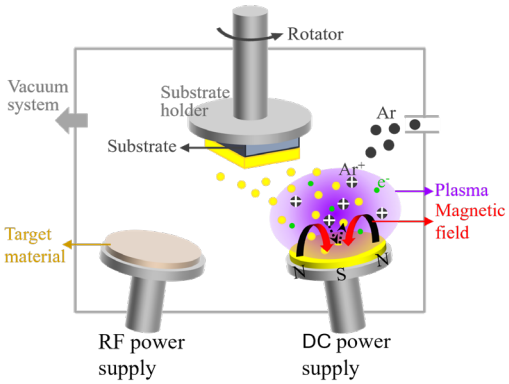

Figure 3.3. Schematic illustration of magnetron sputtering. The dark grey circles represent the inert gas (Ar) that gets ionized (Ar^+) after crashing with the electrons (green circles). Then, the Ar^+ collide with the target material, atoms are expelled (yellow circles), and reach the surface of the substrate, giving rise to the thin film of the desired material.

3.1.3.2 *Electron-beam evaporation*

Electron-beam evaporation was used for the *ex-situ* deposition of the europium sulphide (EuS) thin films at the end of the fabrication process. This step was carried out by our collaborators Dr. M. Ilyn, Prof. C. Rogero, D. Caldevilla Asenjo, S. Kerschbaumer and C. Gonzalez-Orellana from the Materials Physics Center (UPV/EHU-CSIC).

In electron-beam evaporation, the source material is heated and evaporated by a focused beam of high energy electrons emitted from a hot filament, all inside a high-vacuum chamber. The evaporated material then condenses on the substrate, forming a thin film [140].

In particular, EuS was grown by means of sublimation of a stoichiometric EuS powder (99.9% purity) in a commercial e-beam evaporator by cooling the sample holder with liquid nitrogen to prevent interdiffusion of EuS into the (previously fabricated) Pt contacts.

3.1.4 Resist and thin film removal

3.1.4.1 Ar-ion milling

This is a purely physical process based on the phenomenon of sputtering. Ions from an inert gas (Ar) are created by a plasma and accelerated from an ion source toward the surface of the desired substrate to eject atoms from the surface in a controlled manner. This

technique, used during the etching procedure, enables the precise removal of unwanted material.

3.1.4.2 Resist removal

In the etching procedure, this step is performed at the end. The exposed negative resist is removed by immersing the sample in an acetone bath overnight, to ensure complete stripping of the remaining resist.

3.1.4.3 Lift-off

In the lift-off procedure, this is also the last step. The sample is immersed in an acetone bath to dissolve the remaining positive resist of the unexposed areas together with the material deposited on top of it. This process leaves behind only the patterned material directly in contact with the substrate (see Figure 3.2f).

3.2 Characterization techniques

3.2.1 X-ray characterization

X-ray characterization is the use of photons with energy ~125 eV-125 keV to study the atomic and molecular structure of a material [141]. The X-ray techniques, X-ray reflectivity (XRR) and X-ray diffraction (XRD), involve processes of X-rays in and out of the sample.

The X-ray instrument used is a X'Pert from Malvern PANalytical.

3.2.1.1 X-ray reflectivity (XRR)

This technique is used to extract the thickness and surface roughness of the films. It also allows us to calculate the deposition rates of the desired materials in the sputtering system.

XRR is based on the fundamental principles of X-ray reflection an interference. A beam of X-rays is directed onto a flat surface at grazing incidence angles and the intensity of the reflected X-rays as a function of the incident angle is measured. When an X-ray beam strikes a flat surface at grazing angle, part of the beam is reflected from the surface, while the remaining portion penetrates the material and undergoes reflection if the incident angle is greater than the critical angle for total reflection Θ_c (see Figure 3.4a). Then,

interference occurs between the X-rays reflected from the surface of the thin film and the interface between the thin film and the substrate. As a result, a characteristic oscillation pattern in the reflected intensity profile appears, known as Kiessing fringes, first observed in 1931 by Kiessing [142]. The period and amplitude of these oscillations contain information about the thickness, with nanometer precision, density, and roughness of the film layers (see Figure 3.4b).

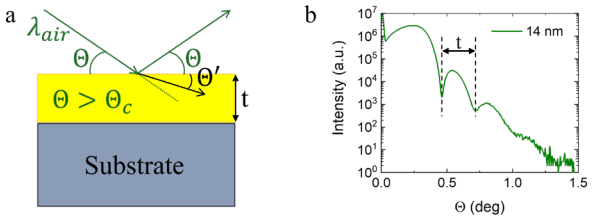

Figure 3.4. a) X-ray reflectivity working principe, where λ_{air} is the wavelength in air and Θ is the incident angle of the X-rays. When the X-rays arrive to the surface, they penetrate the material by diffraction if $\Theta > \Theta_c$. b) XRR for 14-nm-thick V films, showing how to extract film thickness in the sample.

The angular separation between reflectivity fringes, $\Delta(2\Theta)$, in radians, can be used to calculate the thickness $t_{NM,LM}$ of the corresponding layer:

$$t = \frac{\lambda_{x-ray}}{\Delta(2\Theta)} \tag{3.1}$$

which is valid for adjacent fringes well above the critical angle [141].

In addition, the decay of the reflected intensity at higher angles provides a qualitative indication of the surface and interface roughness, with faster damping corresponding to rougher layers.

3.2.1.2 X-Ray diffraction (XRD)

X-ray diffraction is a technique used to determine the crystalline structure of a material. When X-rays strike the sample, they interact with the regularly spaced atoms in the crystal lattice. This interaction causes the X-ray to scatter, changing the direction at an angle ϑ relative to the incident the beam. This is the angle of diffraction. While some

scattered waves cancel each other out through destructive interference, others create a constructive interaction. The condition for constructive interference is described by Bragg's law, which relates the angle of diffraction to the spacing between atomic planes in the crystal d:

$$sin\vartheta = \frac{n\lambda_{x-ray}}{2d} \tag{3.2}$$

By sweeping the detection angle is then possible to get the diffraction spectrum that can be compared to a database to identify the crystallographic phases present in the sample.

3.2.1.3 Atomic force microscopy (AFM)

Atomic force microscopy (AFM) is a surface characterization technique that enables mapping and analysis of the morphology of a wide variety of materials including insulators, conductors, polymers and biological samples. In our case, AFM is employed to analyse the surface texture and evaluate the roughness of the films.

The instrument consists of a sharp tip mounted on a flexible cantilever. As the tip scans the surface, it interacts with the sample through short-range forces, producing a deflection of the cantilever proportional to the interaction force. This deflection is detected by a laser beam that impacts a photodetector which records the signal. Finally, a software processs the recorded signal generating an image of the sample surface.

3.2.2 Electrical measurements

Electrical measurements are carried out in the Physical Property Measurement System (PPMS) developed by Quantum Design (Figure 3.5a). It allows us to apply magnetic fields up to 9 T and control the temperature between 2 K and 400 K.

In order to measure the sample, it is glued to a sample holder (commonly referred to as a *puck)* which is equipped with 8 electrical contact pads. To electrically contact the *puck* with the sample, a wire bonder system developed by West Bond is used. Aluminium wires serve as a connection between the sample and the corresponding contact pads on the puck (Figure 3.5b). Finally, the *puck* with the sample is placed onto the rotator probe (Figure 3.5c) and introduced into the cryostat of the PPMS.

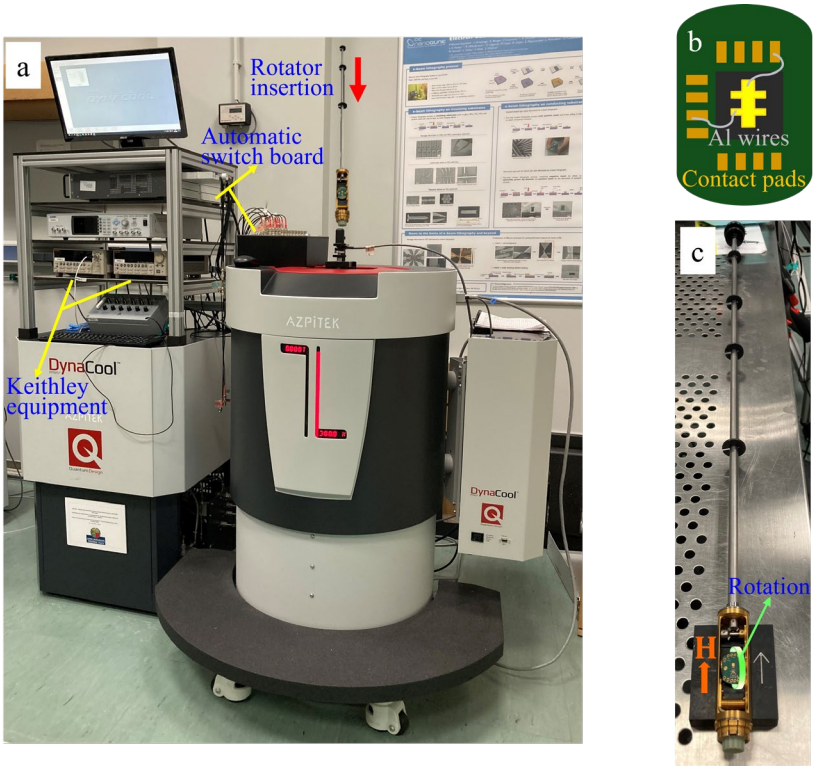

Figure 3.5. a) PPMS setup, including the equipment by Keithley used to apply the current (6221 source) and measure the resulting voltage (2182 nanovoltmeter). It also illustrates the insertion of the rotator probe into the cryostat, which enables angular-dependent measurements under controlled temperature and magnetic field conditions. b) Schematic representation of the sample mounted on the *puck*, showing the aluminium wires bonds connecting the sample's contact pads to the *puck*'s electrical terminal. c) Rotator indicating the orientation of $\boldsymbol{H}$ upon insertion into the PPMS as well as the rotational motion.

The rotator system integrated into the PPMS enables full 360º rotation of the sample under the presence of an applied magnetic field $\boldsymbol{H}$, allowing controlled angular-dependent measurements. Due to the specific rotational mechanism of the rotator, two types of sample holders are required: the *standard puck*, in which the rotation axis lies within the sample plane points out of the sample plane, and the *T-puck*, in which the rotation axis points out of the sample plane (see Figure 3.6). The *standard puck* allows for the application of the magnetic field out-of-plane of the sample as well as for angular sweeps that transition

between in-plane and out-of-plane configurations. In contrast, the *T-puck* enables measurements in which the magnetic field is rotated within the plane of the sample. The use of these interchangeable sample holders makes it possible to apply $\boldsymbol{H}$ along three mutually orthogonal rotational planes relative to the sample, thereby enabling the exploration of its magnetic response. The rotation planes are the xy-plane, where H is rotated by an angle α from the direction of the applied current (x), yz-plane, where H is rotated by an angle β from the out-of-plane direction (z), and xz-plane, where H is rotated by an angle γ from the out-of-plane direction (z) (see Figure 3.7a).

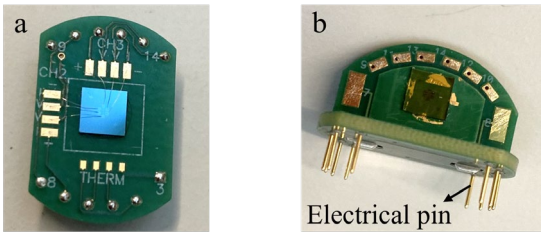

Figure 3.6. a) *Standard puck* with 8 contacts and sample contacted with Al wires. It is used to rotate the magnetic field from in-plane to out-of-plane configuration. b) *T-Puck* showing the electrical pins. This puck enables you to rotate the magnetic field in an in-plane configuration.

Moreover, to apply the current and measure the voltage, we use an automatic switch board which enable us to choose the desired contacts. For the measurement, the current is applied through a Keithley 6221 and the voltage is measured with a Keithley 2182 nanovoltmeter in the longitudinal (V_L) or transverse (V_T) configuration (see Figure 3.7b and Figure 3.7c), using a DC-reversal mode technique also known as delta mode. In delta mode, an alternating positive and negative current is injected, and the voltage is measured every time the polarity of the current changes:

$$V = \frac{V(I+) - V(I-)}{2} \tag{3.3}$$

where $V(+I)$ and $V(-I)$ are the voltages for the positive and negative charge current, respectively. The delta mode measures the linear response of V with I, which is equivalent to the first harmonic signal of an AC lock-in measurement.

Additionally, it is possible to detect the quadratic response of V with respect to I, typically associated with thermal effects arising from Joule heating, which is proportional to I^2. This corresponds to the second harmonic response when using an AC lock-in measurement, and is given by:

$$V = \frac{V(I+) + V(I-)}{2} \tag{3.4}$$

Finally, we can also distinguish between a local voltage V_{LOC} (equivalent to the longitudinal configuration), and the non-local voltage V_{NL}, which is particularly important in the context of magnon transport devices. As sketched in Figure 3.7d, I is applied through one strip, and the voltage response is detected in two configurations. When the voltage is detected along the same strip as the current, it is referred to as the local voltage V_{LOC}. When the voltage is detected in a second strip, separated by a distance d, we denote it as the non-local voltage V_{NL}. Then, the first harmonic response or electrical voltage component is given by:

$$V^{e}_{LOC,NL} = \frac{V_{LOC,NL}(I+) - V_{LOC,NL}(I-)}{2} \tag{3.5}$$

By measuring $V^{e}_{LOC} = V_L$ we study the SMR and HMR, and with V^{e}_{NL} we study the electrically injected magnon currents.

The second harmonic response or thermal voltage component is:

$$V^{th}_{LOC,NL} = \frac{V_{LOC,NL}(I+) + V_{LOC,NL}(I-)}{2} \tag{3.6}$$

By measuring $V^{th}_{LOC,NL}$ we detect the thermally induced magnon currents (also known as SSE) locally (V^{th}_{LOC}) and non-locally (V^{th}_{NL}).

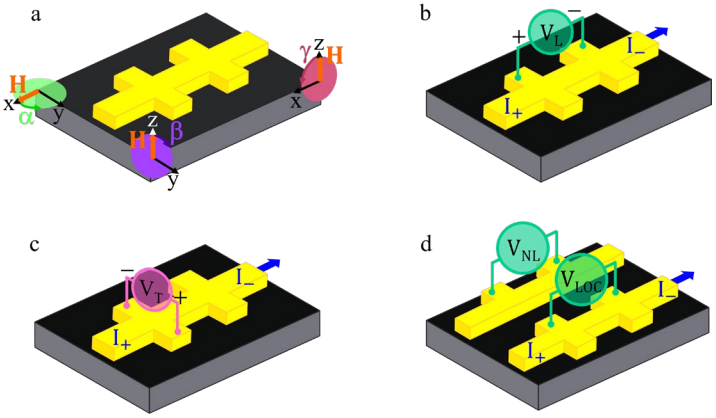

Figure 3.7. a) Rotation configuration for α, β, γ −planes. b) Longitudinal configuration. c) Transverse configuration. d) Local (longitudinal) and non-local configuration for magnon transport devices.

3.2.3 Ferromagnetic resonance measurements

As explained in Sec. 2.1.8, FMR is a versatile characterization technique to study the magnetization dynamics of ferromagnetic materials. To perform the FMR experiments, a vector network analyser (VNA) setup is used in combination with a coplanar waveguide (CPW) that creates microwave magnetic fields operating in a broad frequency range (from 7 to 25 GHz). A schematic of the setup is illustrated in Figure 3.8a.

The VNA is a tool that sends a microwave signal, in our case to excite the magnetization dynamics in the magnetic sample and then analyse the signal received. This allows the VNA to capture the amplitude and phase of the signal in a wide range of frequencies. It measures the scattering parameters S_{21} (transmission) and S_{11} (reflection).

The CPW structure consists of a central conductive strip and two narrow ground electrodes running adjacent and parallel on the same surface of a dielectric substrate (see Figure 3.8b). Our CPW is composed of a ~176-µm-wide signal line (S) separated from the ground conductors (G) by two ~171-µm-wide adjacent air gaps. The sample is placed with the ferromagnetic part facing the CPW, which is placed in between the coils. The CPW is connected on both ends to ports 1 and 2 of the VNA configured in the transmission mode S_{21}.

To perform the FMR measurements, a static (DC) external magnetic field (H_{DC}) is applied in the plane of the sample and a microwave current in the signal line of the CPW produces a microwave magnetic field H_{RF} (see Figure 3.8b). In the resonance condition determined by H_{DC} and frequency, H_{RF} can resonantly excite the magnetic moments in the sample to precess around the direction of the local field [143], as illustrated in Figure 3.8a.

Resonance absorption of microwave power by the sample is seen as a dip in the measured S_{21} spectrum. A typical experimental resonance spectrum of YIG at a resonance frequency of 14 GHz is shown in Figure 3.8c as a function of the in-plane H_{DC}, from where the resonance field (H_{res}) and linewidth (ΔH) can be obtained.

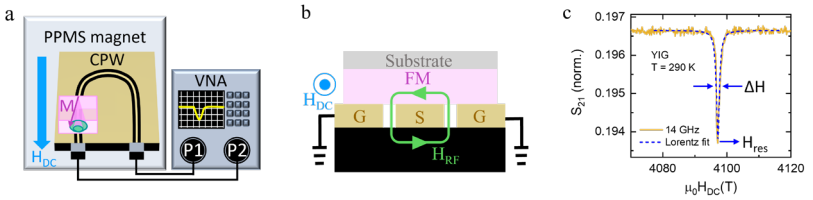

Figure 3.8. a) Experimental VNA-FMR setup with the CPW mounted inside de PPMS magnet and connected to the VNA. The ferromagnetic sample is placed on the CPW, with the magnetization M precessing around H_{DC} and describing a cone that spirals inwards. b) Schematic diagram of the side view of the CPW with the sample on top showing the magnetic field lines winding around the signal conductor (S). c) Experimental resonance spectrum of YIG fits a Lorentzian curve enabling to extract the resonance field (H_{res}) and linewidth (ΔH).

Chapter 4
Magnon currents excited by the spin Seebeck effect in ferromagnetic EuS thin films

A magnetic insulator is an ideal platform to propagate spin information by exploiting magnon currents. However, until now, most studies have focused on YIG and a few other ferri- and antiferromagnetic insulators, but not on pure ferromagnets. In this chapter, we demonstrate that magnon currents can propagate in ferromagnetic insulating thin films of EuS. By performing both local and non-local transport measurements in 18-nm-thick films of EuS using Pt electrodes, we detect magnon currents arising from thermal generation by the spin Seebeck effect. By comparing the dependence of the local and non-local signals with the temperature (< 30 K) and magnetic field (< 9 T), we confirm the magnon transport origin of the non-local signal. Finally, we extract the magnon diffusion length in the EuS film (~140 nm), a short value in good correspondence with the large Gilbert damping measured in the same film.

4.1 Introduction

Magnon-based transport in magnetic insulators presents a promising route for pure spin current manipulation [24,25]. However, to integrate such magnon currents into functional devices, hybrid structures combining a MI and a NM have emerged as ideal platforms (see Sec. 2.1.7) [24], allowing the transfer of spin angular momentum (see Sec. 2.1.2). In such systems, incoherent magnon currents can be excited either electrically, through the SHE, or thermally, via the SSE [24,25,44], while the ISHE can be used for their detection, enabling all-electrical access to spin current physics [25,44].

So far, magnon transport in magnetic insulators has been studied mainly through ferrimagnetic garnets with the prototypical example being YIG, whose exceptionally small Gilbert damping results in a magnon

diffusion length of several microns [50,51,144]. Magnon transport has also been reported in some antiferromagnetic insulators, showing characteristic magnon diffusion lengths of few hundreds of nm [53,54]. Indeed, there is increasing interest in extending the knowledge of magnon transport to other magnetic compounds. For example, recent studies have focused on magnon excitations in van der Waals magnetic insulators [68,145–148]. In this context, SMR measurements on Eu-based insulating ferromagnets have recently demonstrated intriguing spin-transport properties at the interface with heavy metal films, suggesting that they could also be employed as carriers of magnon spin currents [149–151].

Europium sulphide (EuS), one of the few examples of isotropic Heisenberg ferromagnetic insulator [152,153], can be grown as thin films exhibiting the ferromagnetic ground state below the Curie temperature $T_C \approx 18$ K, which can be tuned by chemical doping or strain [154]. Below T_C, it behaves as a soft ferromagnet with extremely small coercive fields, similar to YIG. EuS films have been used to introduce strong magnetic exchange fields within interfacial layers such as metals, superconductors, and topological insulators, and manipulate their electronic phases by the magnetic proximity effect [151,155–166]. Specifically, EuS/Pt interfaces have recently been studied by means of SMR measurements, revealing a strong exchange field into the heavy metal layer, even for polycrystalline EuS films [151].

In this chapter, we demonstrate the propagation of magnon spin currents in a ferromagnetic insulating thin film of EuS. We use Pt nanostructures to generate and detect magnon currents through evaporated polycrystalline EuS films deposited by our collaborators at the Materials Physics Center (UPV/EHU-CSIC). Below T_C of EuS, we show that magnon currents generated by the SSE at the Pt/EuS interface can propagate through the EuS films. We study such an effect by electrically detecting the magnon currents at the Pt/EuS interface considering both the local and the non-local configuration (see Sec. 3.2.2). We study the temperature, magnetic field, and length dependence of the signal, which indicate that thermally-induced magnon currents propagate in the diffusive transport regime in our samples. We extract a thermal magnon diffusion length ℓ_m^{th} of ~140 nm, much smaller than the one observed in YIG, suggesting that magnons are strongly damped in the studied EuS films, in good correspondence

with the measured Gilbert damping α_G (~0.04). Our work further expands the present knowledge of magnon transport to a broader class of materials.

4.2 Experimental details

Pt/EuS heterostructures have been fabricated on top of insulating Pyrex substrates, following the procedure presented in the previous work by our group and collaborators from the Materials Physics Center (UPV/EHU-CSIC) [151]. First, 5 nm of Pt were deposited with DC magnetron sputtering on top of the Pyrex substrate [167]. Subsequently, the Pt/EuS magnon spin transport (MST) devices were defined by e-beam lithography. Each MST device consists of two or three Pt strips (width of 300 nm and length of 70 μm) separated by different distances d (0.8 μm < d < 2 μm), as shown in Fig. 4.1 (MST1 contains d = 0.8 and 1 μm, MST2 includes d = 1.25 μm and MST3 d = 2 μm). Afterwards, 18 nm of EuS were evaporated *ex situ* on top of the Pt contacts, with the deposition method described in Sec. 3.1.3.2 [151]. Since the top surface of the EuS film oxidizes when it is exposed to air, the final film corresponds to around 14 nm of insulating EuS capped by ~4 nm of EuO_x, which is also insulating [168]. An optical image of a representative device is shown in Figure 4.1d.

Transport measurements were carried out using a Quantum Design PPMS covering the temperature range 2 K < T < 300 K. We applied magnetic fields H up to $\mu_0 H$ = 9 T and the sample was rotated within the xy plane (α plane, inset of Figure 4.1a). A DC current I ranging from 4 μA to 100 μA was applied, and the resulting voltage recorded (as sketched in Figure 4.1d). Both the electrical (V^e) and thermal (V^{th}) voltage responses were measured in local $\left(V_{LOC}^e, V_{LOC}^{th}\right)$ and non-local $\left(V_{NL}^e, V_{NL}^{th}\right)$ configurations, as described in Sec. 3.2.2. The magnetic properties of the EuS film have been measured by FMR (see Sec. 3.2.3).

4.3 Results and discussion

We studied the generation and transport of spin angular momentum in EuS films by incoherent magnon currents, which can be driven by non-equilibrium magnon density and temperature gradients [35]. In fact, a magnon spin current can propagate in a magnetic medium according to Eq. (2.9) [36].

In our experiment, we adopted the same measurement configuration used by Cornelissen et al. [50]. The magnon spin transport (MST) devices consist of a EuS thin film deposited on top of the Pt strips. As sketched in Figure 4.1d, a charge current I is applied through a metallic Pt strip (injector) and the voltage response is measured along the same strip (local voltage, V_{LOC}) or at a different strip (non-local voltage, V_{NL}).

The measurements principle is illustrated in Figure 4.1a. The applied I along the x-axis of the Pt wire corresponds to a charge current density $j_{q,in}$ that generates a spin accumulation polarized along the y-axis at the Pt/EuS interface thanks to the SHE. The effects of the interaction between the spin current flowing in the Pt strip in z-axis and the interfacial magnetic layer can be read out in the first order, or *electrical*, response of the system as a voltage $V^{e}_{LOC,NL}$. By measuring V^{e}_{LOC} we study the SMR effect in our samples, that is the modulation of the Pt resistance due to the torque exerted by the magnetization ($\boldsymbol{M}$) of the EuS on the spin current flowing through Pt [56,169]. Moreover, the spin current can also generate magnons at the Pt/EuS interface by spin-flip scattering processes, as sketched in Figure 4.1c. Furthermore, when the magnons diffuse away and reach a second Pt strip, they can transfer spin angular momentum to the Pt electrons due to the same spin-flip scattering process (Figure 4.1c). This produces a spin current through the Pt/EuS interface and, consequently, a voltage in the Pt wire, due to the ISHE. Thus, the electrically injected magnon currents are detected as V^{e}_{NL} in the second Pt wire.

Most important for our work, the applied $j_{q,in}$ also generates Joule heating at the Pt/EuS interface, so that a temperature gradient proportional to the square of the current (I^2) is introduced in the system (Figure 4.1b). The second order or *thermal* response of the system to such a gradient is detected as $V^{th}_{LOC,NL}$. When the thermal gradient appears, the magnon population is driven out of equilibrium and a magnon current can flow between the hot and the cold side of the system (black arrows in Figure 4.1a−4.1c), resulting in the SSE. At the interface with the Pt wire, the magnon spin angular momentum is transferred to the Pt electrons through spin-flip scattering processes (Figure 4.1c), yielding a thermal voltage response $V^{th}_{LOC,NL}$. We note here that the thermal voltage due to the SSE can be detected both locally (V^{th}_{LOC}) and non-locally (V^{th}_{NL}), as thermally-induced magnon currents

(black arrows in Figure 4.1a–4.1c) diffuse through the EuS film [24,40,69].

The geometry of the experiment allows the SMR and magnon-induced voltages to be probed through the Pt wires. We take into account that both phenomena depend on the orientation between the spin polarization $\boldsymbol{s}$ of the electrons in the Pt (fixed along y axis), and $\boldsymbol{M}$ of EuS. For that reason, we saturate $\boldsymbol{M}$ in the plane of the film (xy-plane) with an external magnetic field H (inset of Figure 4.1a), and we rotate it. Thus, since the generated spin current is absorbed by $\boldsymbol{M}$ as a spin-transfer torque if $\boldsymbol{M} \perp \boldsymbol{s}$, SMR results in a $\cos^2 \alpha$ angular dependence when $\boldsymbol{M}$ of the EuS film is rotated in plane (Figure 4.1a) [170]. However, spin-flip scattering processes depend on the scalar product between $\boldsymbol{M}$ and $\boldsymbol{s}$, causing the electrically injected and detected magnon currents to exhibit a $\sin^2 \alpha$ dependence [50]. Finally, since spin-flip only occurs at the detector for the thermal injection, it results in a $\sin \alpha$ dependence [50].

The magnetic properties of the studied EuS film are exemplified in Figure 4.1e and Figure 4.1f, which present the total magnetic moment (m) of the sample as a function of temperature and applied magnetic field, respectively. As shown in Fig. 4.1e, EuS exhibits clear ferromagnetic behavior with a $T_C \approx 19\ K$, in agreement with previous reports [151,154]. The hysteresis loop at 2 K in Figure 4.1f, with a coercive field around 3 mT, confirms the ferromagnetic behavior of the EuS film (see Sec. 4.5.5 for more details) [151].

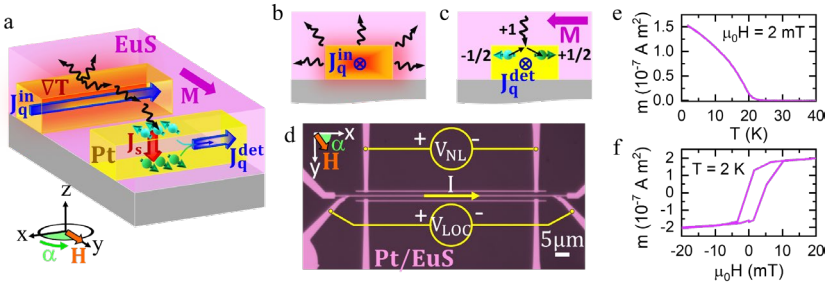

Figure 4.1. a) Schematic representation of the physical processes that occur in the Pyrex/Pt/EuS system. Two Pt strips are embedded in the magnetic insulator (EuS) with magnetization $\boldsymbol{M}$ following the in-plane magnetic field H applied, which can rotate an angle α in the sample plane. When a charge current density $j_{q,in}$ is applied through the left Pt strip, a radial thermal gradient ∇T appears

due to Joule heating, generating non-equilibrium magnons (black arrows) that diffuse away. This leads to a magnon accumulation at the second Pt strip that interact with the electron-spins of the heavy metal creating a spin accumulation that induces a spin current density J_s. Due to the ISHE, J_s is transformed into a charge current density J_q^{det} that can be electrically detected. b) The applied J_q^{in} generates a thermal gradient due to ohmic losses that gives rise to a magnon flow away from the injector. c) Spin-flip scattering process leading to a transfer of spin angular momentum between the Pt electrons and the EuS magnons at the Pt/EuS interface. d) Optical microscope image of a device, showing the measurement configuration where I denotes the charge current applied, and V_{LOC}, V_{NL} the local and non-local voltages measured, respectively. e) Temperature dependence of the magnetic moment measured at a magnetic field of 2 mT in the Pyrex/Pt/EuS sample. f) Magnetic hysteresis loop measured in the Pyrex/Pt/EuS sample at 2 K, with a step size of 2.5 mT.

4.3.1 Angle dependence of the electrical and thermal response

Figure 4.2a presents the ADMR measured in device MST1 as a function of the in-plane angle α, at T = 2 K, below T_C of EuS. We saturate $\boldsymbol{M}$ in plane by applying a small external field ($\mu_0 H$ = 0.1 T). The data are extracted from the electrical local response V_{LOC}^e in order to provide the SMR signal $\Delta\rho_L/\rho_{L0} = [R_L(\alpha) - R_L(90°)]/R_{L0}(90°)$, where $R_L = V_{LOC}^e/I$ is the longitudinal resistance. We observe a clear $\cos^2\alpha$ modulation of the Pt resistance, as expected for the SMR effect [56,58,169]. The signal amplitude (double arrow in Figure 4.2a) is of the order of 10^{-4}, consistent with previous results in EuS/Pt interfaces and comparable to the magnitude of the SMR measured in Pt/YIG interfaces [58,59,151]. FDMR measurements confirm the typical magnetic behavior of EuS, displaying the SMR gap and magnetoresistance peaks in correspondence with the expected magnetization reversal of EuS (see Sec. 4.5.1). The large SMR amplitude and clear correlation with M of EuS indicate an efficient spin transfer at the EuS/Pt interface, in other words, a favorable spin-mixing conductance [47,150,151]. We note that, from the SMR measurements, we can infer the spin transfer efficiency of each device, which we use to normalize the data to compare the response of different devices, as described in Sec. 4.5.2. Hereafter, we label the normalized measured voltage V_{LOC}^* and V_{NL}^*.

Next, we study the magnon currents. For these measurements, a current $I \leq 20$ μA is applied through an injector strip as sketched in the right panel of Figure 4.2b and Figure 4.2c. Note that the injected current is chosen to be small in order to keep the local temperature below the Curie point of the EuS film, as verified by measuring the four-point resistance of the Pt injector. A detailed calibration of the injector temperature with respect to the applied current is provided in Sec. 4.5.2.

First, we measure the thermal local amplitude V_{LOC}^{th} (which we normalize to I^2) as a function of α at $T = 2$ K and $\mu_0 H = 0.3$ T. V_{LOC}^{*th}/I^2 shows a clear $\sin\alpha$ modulation, as presented in Figure 4.2b for device MST1. The $\sin\alpha$ angular dependence is consistent with the symmetry expected for the SSE [50]. A constant angle-independent voltage offset is also present due to other thermoelectric effects [50,51,53,171]. Second, we study the propagation of magnon currents through the non-local voltage. For the electrically injected magnon currents, that follows a $\sin^2\alpha$ dependence, we found no signal in V_{NL}^{e} (Sec. 4.5.3) at any of the measured distances 0.8 μm < d < 2 μm. In contrast, V_{NL}^{*th}/I^2 signal is similar to the local V_{LOC}^{*th}/I^2 with the same clear $\sin\alpha$ modulation expected for the SSE, but with opposite sign, as shown in Fig. 4.2c for MST1 with d = 0.8 μm. The offset signal due to other thermoelectric effects is also present for the non-local case. The $\sin\alpha$ angular dependence, verified at all the measured distances for V_{NL}^{th}/I^2, is consistent with the symmetry expected for SSE-induced magnon currents [50,71,172]. However, the inverted sign suggests that magnon currents at the injector/detector strips flow in opposite directions (Figure 4.2b and Figure 4.2c). In fact, such a sign change is expected to occur between the SSE-induced magnon currents measured locally and non-locally, due to the redistribution of the magnon population induced by Joule heating [70,173,174]. As Joule heating depletes the magnon distribution at the injector site, the magnon currents are expected to flow towards (away from) the detector (the injector) as also illustrated by the direction of the black arrows in Figure 1.1, Figure 4.1b and Figure 4.1c [36,70,173]. For all the devices measured, we observed a positive local V_{LOC}^{th}/I^2 amplitude and a negative non-local V_{NL}^{th}/I^2 amplitude.

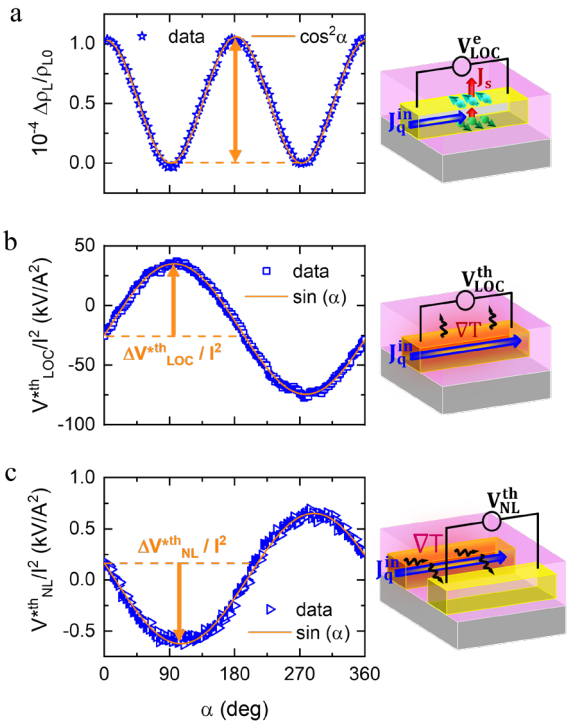

Figure 4.2. Data corresponds to device MST1. Representative a) ADMR of the SMR at a fixed magnetic field of $\mu_0 H$ = 0.1 T. b) Local SSE and c) non-local SSE at 0.8 μm, both at $\mu_0 H$ = 0.3 T, where the voltage is normalized to the square of the applied current. The measurement temperature is 2 K and the current applied is 20 μA. The arrows indicate the amplitude of the signal. A schematic illustration of the effect measured is included on the right side of the corresponding panel.

All things considered, the Pt/EuS devices reveal a magnon-induced response to Joule heating, consistent with the symmetry of the SSE. The absence of an analogue signal in the non-local electrical response V_{NL}^{e}, in contrast, suggests that the magnon population redistribution induced by the spin-flip scattering process at the injector Pt/EuS interface is too small to produce a measurable signal at the detector. We note here that V_{NL}^{e}/I has been reported to vanish as the temperature is lowered below 50 K in Pt/YIG interfaces by different groups [71,175,176]. Thus, the absence of a signal V_{NL}^{e}/I^2 for our samples is expected in the measured temperature range.

4.3.1.1 Temperature dependence

Subsequently, we analyze the temperature dependence of the SMR, local SSE and non-local SSE amplitudes (defined in Figure 4.2), which are presented in Figure 4.3 for devices MST1 and MST3. In all cases, the amplitude of the signal is maximum for the lowest temperature measured (2 K) and decreases with increasing temperature. However, we observe a clear difference between the SMR curve and the thermal amplitudes V_{LOC}^{*th}/I^2 and V_{NL}^{*th}/I^2, as can be observed in Figure 4.3d. The temperature dependence of the SMR amplitudes (Fig. 4.3a) follows the expected trend vanishing as the temperature is raised above the Curie point of the EuS film (see Figure 4.1e and Figure 4.12). In fact, we note here that we can measure an SMR signal even above the T_C of the EuS films. The presence of such a finite SMR response above T_C is a consequence of the sensitivity of the SMR to the magnetic correlations [177], which are present even above T_C in our films, according to our VSM characterization (Sec. 4.5.5). The observed temperature dependence of SMR in our EuS thin films can be fully explained in terms of the microscopic theory developed by Zhang et al. [151,178]. Instead, the temperature dependence of V_{LOC}^{*th}/I^2 (Figure 4.3b) and V_{NL}^{*th}/I^2 (Figure 4.3c) shows similar trend with a substantially different decrease from the SMR curve as T_C is approached (Figure 4.3d). Such temperature dependence may seem surprising for SSE-induced thermal voltages, for which the SSE theory predicts a linear dependence with the system magnetization [179]. However, a similar behavior has been reported in other experimental studies of the SSE at low temperatures [71,175] and can be qualitatively understood with the following considerations. First, the Joule-heating-induced temperature gradient is very likely temperature dependent, as the thermal conductivities of Pt, EuS and the Pyrex substrate may strongly change and at different rates as the temperature is lowered. Second, the Gilbert damping of the EuS film also varies at such temperatures (see Figure 5.6) due to the very low T_C of the films, which consequently affects the propagation of magnon currents. Elaborating a model that captures such temperature dependent effects on the measured thermal voltages is a challenging task, which goes beyond the scope of this work. Instead, we remark that all the measured signals disappear above the T_C of the EuS film, confirming the magnetic origin of the studied voltages.

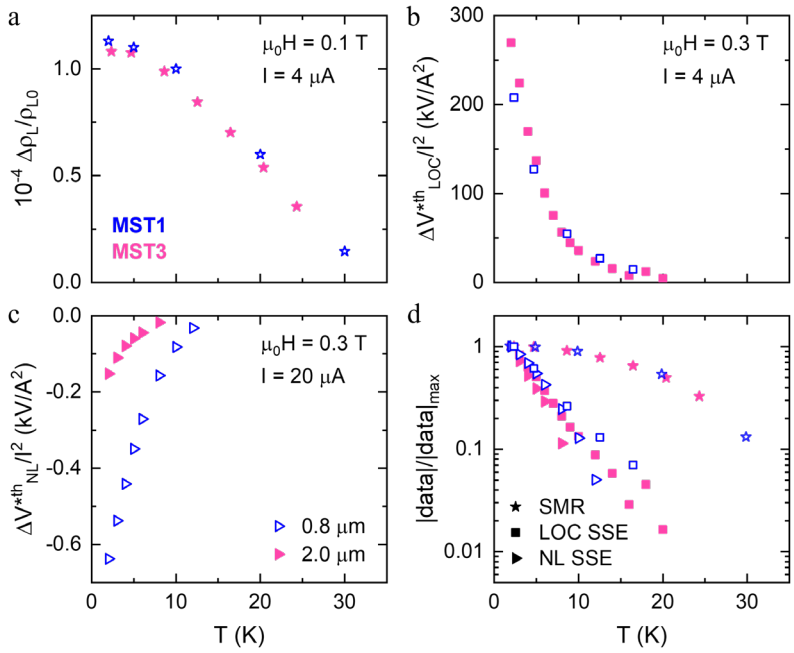

Figure 4.3. Data corresponds to devices MST1 (blue open symbols) and MST3 (pink solid symbols). a) SMR amplitudes (as defined in Figure 4.2a) at $\mu_0 H$ = 0.1 T and I = 4 μA, b) local SSE amplitudes (as defined in Figure 4.2b) at $\mu_0 H$ = 0.3 T and I = 4 μA, and (c) non-local SSE amplitudes (as defined in Figure 4.2c), at $\mu_0 H$ = 0.3 T and I = 20 μA for two different distances, as a function of temperature. d) Comparison of SMR, local SSE and non-local SSE amplitudes normalized to their maximum values.

4.3.1.2 Magnetic field dependence

We also examine the magnetic field dependence of the SMR, local SSE and non-local SSE amplitudes, as illustrated in Fig. 4.4. Initially, both the SMR and SSE signals increase as ***M*** of the system develops, since both effects are related to the interaction of the spins of the electrons in Pt with the magnetic moments in the magnetic layer; but as ***M*** continues to grow their behavior diverges. The SMR response tends to saturate with the magnetic field (Figure 4.4a), in correspondence with the saturation of ***M*** in the EuS films. Note here that the saturation field of

EuS is much higher than the observed coercive field (Figure 4.1f), as already observed in films of EuS deposited at room temperature [156,180]. In contrast to the SMR, both SSE curves (Figure 4.4b and 4.4c) reach a maximum at $\mu_0 H \approx 0.5$ T, followed by a gradual reduction of the SSE amplitude for higher magnetic fields. Such a decay is characteristic of SSE-induced voltages, for which the opening of the Zeeman gap affects the magnon population. According to the SSE theory, when the Zeeman energy $g_S \mu_B H$ is larger than the thermal energy $k_B T$ (where k_B is the Boltzmann constant), magnons cannot be thermally excited, leading to the suppression of the local SSE [181–183]. More interestingly, we note that the local SSE signal suppression at the maximum applied field ($\mu_0 H$ = 9 T) is almost 50% of the maximum signal whereas non-local SSE signal suppression reaches 80%, as is shown in Figure 4.4d. Such a difference can be accounted for by the distinct way magnon currents reach the EuS/Pt interface in the local and non-local case. In fact, the magnon-induced non-local voltage should decay exponentially on the scale of the magnon diffusion length, in contrast to the local voltage case. Therefore, as the magnon diffusion length is also suppressed when the magnetic field is increased, a stronger suppression of the signal should be expected for the non-local case [184].

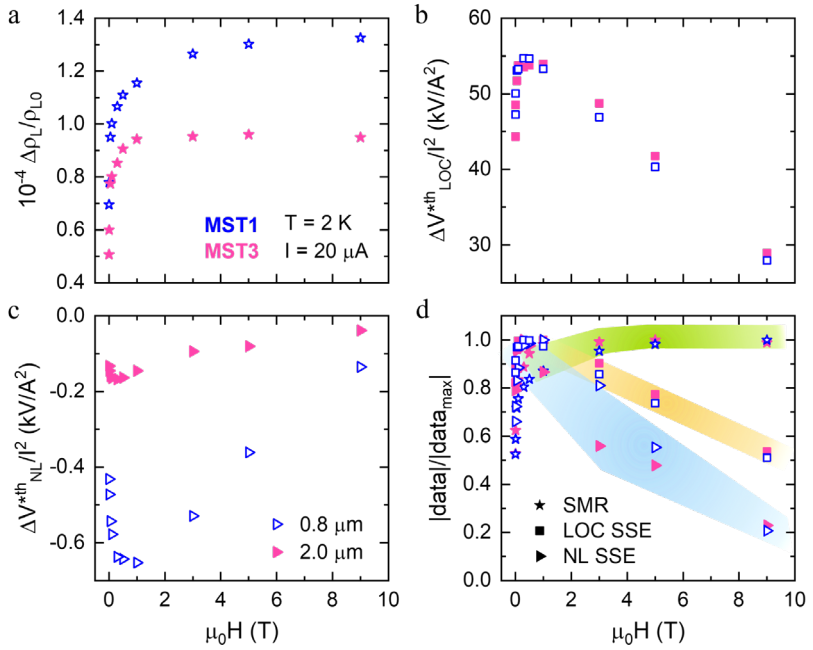

Figure 4.4. Data corresponds to devices MST1 (blue open symbols) and MST3 (pink solid symbols). a) SMR, b) local SSE, and c) non-local SSE amplitudes (as defined in Figure 4.2) as a function of the magnetic field at T = 2 K and I = 20 μA. d) Comparison of SMR, local SSE, and non-local SSE amplitudes normalized to their maximum values. Coloured shadows are a guide to the eye, being green for the SMR amplitudes, orange for the local amplitudes and blue for the non-local amplitudes.

4.3.1.3 Magnon diffusion length

Finally, we study the dependence of the non-local SSE amplitude on the injector-detector distance *d,* to unravel the mechanism by which the magnon currents propagate through the EuS medium. As shown in Figure 4.5, the data can be fitted with an exponential decay law, characteristic of thermally-generated magnons in the relaxation regime [50,72]. Moreover, we note that the data could not be fitted by power laws, indicating that the signal is not driven by the radial decay of a thermal gradient through the sample, but by the redistribution of the magnon population (see Sec. 4.5.4). From the exponential fit, we extract a magnon diffusion length ℓ_m^{th} = 140 ± 30 nm at 2 K and 0.3 T. This value is of the same order as the one reported by Gao *et al.* in the

ferrimagnet TmIG, where a 15-nm-thick film results in ℓ_m^{th} = 300 nm at 0.5 T and room temperature [185]. In comparison to the best YIG samples, where $\ell_m^{th} \sim 7$ μm at low temperatures in a 210-nm-thick film and the electrical magnon diffusion length $\ell_m^e \sim 3$ μm in 10–15-nm-thick films [51,175], the EuS value is more than one order of magnitude smaller. However, we note here that several studies in YIG films reported ℓ_m^{th} values at room temperature comparable with the ℓ_m^{th} value that we observe in EuS [186–189]. At this point, it is important to consider the Gilbert damping (α_G) since it is linked to the magnon diffusion length. Reducing α_G implies increasing the magnon spin-relaxation time and, therefore, the magnon diffusion length [25,36]. To verify this relationship, we performed FMR measurements in the very same sample where the measured devices are located. Our results in the EuS thin film yields $\alpha_G^{EuS} = 4 \times 10^{-2}$ at 2 K (see Sec. 5.5.2), which is two orders of magnitude higher than the case of YIG thin films ($\alpha_G^{YIG} \sim 10^{-4}$) [50,51], in agreement with the difference observed in the magnon diffusion length.

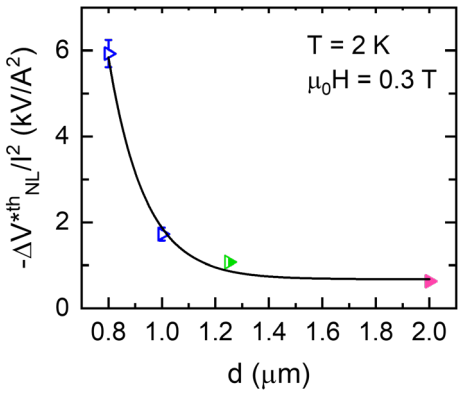

Figure 4.5. Amplitude of the non-local SSE as a function of injector-detector separation distance measured at T = 2 K, $\mu_0 H$ = 0.3 T and I = 4 μA. Black solid line is a fit to an exponential decay.

4.4 Conclusions

To summarize, we demonstrated the transport of incoherent magnon currents in polycrystalline films of EuS. Below T_C, we observe a

thermally-induced response in both local and non-local transport measurements. Considering the angular, temperature and magnetic field dependence of such signals, we ascribe the measured thermal voltages to the SSE. By studying the length dependence of the non-local transport signal, we extract a magnon diffusion length of ℓ_m^{th} = 140 ± 30 nm at 2 K and 0.3 T. This value, short compared to other studied materials such as YIG, correlates well with an enhanced Gilbert damping caused by the polycrystalline structure of the studied EuS films. While we expect that a significantly smaller Gilbert damping in epitaxial EuS films could lead to an improvement of the magnon diffusion length, we highlight the observation of magnon currents propagating even through a polycrystalline ferromagnetic insulator film, as compared to the case of YIG films. Despite the relatively short ℓ_m^{th} observed, our work shows that the transport of spin currents by incoherent magnons through EuS films should be taken into account when studying EuS-based heterostructures. As for perspectives, our results evidence the opportunity of studying the interaction between magnon currents and superconductivity in systems comprising, for example, superconductor/EuS interfaces, following recent experimental and theoretical works [190,191]. Moreover, as sizeable thermoelectric effects may occur in spin-split superconductors, such as Al/EuS bilayers, the role of the observed SSE could be further explored in such a context [192–195].

4.5 Appendices

4.5.1 Longitudinal magnetoresistance measurements

Figure 4.6a shows a characteristic longitudinal FDMR measurement performed in device MST2 at T = 2 K with the magnetic field applied in x and y direction. A clear gap appears between H_x and H_y curves with a peak (in H_y) or dip (in H_x) around zero field which corresponds to the reversal magnetization of EuS and follows the SMR behavior for in-plane magnetic fields [151]. Figure 4.6b shows the ADMR measurement for the same device at T = 2 K and $\mu_0 H$ = 0.1 T, where

the amplitude of the signal corresponds to the magnitude of the FDMR gap at the same magnetic field.

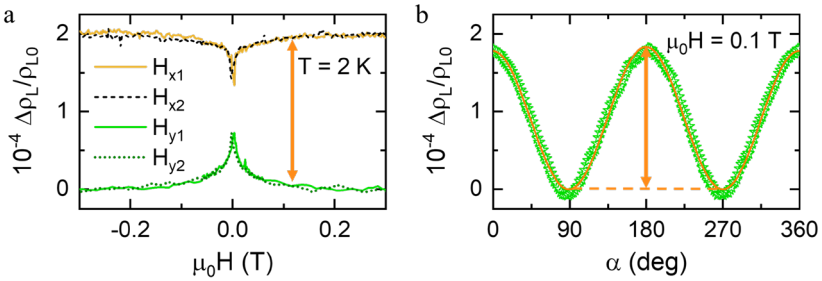

Figure 4.6. Longitudinal measurements of the a) FDMR at T = 2 K and b) ADMR in α plane at T = 2 K and $\mu_0 H$ = 0.1 T in device MST2. The orange line is a $\cos^2 \alpha$ fitting. The double arrows in a) and b) mark the same SMR amplitude $\Delta\rho_L/\rho_{L0}$.

4.5.2 Current-dependent measurements

Figure 4.7a shows the ADMR measurement performed for each device (MST1, MST2 and MST3) at I = 4 μA, $\mu_0 H$ = 0.1 T and T = 2 K. The different SMR amplitude among the devices implies a different spin transfer at the EuS/Pt interface (i.e., a different effective spin-mixing conductance). Therefore, in order to normalize the measured voltage $V_{LOC,NL}$ at a given current, we use the following formula:

$$(V^*_{LOC,NL})_{MSTx} = (V_{LOC,NL})_{MSTx} \cdot \frac{(\Delta\rho_L/\rho)_{MST2}}{(\Delta\rho_L/\rho)_{MSTx}} \qquad (4.1)$$

where $\Delta\rho_L/\rho$ is the amplitude of the SMR signal and $MSTx$ a device. As shown in Figure 4.7b, the amplitude of the SMR signal decreases as the current is increased.

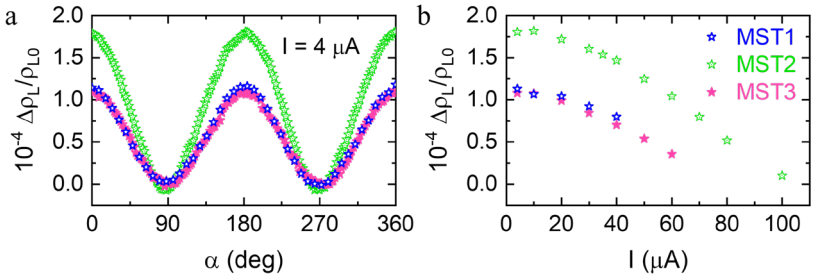

Figure 4.7. Data corresponds to devices MST1 (blue open stars), MST2 (green open stars) and MST3 (pink solid stars). a) ADMR at T = 2 K, $\mu_0 H$ = 0.1 T and the smallest current applied (4 μA). b) Current dependence of the ADMR amplitude at T = 2 K and $\mu_0 H$ = 0.1 T.

Since the injected current heats up the Pt injector and the T_C of the EuS is low, we calibrate the temperature of the injector to stay below T_C. To do so, first we have measured the temperature dependence of the Pt at the lowest current applied (4 μA), a representative curve for device MST2 is shown in Figure 4.8a. Then, from the minimum of the SMR curve at higher currents, up to 100 μA, we estimate the effective temperature of the system (see Figure 4.8b and Figure 4.8c). This way we make sure that we are not above the Curie temperature of the EuS, neither increasing too much the temperature of the system. As shown in Fig. 4.8c, a linear dependence between the applied current and the effective temperature is found. We ascribe the linear relationship not only to Joule heating, which is proportional to I^2, but also to the heat removed from the sample surface by the cooling capacity of the He-vapor based cryostat, which is also strongly temperature dependent below 20 K.

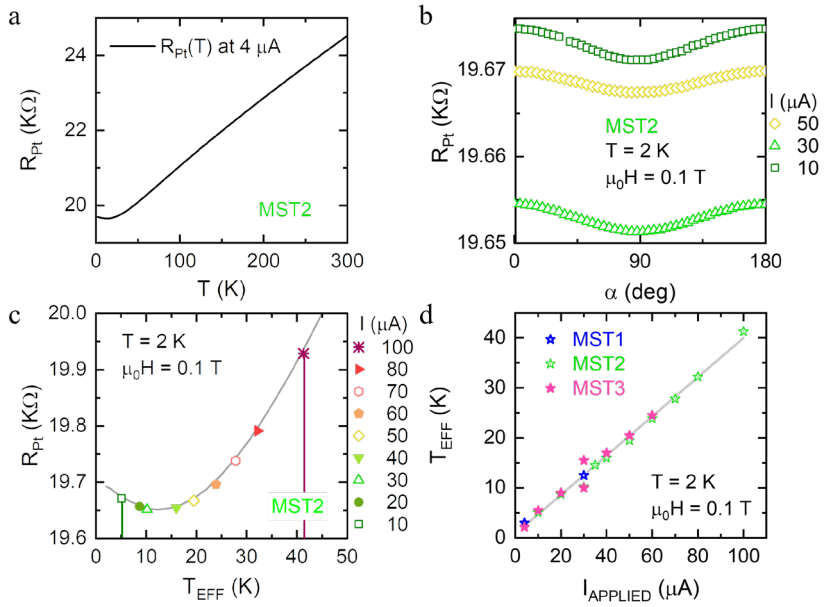

Figure 4.8. a) Resistance of Pt as a function of temperature at I = 4 μA measured in the longitudinal configuration. b) ADMR measurements in α plane for I = 10, 30 and 50 μA. The minimum of the signal (at α = 90º) changes with the applied current. The SMR amplitude decreases with increasing applied current, which can be better seen in Fig. 4.7b and 4.7c. c) Correspondence between the resistance of Pt as a function of temperature at 4 μA (grey line) and the minimum of the SMR curves measured at different currents (colored symbols). Data in panels a), b), and c) correspond to device MST2. d) Relation between the current applied and the effective temperature [extracted from panel c) for the exemplary case of MST2]. The same linear relation (grey solid line) is obtained for the three devices studied (MST1, MST2, and MST3).

Moreover, due to the relatively low T_C of the EuS films, the second harmonic voltage is particularly affected by Joule heating. As can be seen in Figure 4.9, the voltage versus I^2 characteristics reveals two competing regimes. At low currents, we see an increase of voltage with the squared current, but as we continue increasing the current, the signal reaches a maximum and starts decreasing. This is most likely due to overheating of the EuS layer, and in consequence, reducing the

magnetization of the film. For that reason, we keep at $I \leq 20$ μA for the local and non-local measurements.

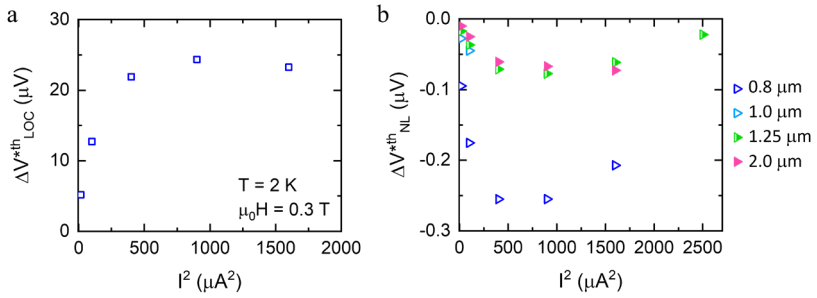

Figure 4.9. Amplitude of the a) local SSE and b) non-local SSE as a function of the square of the current, at 2 K and 0.3 T.

4.5.3 Electrical excitation of magnons

The electrical excitation of magnons through the non-local voltage V_{NL}^{e} have been verified for different injector-detector distances and no signal has been found. A representative measurement for device MST1 is shown in Figure 4.10, in which we are not able to detect any $\sin^2 \alpha$ modulation expected for the electrically-driven magnons. The magnon population decreases as we approach zero temperature and thus the magnon accumulation and V_{NL}^{e}vanishes [71,175,176]. The absence of an electrically-driven signal can thus be explained by taking into account the range of temperatures involved (below ~ 30 K) as well as the fact that V_{NL}^{e} is linear with the applied current (while V_{NL}^{th} is quadratic with the current, leading to larger values above the detection limit).

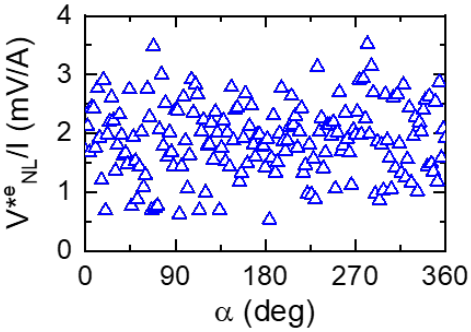

Figure 4.10. Angular-dependent non-local signal detected for electrically-injected magnon currents at d = 0.8 μm, T = 2 K, I= 20 μA and $\mu_0 H$ = 0.3 T for device MST1.

4.5.4 Thermal excitation of magnons

Different regimes have been proposed for the propagation of magnons [50,72,173]. At short distances, $d \ll l_m^{th}$, the system is in the diffusive regime, and it decays as $1/d$. Then, for higher distances we enter the exponential decay or relaxation regime. Finally, for $d \gg l_m^{th}$ the system enters the $1/d^2$ regime, where the signal reduction no longer depends on l_m^{th}. Figure 4.11 shows different fittings according to these three regimes. From here, we conclude that the best fit is found for the exponential decay.

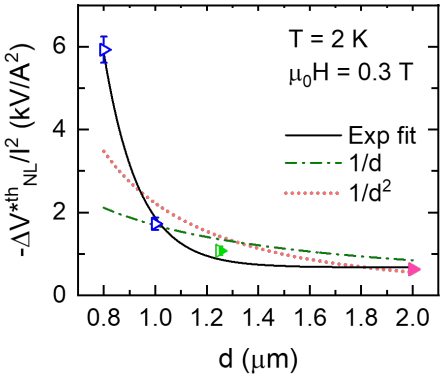

Figure 4.11. Amplitude of the non-local SSE as a function of the injector-detector separation distance measured at T = 2 K, $\mu_0 H$ = 0.3 T and I = 4 μA. Black solid line is a fit to an exponential decay, green dashed line corresponds to $1/d$ fit and red dotted line to $1/d^2$ fit.

4.5.5 Magnetic characterization

The magnetic properties of the EuS thin film are determined by the vibrating sample magnetometry (VSM) and ferromagnetic resonance (FMR) techniques. Figure 4.12a shows the temperature dependence of the EuS magnetic moment (m) for different applied magnetic fields. EuS shows clear ferromagnetic behavior with a broad transition to the paramagnetic state. From the temperature derivative of m, we found a Curie temperature $T_C \approx 19$ K for an applied magnetic field of 20 Oe [151,196]. Besides, an increase in the magnetic field applied shifts the transition to the paramagnetic state towards higher temperatures. The hysteresis loops recorded between 2 K and 30 K show very low coercive fields, around 3 mT at 2 K (see Figure 4.12b), supporting the soft ferromagnetic behavior of the EuS films also observed in FDMR measurements (Figure 4.6a). For the probed magnetic field range, the magnetization increases with field, and we do not observe saturation.

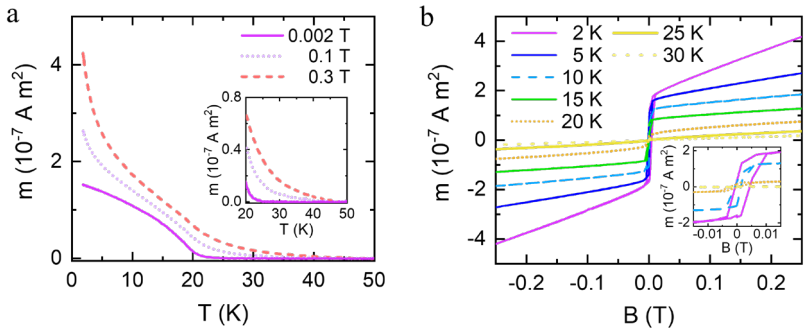

Figure 4.12. a) Magnetic moment of EuS thin film as a function of temperature for different applied magnetic fields $\mu_0 H$ = 2 mT, 0.1 T and 0.3 T. b) Hysteresis loops measured at different temperatures from 2 K to 30 K with zoom to observe the small field regime, note that the serrated shape is due to the step size of 2.5 mT used during the measurement.

Chapter 5
Gilbert damping in EuS thin films by ferromagnetic resonance spectroscopy

The understanding of magnetization dynamics is critical for the future applicability of magnetic devices. Specifically, materials with low magnetization damping are required to achieve low energy loss, high sensitivity and long spin-wave propagation. Despite the early interest in EuS, its magnetization dynamics have remained largely unexplored, with only a few studies dating back to the 1960s, and limited to bulk crystals. In this chapter, we advance the understanding of EuS thin films by employing ferromagnetic resonance spectroscopy, which enables us to investigate the dynamics of magnetization. In the frequency range from 7 to 25 GHz, we analyse the full ferromagnetic regime of EuS by varying the temperature from 2 K to 30 K. We find that the Gilbert damping of EuS thin films is strongly influenced by film thickness, but only slightly affected by crystallinity, at least up to 40 nm. We attribute the thickness dependence to the influence of structural and chemical defects present at the substrate/film interface. At the lowest measured temperatures, we find Gilbert damping values comparable to those of yttrium iron garnet and permalloy films within the same temperature range.

5.1 Introduction

FMR spectroscopy is a versatile characterization technique to study the magnetization dynamics of ferromagnetic materials [82]. It allows for the investigation of magnetization precession and the associated energy dissipation, providing key parameters such as saturation magnetization and damping in thin magnetic films and magnetic heterostructures [80,81,85].

For many applications, including filters and generators, materials with low magnetization damping are essential. In metals, spin excitations are strongly attenuated due to significant viscous damping [24,75–78]. In contrast, magnetic insulators typically exhibit low damping as spin scattering from conduction electrons is absent [24,79]. Within this class of materials, iron-based garnets have dominated the research field of

insulator spintronics, largely due to YIG, which has been known since 1950 to exhibit the lowest Gilbert damping, $\alpha_G \approx 10^{-5}$ in bulk crystals [79,197]. However, YIG-based systems generally require epitaxial growth on a specific crystalline substrate, typically GGG [79]. Moreover, although YIG has low α_G at room temperature even in thin films, its damping increases significantly at low temperatures. This is mainly because the substrates required for epitaxial growth exhibit magnetic losses that are inversely proportional to temperature, resulting in an increase in α_G as temperature is lowered [198–203]. Consequently, the low temperature α_G of YIG becomes comparable to that of metallic materials such as Fe [92], CoFeB [77] or permalloy [204].

Since low temperatures provide an excellent operating environment for quantum technologies and superconducting spintronics, understanding the low-temperature behavior of a broader class of materials will be of benefit for future applications [205–207].

Another notable magnetic insulator with favourable operating conditions at cryogenic temperatures is EuS, a ferromagnet below its T_C of 16.5 K, with a high magnetic moment of 7 μ_B per Eu atom [152]. Since the 1960s, EuS has been extensively studied as a model system for the classical Heisenberg ferromagnet, particularly in terms of its magnetization and spin dynamics [208–212]. Early experimental studies were conducted on single crystals of EuS [209–212]. Notably, even the phenomenological damping constant λ_{LL} first introduced by Landau-Lifshitz [73], which relates to Gilbert damping by Eq. (2.33) [74], was measured at that time. M.C. Franzblau *et al.* reported a value of $\lambda_{LL} = (1.9 \pm 0.09) \times 10^8$ rad/sin EuS pellets, corresponding to $\alpha_G = 7 \times 10^{-4}$ [212], thereby validating the Landau-Lifshitz damping mechanism.

More recently, EuS thin films have shown their advantage when designing heterostructures comprising EuS-based interfaces. In such systems, EuS films can induce an extremely strong magnetic exchange field at interfaces with a wide range of materials including metals [151,196], superconductors [159,161,213], semiconductors [160,164], and topological insulators [214]. This strong interfacial exchange enables control over the electronic properties of adjacent layers, opening new pathways for spintronic

applications. Therefore, extending the understanding of magnetization damping from bulk EuS crystals to thin film systems is essential for assessing their potential for device applicability.

In this chapter, we perform FMR measurements to investigate the magnetic properties of EuS thin films and their dependence on crystallinity and thickness. Specifically, we compare polycrystalline EuS films grown on top of amorphous Pyrex substrates with epitaxially grown EuS films deposited on InAs (001) substrates. We found the smallest $\alpha_G \approx 10^{-3}$ for the 40-nm-thick epitaxial EuS, comparable to YIG pulsed-laser-deposited on GGG substrate [215]. The Gilbert damping of such EuS films decreases with temperature and can be within the 10^{-3} range in both polycrystalline and epitaxially grown films. By considering films of different thickness, we observe that α_G tends to be reduced for thickner films, while the bare magnetization is mostly unaffected. Our results will help uplifting the integration of FI interfaces in magnonic and spintronic devices.

5.2 Experimental details

EuS thin films with thicknesses between 20 nm and 60 nm were grown by means of sublimation of a stoichiometric EuS powder in a e-beam evaporator on either Pyrex or InAs (001) substrates (see Sec. 3.1.3.2). The EuS films were grown keeping the substrate at liquid nitrogen temperature. The different substrates result in different structural properties of the EuS films. EuS/Pyrex films exhibit polycrystalline morphology [151], whereas EuS/InAs films grow epitaxially along the (001) crystallographic direction, although an amorphous layer of about 5 nm of thickness is formed between the InAs (001) substrate and the EuS [140]. The EuS films were capped *in situ* with 6 nm of evaporated CaF_2 to prevent oxidation. We refer to the samples grown on Pyrex and InAs as Pyrex_X or InAs_X, respectively, where X denotes the EuS thickness in nm.

The magnetic properties of the EuS films have been studied with the ferromagnetic resonance option of a Quantum Design Physical Property Measurement System (PPMS); see Sec. 3.2.3 for details. To excite FMR in the sample, we used a CPW and a vector network analyser (VNA), model PNA N5225A from Agilent Technologies, configured in the transmission mode S_{21}. The external magnetic field H_{DC} was swept

from 0 to 0.5 T, while the excitation frequency was kept constant. At each temperature, ranging from 2 K to 30 K, the FMR response was measured at several fixed microwave frequencies within the 7-25 GHz range.

The amplitude of each spectrum was fitted to a Lorentzian curve after applying a phase correction to the signal and subtracting the background [216]. From this fit at a given frequency, the resonance field H_{res} allows the extraction of the effective magnetization M_{eff} according to the Kittel formula [Eq. (2.34)]. The linewidth ΔH provides the means to determine α_G interpreted within a model combining inhomogeneous broadening and Gilbert damping [Eq. (2.35)].

5.3 Results and discussion

When the magnetization $\boldsymbol{M}$ of a material is perturbed from its equilibrium, the magnetization precesses and, after some time, it relaxes and realigns to its equilibrium position [82]. The dynamics of the magnetization of ferromagnetic materials can be described by the Landau-Lifshitz-Gilbert (LLG) equation of motion, Eq. (2.32), which describes how the effective magnetic field $\boldsymbol{H}_{eff}$ interacts with $\boldsymbol{M}$, exerting a torque $\boldsymbol{\Gamma} = \boldsymbol{M} \times \boldsymbol{H}_{eff}$ that results in precession of $\boldsymbol{M}$ around the effective field direction if they are initially non-collinear (see pink trajectory in Figure 2.12a). Besides, it includes a term that accounts for the damping that cause the magnetization to diminish (see how the magnetization spirals inwards along the green trajectory in Figure 2.12b). The dissipative mechanisms that pull the magnetization in the direction of the magnetic field are reflected in the second term of Eq. (2.32) where α_G indicates the strength of the damping [82,217]. The spin-orbit coupling, non-local spin relaxation channels, and disorder present in a material are the major factors causing damping [80].

FMR experiments were performed using the VNA setup in combination with a CPW operating in a broad frequency range. A schematic of the setup is illustrated in Figure 3.8a. The sample is placed with the ferromagnetic part (EuS) facing the CPW, which is placed inside de PPMS magnet. The CPW is connected on both ends to ports 1 and 2 of the VNA that functions as a source of a microwave signal to excite the

magnetization dynamics in the sample and as a signal receiver, respectively [218,219].

A microwave current in the signal line of the CPW produces a microwave magnetic field H_{RF} (see Figure 5.1a). In the resonance condition determined by the external magnetic field (H_{DC}) and frequency, H_{RF} can resonantly excite the magnetic moments in the sample to precess around the direction of the local field [218], as illustrated in Figure 3.8a. A typical experimental resonance spectrum of 40-nm-thick samples grown on Pyrex and InAs at a resonance frequency of 18 GHz are shown in Figure 5.1b as a function of the in-plane H_{DC}. Resonance absorption of microwave power by the sample is seen as a dip in the measured spectrum. The experimental data is then fit using a Lorentzian curve to extract the resonance field H_{res} and linewidth ΔH.

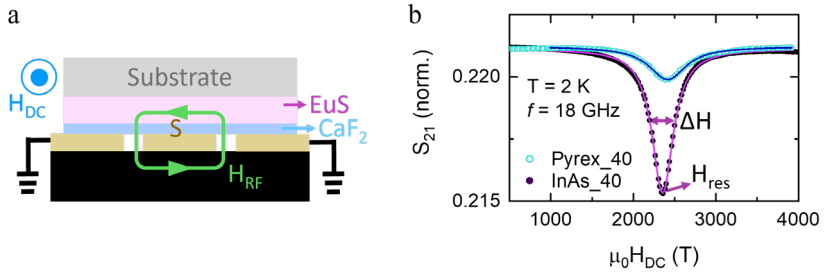

Figure 5.1. a) Schematic diagram of the side view of the CPW with the sample on top showing the magnetic field lines in green winding around the signal conductor (S). b) Representative experimental resonance spectrum of Pyrex_40 and InAs_40 samples with fit to a Lorentzian curve to extract the resonance field (H_{res}) and linewidth (ΔH).

We consider our sample as an infinitely extended thin film magnetized in its plane, for which the uniform excitation field gives a small precession cone-angle [81,82,219]. Then, the solution to the LLG equation (2.32) is a special case of the Kittel formula, with the resonance frequency f determined by Eq. (2.34) [220].

For excitation frequencies between 7 and 25 GHz, we observe a resonance dip which we fit using a Lorentzian curve (see Figure 5.1b). The intensity and linewidth of the resonance serve as indicators of the structural quality of the samples. As shown in Figure 5.1b, the InAs_40

sample presents a narrower and more intense dip than the Pyrex_40 one, as expected for the higher crystal quality of the epitaxial thin film.

We now focus on H_{res}, which allows us to extract information about the effective magnetization M_{eff}. Figure 5.2a and Figure 5.2b illustrate the evolution of the frequency as a function of the extracted H_{res} for different samples at a fixed temperature of 2 and 10 K, respectively. With increasing frequency or temperature (see Figure 5.2c for the InAs_40 sample), resonance fields shift to higher values. We apply Kittel's resonance condition, Eq. (2.34), to fit the experimental data (see lines in Figure 5.2a-5.2c) and extract M_{eff}, which is plotted in Figure 5.2d. All studied samples fit well with the Kittel formula, Eq. (2.34), as shown in Figure 5.2a for the case of T = 2 K, and in Figure 5.2b for T = 10 K. As shown in Figure 5.2d, M_{eff} becomes nearly thickness-independent for thicker films, tending toward a maximum value of approximately 1.5 T. The M_{eff} values at 2 K range from 1.37 T (1157 kA/m) in Pyrex_20, to 1.52 T (1282 kA/m) for in InAs_40, see inset of Figure 5.2d. These values are in good agreement with previously reported data for crystal EuS [221] and thin films [222], as the nominal M_{eff} expected in perfectly stoichiometric samples corresponds to 1.6 T. The temperature dependence of M_{eff} is consistent with the ferromagnetic behaviour of the EuS in all samples, decreasing as the temperature approaches T_C.

Moreover, we observe that T_C clearly depends on the film thickness, as M_{eff} decreases more rapidly with temperature in thinner samples. Lower T_C values for thinner EuS films have already been reported and have been attributed to stress mismatch in thermal expansion coefficients between the substrate and the EuS film [140,223,224]. This effect could also account for the differences observed between the InAs and Pyrex samples.

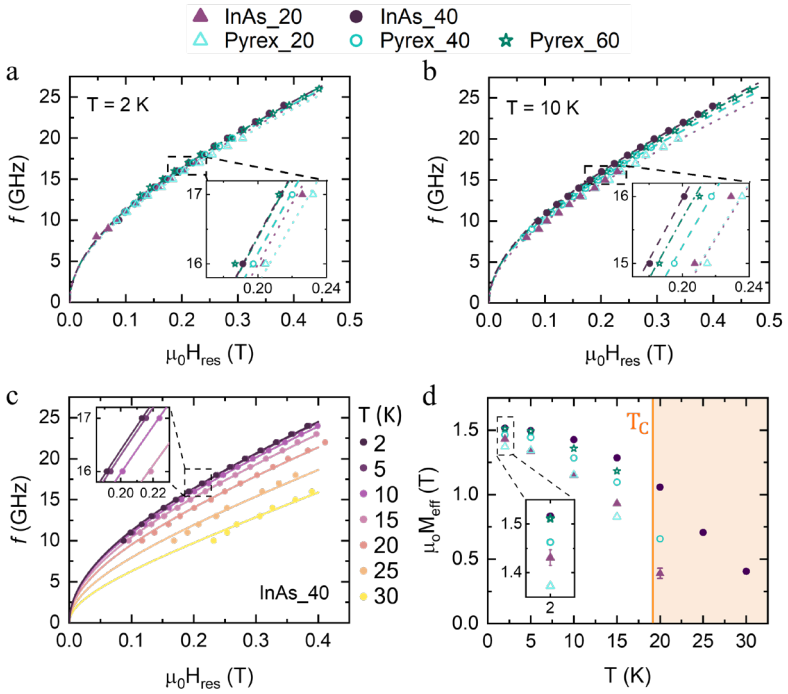

Figure 5.2. Frequency as a function of the resonant field at a) $T = 2$ K and b) $T = 10$ K for the different EuS films. Dotted, dashed, dot-dashed lines correspond to fits to Eq. (2.34) for 20-nm-, 40-nm-, 60-nm-thick films, respectively. c) Frequency as a function of the resonance field at different temperatures for the 40-nm-thick EuS film grown on InAs. Solid lines correspond to fits to Eq. (2.34) d) Temperature dependence of the effective magnetization extracted from the fits for the different EuS films (symbols follow the legend at the top).

The broadening of the FMR peak linewidth ΔH is a direct measure of the magnetic damping of the system and can be described by a linear dependence on frequency, allowing intrinsic and extrinsic contributions to be separated, see Eq. (2.35) [81,225,226]. In Eq. (2.35), the frequency-independent inhomogeneous linewidth broadening ΔH_0, arises from the presence of magnetic inhomogeneities [227]. In contrast, the total Gilbert damping α_G is frequency-dependent and consists of both intrinsic and extrinsic contributions (see Sec. 2.1.8). The latter typically arise from eddy currents, radiative damping, two-magnon scattering, and interfacial contributions. Both intrinsic and extrinsic contributions are thickness-dependent [87].

Figure 5.3a and 5.3b show the dependence of ΔH on frequency at 2 K and 10 K, respectively. ΔH_0 corresponds to the intercept of the linear fit of Eq. (2.35) to the vertical axis. We found ΔH_0 to be approximately 25-35 mT for InAs and 20-50 mT for Pyrex, with no observable temperature dependence up to 15 K (see Figure 5.3d). It is worth noting that lower frequencies allow for a more accurate determination of ΔH_0; however, the intensity and linewidth of the FMR signal typically prevent measurements below 10 GHz. The 20-nm-thick and 40-nm-thick Eu films in InAs substrates exhibit a significantly narrower ΔH_0 spread compared to the samples of the same thickness in Pyrex substrates, indicating reduced inhomogeneous broadening. This likely reflects fewer magnetic inhomogeneities, which can be attributed to the higher crystal quality expected from epitaxial growth. Moreover, the narrowest ΔH is observed for samples which have the best structural quality. Figure 5.3a and 5.3b show lower values for epitaxial InAs_40.

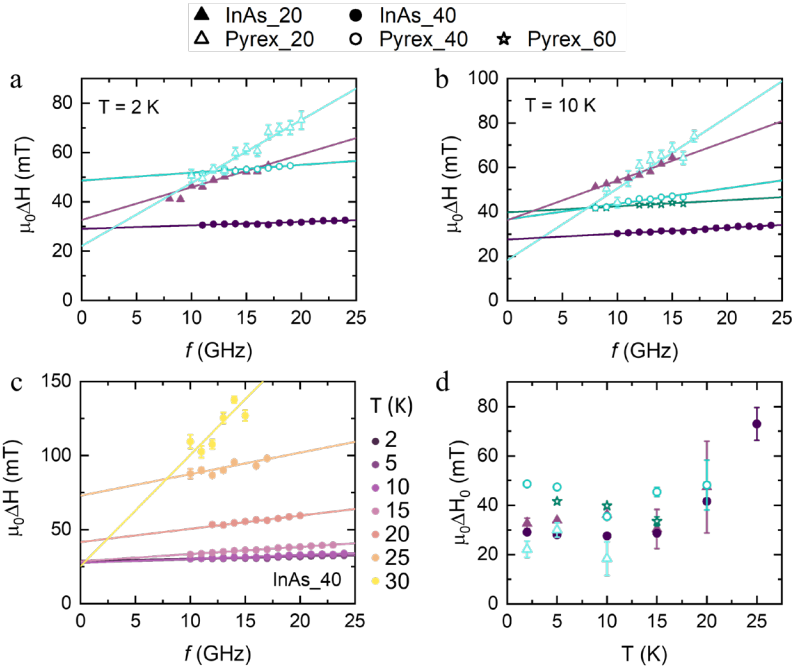

Figure 5.3. FMR linewidth as a function of frequency: a) at $T = 2$ K and b) at $T = 10$ K, for the different EuS films, and c) as a function of temperature up to 30 for InAs_40. Solid lines correspond to the fit of experimental data to Eq. (2.35). d) Temperature dependence of the inhomogeneous broadening.

From Eq. (2.35), α_G is extracted from the slope of the linewidth versus resonance frequency (see linear fit in Figure 5.3a-5.3c). α_G is analysed in both InAs- and Pyrex-based samples for temperatures up to 30 K. Note that the slope of the fitted lines in Figure 5.3c is temperature dependent. The temperature evolution of α_G shows an increase with temperature, independent of the substrate or film thickness (Figure 5.4a). Since α_G describes the viscous relaxation of the magnetization, including mechanisms such as direct energy dissipation into the lattice phonon bath or nonuniform magnetization dynamics (e.g. spin waves) [81,228], they are expected to be influenced by temperature. The variation of α_G with temperature has already been reported in other magnetic materials [200,204,215,229,230]. In the present case, considering that the studied temperature range extends from 2 K up to T_C of EuS, it covers the full range from the highest values of M_{eff} to the point where it nearly vanishes.

The total Gilbert damping α_G considered above includes extrinsic contributions. First, eddy current damping is not present in our samples since they are insulating. However, radiative damping α_{rad} arises because of the inductive coupling between sample and waveguide, and thus it depends on the properties and dimensions on both waveguide and sample. The radiative damping is well approximated by Eq. (2.37), where l = 5 mm, $w_{cc} = 176$ μm and $Z_0 = 50$ Ω. For very thin films or films with low saturation magnetization α_{rad} is not a significant contribution to the total Gilbert damping and can be ignored [231]. As shown in the shadowed area of Figure 5.4a, α_{rad} increases as the temperature is lowered, reflecting the corresponding increase of M_{eff}. In all samples, the estimated α_{rad} saturates at about 10^{-3} as the temperature is lowered, thus its contribution to the total damping is appreciable in the samples with the lowest α_G. In the following, we refer to α_G^* as the total Gilbert damping with the radiative damping contribution subtracted, that is $\alpha_G^* = \alpha_G - \alpha_{rad}$.

Two-magnon scattering can also contribute to the total Gilbert damping observed, as the film magnetization is oriented in-plane. Tipically, sizeable TMS results in a non-linear behaviour of the linewidth versus frequency curves which is not observed in the measured frequency range. To evaluate the impact of this contribution, we performed additional FMR measurements for films magnetized out-of-plane. In

the 40 nm Pyrex sample, we found similar damping values for both in-plane and out-of-plane configurations, indicating that two-magnon scattering does not play a role in the in-plane measurements (see Sec. 5.5.1 for more details).

Regarding the substrate, lower damping values are found on InAs (see Figure 5.4b); at 2 K and 20-nm-thick EuS, $\alpha_G^* = (3.5 \pm 0.3) \times 10^{-2}$ for Pyrex and $(1.8 \pm 0.2) \times 10^{-2}$ for InAs. From here, we conclude that epitaxially grown films reduce the Gilbert damping. However, we find that the thickness of EuS has a stronger impact on α_G^* when doubling the thickness. As highlighted in Figure 5.4, α_G^* decreases one order of magnitude when the sample thickness increases from 20 nm to 40 nm, indicating that the ratio surface/interface is the dominant factor. At 2 K and 40-nm-thick EuS, α_G^{int} reduces to $(4 \pm 1) \times 10^{-3}$ for Pyrex and $(1.0 \pm 0.2) \times 10^{-3}$ for InAs, which is in the same order of magnitude as nanometer-thick YIG films at 2 K [199,232]. Moreover, Pyrex_60 yields $\alpha_G^* \approx 3 \times 10^{-3}$ at T = 5 K, within the same order of magnitude. The values α_G^* that we obtained are comparable to the reported ones for permalloy films in the 20-50 nm range at 5 K [204] or in the 20-120 nm range at cryogenic temperatures [198]. Overall, our measurements suggests that films of EuS with thicknesses between 40 nm and 60 nm can reach α_G^* within the 10^{-3} range, even for polycrystalline morphology. The thickness dependence indicates that the surface/interface ratio play an important contribution to α_G^*, and stoichiometric defects could be denser at the film boundaries.

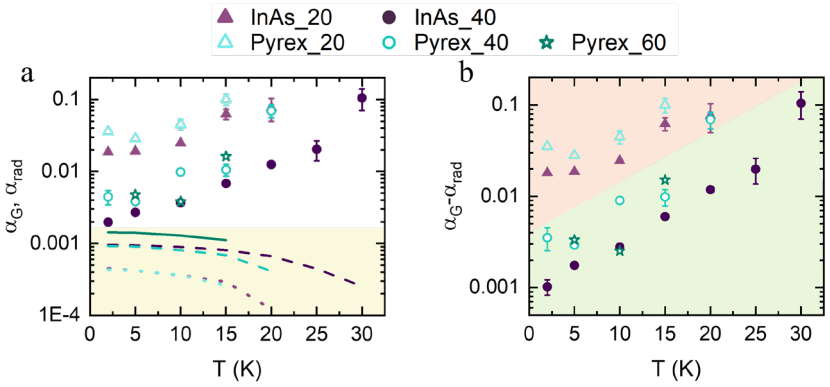

Figure 5.4. a) Total Gilbert damping (blue and maroon symbols) and radiative damping (green and purple lines in the shadowed area) as a function of temperature for the different EuS films. b) Damping, with the radiative

damping subtracted from the total Gilbert damping, as a function of temperature for the different EuS films. Symbols follow the legend on top of the figure.

Finally, we discuss the results considering the structural differences of the studied films. In the case of EuS/InAs samples, González-Orellana [140] reported a disordered interface of 5 nm in another InAs_40 sample, grown with the same deposition method and conditions, which is around 12.5% of the total EuS layer. This interfacial layer will affect the properties of the EuS films and become more important when thickness is decreased, not only reducing M_{eff} and T_C but also increasing α_G^* of the epitaxially grown samples. Indeed, a faster decay of the effective magnetization with increasing temperature is observed for thinner EuS films on both types of substrates, as shown in Figure 5.2d, confirming the presence of the interfacial layer also in the polycrystalline EuS films. Moreover, the interfacial layer will affect also α_G^*, increasing the damping of the thinner samples, as presented in Figure 5.4b. At the temperature range between 2 and 20 K, the damping measured in 40-nm-thick EuS is approximately one order of magnitude smaller than for 20-nm-thick EuS. In addition to this, single crystal materials exhibit enhanced magnetic behaviour with respect to polycrystals, which leads to slightly higher values of magnetization and T_C (Figure 5.2d), as well as smaller α_G^* values (Figure 5.4b), on the epitaxially grown EuS/InAs samples with respect to the polycrystalline EuS/Pyrex ones.

5.4 Conclusions

To summarize, we performed FMR measurements on EuS thin films grown on different substrates, exhibiting different structural properties. The experimental results show that the Gilbert damping decreases by one order of magnitude as the thickness is doubled from 20 nm to 40 nm, whereas crystallinity of the samples seems to have a lower impact on the magnetic losses. We associate this thickness dependence with the presence of structural and chemical defects at the substrate/film interface. Notably, such a result suggests that achieving atomically clean EuS interfaces may result in even lower damping in such films. Our study demonstrates that both epitaxial and polycrystalline EuS films exhibit Gilbert damping parameters of the order of 10^{-3} for temperature below 10 K, comparable to the case of thin permalloy

films. Moreover, we observe a decrease of the damping as the temperature is decreased. We note here that even the best magnonic materials, such as YIG, suffer from the magnetic losses of the substrate as the temperature is lowered [200,229]. As our EuS films demonstrate good damping characteristics even without the need of epitaxial growth, we suggest that their damping in the low temperature regime could be further engineered by optimizing the choice of the substrate material. Our study paves the way to exploit the magnetization dynamics of EuS films in low temperature spintronic applications, as an alternative to garnets and permalloy films.

5.5 Appendices

5.5.1 Out of plane measurements

In order to analyze the contribution from two-magnon scattering we performed out of plane measurements in Pyrex_40. As shown in Figure 5.5 we got the same linear slope, which means similar damping values, from the in-plane and out-of-plane measurements, indicating TMS does not play a critical role in the in-plane measurements of the absence of two-magnon scattering.

Out-of-plane field FMR measurements of EuS films on InAs substrates was characterized by a very strong, field-dependent background signal, most probably associated with weakly paramagnetic character of the InAs.

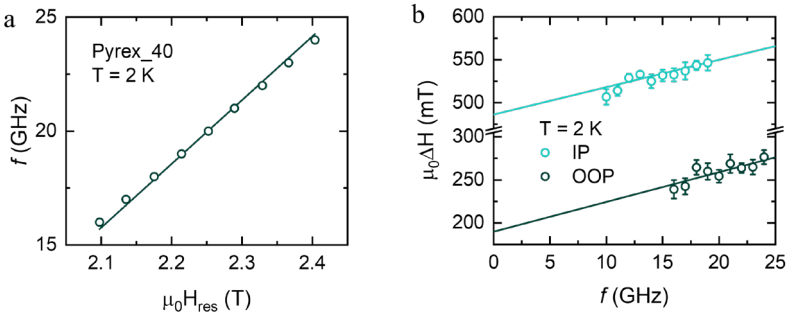

Figure 5.5. a) Frequency as a function of the resonant field at T = 2 K for the out-of-plane configuration. b) FMR linewidth as a function of frequency for the in plane (IP) and out-of plane (OOP) configuration at 2 K, on Pyrex_40.

5.5.2 Magnetic characterization of EuS without capping layer

A similar analysis to the one shown in this chapter was carried out for EuS/Pyrex films without capping layer. In this case, we analyzed the same sample used for the study of the MST devices (Chapter 4), which consist of 18 nm of EuS. FMR measurements were performed at constant temperature by sweeping an external magnetic field at several fixed microwave frequencies. Each FMR spectrum has been analyzed by subtracting a background and fitting it to a Lorentzian curve (see Figure 5.6a). The resonance field (H_{res}) as a function of microwave frequency is shown in Figure 5.6b, which is fitted using Eq. (2.34) (solid lines in Figure 5.6b) [81,233]. Due to a small magnetic anisotropy of the EuS, we can assume that the saturation of magnetization $M_{sat} = M_{eff}$. As depicted in Figure 5.6c, the temperature behavior of M_{eff} shows the same trend as the magnetic moment (see Figure 4.12a), disappearing around T_C. At T = 2 K, we found a saturation magnetization of 1163 kA/m, which is close to the reported bulk value of 1240 kA/m [221]. From Eq. (2.35), we fit the linear dependence of ΔH with f (solid lines in Figure 5.6d), and extract $\alpha_G = (4.0 \pm 0.4) \times 10^{-2}$ at 2 K, which is at least one order of magnitude higher than that of YIG [201], and similar to the one obtained for the 20-nm-thick sample in Pyrex with a capping layer, $\alpha_G = (3.6 \pm 0.3) \times 10^{-2}$. The temperature dependence up to 20 K is plotted in Figure 5.6e.

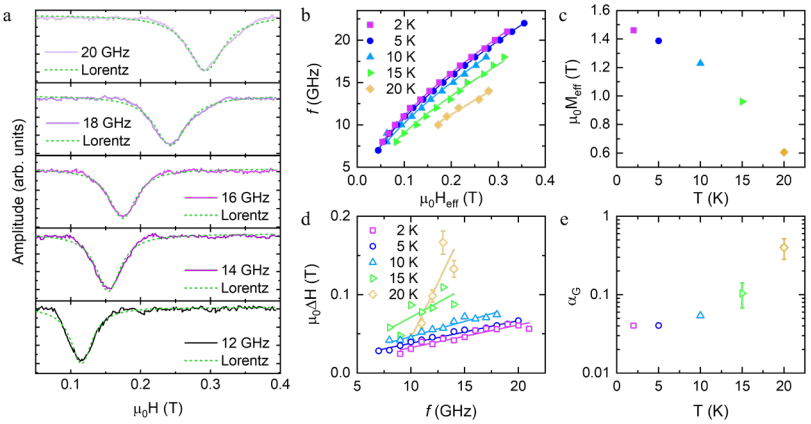

Figure 5.6. a) FMR spectra as a function of external magnetic field at 2 K for different frequencies. Dashed lines represent the fittings to a Lorentzian curve. b) Frequency as a function of the resonant field at different temperatures. Solid lines correspond to the fit of experimental data to the Kittel formula, Eq. (2.34). c) Effective saturation magnetization extracted from the fitting in panel b). d) FMR linewidth (ΔH) as a function of frequency. Solid lines correspond to linear fits of the experimental data based on Eq. (2.35). e) Gilbert damping of the EuS sample as a function of temperature, extracted from the slope of panel d).

Chapter 6
Orbital Hall conductivity and orbital diffusion length of Vanadium thin films by Hanle magnetoresistance

In spintronics, the spin Hall effect has been widely used to generate and detect spin currents in materials with strong spin-orbit coupling such as Pt and Ta. Recently, its orbital counterpart has drawn attention as a new tool to generate and detect orbital currents and thus investigate orbital transport parameters. In this chapter, we investigate vanadium (V), a *3d* transition metal with weak spin-orbit coupling but with a theoretically large orbital Hall conductivity. We measure a large Hanle magnetoresistance in V thin films with a magnitude comparable to that of heavy metals and at least one order of magnitude higher than the spin Hall magnetoresistance observed in a $Y_3Fe_5O_{12}$/V bilayer, pointing to the orbital Hall origin of the effect. A fit of the magnetic-field dependence and thickness dependence of the Hanle magnetoresistance to the standard diffusion model allows us to quantify the orbital diffusion length (~2 nm) and the orbital Hall conductivity [~78 ($\hbar$/2e) $\Omega^{-1}cm^{-1}$] of V.

6.1 Introduction

The SHE and ISHE are widely used in spintronics to generate and detect spin currents without the use of a ferromagnetic material as the spin source (see Sec. 2.1.2) [234,235]. Indeed, they are of utmost importance in novel applications such as the SHE to write magnetic elements in MRAMs via SOTs [236–238] or the ISHE to readout magnetic elements in magnetoelectric spin-orbit (MESO) logic [11,238,239]. Since SHE depends on the strength of the SOC, which scales with the atomic number (Z) as Z^4 (see Chapter 1) [240,241], SHE studies have mainly focused on heavy metals (HMs), essentially *4d* and *5d* transition

metals [240,242–244]. Theoretical studies also proposed the existence of the OHE [108–112], the orbital analogue of the SHE. As detailed in Sec. 2.2.2, the OHE was firstly calculated in the well-known HMs [108,109] and, more recently, it has been extended to light metals (LMs) such as the *3d* transition metals [110–112], which show weak SOC. According to these theoretical calculations, *3d* transition metals present higher intrinsic orbital ($\sigma_{OH}^{int} \sim 10^3$–$10^4$ ($\hbar$/e) Ω^{-1}cm^{-1}) than spin ($\sigma_{SH}^{int} \sim 10^2$ ($\hbar$/e) Ω^{-1}cm^{-1}) Hall conductivities [111,112]; because of that, LMs have been considered ideal candidates to explore orbital physics. Experimental studies have quantified the orbital transport parameters of *3d* transition metals as summarized in Table 2.1.

HMR arises because of the combination of the SHE and ISHE together with the presence of an external magnetic field H producing a change in the resistivity and giving rise to the magnetoresistance effect [61], as discussed in detail in Sec. 2.1.5. Because of the SHE requirement, it was originally explored on HMs [62,63,245,246]. Since the orbital angular momentum also precesses with H, HMR should also occur in the presence of OHE (see Sec. 2.2.5). Due to the important contribution of the OHE in LMs, it has been recently observed in Mn [102].

In contrast, SMR [56,59,178] arises when a HM is put in contact with a FM, as explained in Sec. 2.1.4. The spin current with spin polarization s, originated because of the SHE, interacts with the magnetization M of the FM at the HM/FM interface, which can be reflected (when $\boldsymbol{M} \parallel \hat{\boldsymbol{s}}$) or absorbed via spin transfer torque (when $\boldsymbol{M} \perp \hat{\boldsymbol{s}}$). Although there is an orbital analogue of the SMR, the orbital Hall magnetoresistance [137] which arises due to the interaction of orbital currents with M of the FM at a LM/FM interface via the orbital torque [138], see Sec. 2.2.4, it requires the FM to have a considerable orbital magnetization component [247].

In this chapter, we report a HMR of the order of 10^{-4} on sputtered V thin films. A patterned Hall bar allows to perform longitudinal and transverse magnetotransport measurements by rotating the sample along different axis and sweeping the magnetic field up to 9 T. We observe the symmetry expected for HMR in the temperature range from 25 K to 300 K in samples of different thicknesses ranging from 4 nm to 30 nm and different resistivities. From the analysis of the SMR and spin-mixing conductance of $Y_3Fe_5O_{12}$/V samples, we confirm the

orbital Hall origin of the observed HMR and quantify the orbital transport parameters of V.

6.2 Methods

V samples were prepared by patterning a Hall bar, as explained in Sec. 3.1, with a length of l = 200 μm and a width of w = 50 μm on top of Si/SiO_2(150 nm) or $Y_3Fe_5O_{12}$ (yttrium iron garnet, YIG) grown on gadolinium gallium garnet (GGG). The samples were prepared by photolithography process (see Sec. 3.1.2.2) and magnetron-sputtering deposition of V (50 W dc; 3 mTorr of Ar) (Sec. 3.1.3.1), followed by a capping layer of either 5 nm of SiO_2 (200 W rf; 3 mTorr of Ar) or 8 nm of SiN (100 W rf; 3 mTorr of Ar) to prevent oxidation.

Magnetotransport measurements were taken with a PPMS covering the temperature range 25 K ≤ T ≤ 300 K (see Sec. 3.2.2). We performed ADMR and FDMR measurements by applying magnetic fields H up to $\mu_0 H$ = 9 T. For the ADMR, the magnetic field H is rotated along 3 different planes: *xy*-plane, where H is rotated by an angle α from the direction of the applied current (x), *yz*-plane, where H is rotated by an angle β from the out-of-plane direction (z), and *xz*-plane, where H is rotated by an angle γ from the out-of-plane direction (z) (see Figure 6.1a and Figure 3.7). For the FDMR, H is applied along the three main axes (x, y and z). As sketched in Figure 6.1a, a 10 μA dc electric current is applied along the Hall bar with a Keithley 6221 current source meter, and the voltage is measured with a Keithley 2182 nanovoltmeter in the longitudinal V_L or transverse V_T configuration using a dc-reversal mode (see Sec. 3.2.2).

The magnetic properties of the samples have been studied with the FMR option of the PPMS (see Sec. 3.2.3), covering the temperature range 100 K ≤ T ≤ 290 K. FMR measurements were performed at constant temperature and fixed microwave frequency (in the range of 10-19 GHz) while sweeping the magnetic field.

6.3 Results and discussion

According to the spin (and orbit) diffusion theory, the resistivity of the NM layer in the longitudinal (ρ_L) and transverse (ρ_T) configurations changes either with the orientation of an applied H in the case of HMR (see Sec. 2.1.5 and Sec. 2.2.5) or with the orientation of the magnetization of an adjacent FM in the case of SMR (see Sec. 2.1.4).

This results in a characteristic dependence of ρ_L and ρ_T of the film, which follows Eqs. (2.19) and (2.20) for SMR, and Eqs. (2.23) and (2.24) for the HMR.

ADMR and FDMR measurements are taken in the system Si/SiO_2/V(t_V nm)/SiO_2(5 nm) or Si/SiO_2/V(t_V nm)/SiN(8 nm), where t_V denotes the thickness, for samples with a resistivity of $\rho_{L0}\sim$ 270 μΩ·cm. Although both capping and substrate materials act as diffusion barriers, the presence of an interfacial vanadium oxide layer cannot be fully excluded. Such a layer could slightly reduce the effective conducting thickness, but it is not expected to influence the overall results.

Figure 6.1 shows the measurement configuration (Figure 6.1a) and representative results of the ADMR (Figure 6.1b), longitudinal FDMR (Figure 6.1c) and transverse FDMR (Figure 6.1d) measurements taken in a 6-nm-thick film at T = 100 K. Both ADMR and FDMR show the shape and symmetry expected by HMR between 25 K and 300 K (see the temperature dependence of the ADMR in the Sec. 6.5.2). The result of the ADMR is plotted as $\Delta\rho_L/\rho_{L0} = \Delta R_L/R_L = [R_L(\alpha,\beta) - R_L(90°)]/R_L(90°)$, where $R_L = V_L/I$ is the longitudinal resistance (see Figure 6.1a). We observe the typical $\cos^2(\alpha,\beta)$ modulation related to the HMR geometry [62], which gives an amplitude of the order of 10^{-4} in both α and β planes (Figure 6.1b). Similar values have been found in Pt [62,63,245]. A small difference of the order of 10^{-5} is present between the amplitude of α and β plane, corresponding to a $\sin^2\gamma$ modulation in γ plane which cannot be due to HMR, for which the modulation should vanish (see also Sec. 6.5.2). The origin of such extra magnetoresistance, which is negative when H is applied along z (see the difference between longitudinal FDMR along x and along z in Figure 6.1c), is most likely related to the weak localization which appears in disordered systems, which are also known by a resistivity increase below a characteristic crossover temperature [248,249], a feature present in all our samples (see Figure 6.6a).

The longitudinal FDMR (Figure 6.1c), plotted as $\Delta\rho_L/\rho_{L0} = \Delta R_L/R_L = [R_L(H_i) - R_L(H=0)]/R_L(H=0)$, with i=x,y,z, shows that the amplitude depends on the strength of the magnetic field with a parabolic increase at low fields ($\propto H_{x,z}^2$) that tends to flatten at high fields, with similar values along the x- and z-axes (except for the small variation due to weak localization mentioned above). In contrast, a small positive FDMR is found along the y-axis, which we ascribe to the in-plane weak localization contribution [250]. Figure 6.1d, plotted as $\rho_T/\rho_{L0} = R_T(H_z)l/(wR_L)$, where $R_T = V_T/I$ is the transverse

resistance, shows the normalized transverse resistivity where the contribution from the ordinary Hall effect is subtracted by performing a linear fit of the transverse FDMR as detailed in Sec. 6.5.3. We see a strong dependence on the magnetic field only when it is applied out of plane, with a linear increase with magnetic field ($\propto H_z$) at low fields and tending to saturation above ~3 T. Overall, the observed signatures of the measured ADMR, longitudinal FDMR and transverse FDMR confirm the presence of HMR in our V thin films.

Furthermore, we perform ADMR and FDMR measurements in a set of samples with same thickness but different resistivities. In the range of resistivities evaluated (ρ_{L0}~ 171–464 μΩ·cm), all of them showed the characteristic HMR signatures discussed above. Among them, we find that the amplitude of the HMR increases with resistivity, with values one order of magnitude higher for highly resistive samples with the same thickness (see Sec. 6.5.4 for more details).

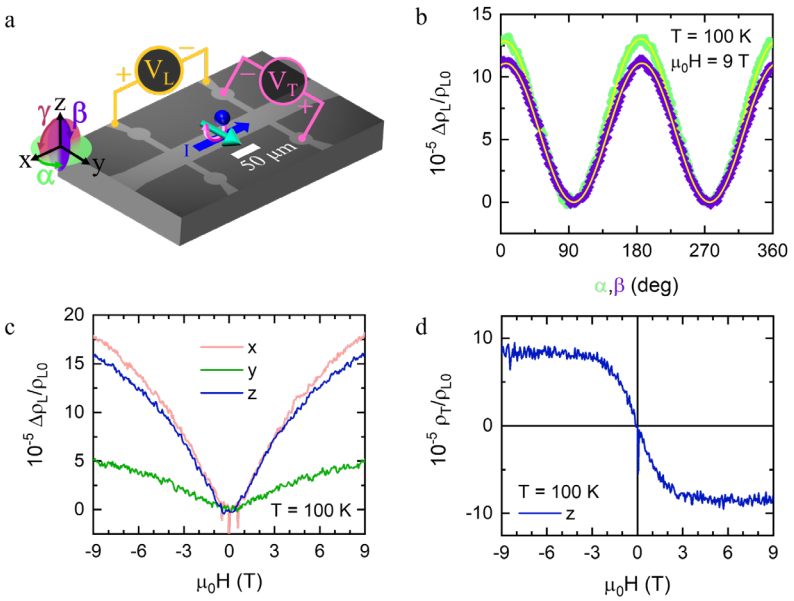

Figure 6.1. HMR measurements (a) Optical microscope image of a vanadium Hall bar showing the experimental setup for HMR and SMR measurements. A charge current I is applied along x-direction in the Hall bar and then the longitudinal V_L and transverse V_T voltages are measured as depicted in the image. The three H-rotation planes (α, β, γ) are illustrated. (b) ADMR measurement at T =100 K and $\mu_0 H$ = 9 T in α, β planes. Yellow lines correspond to a $cos^2(\alpha, \beta)$ fit. (c) Longitudinal and (d) transverse FDMR

measurements performed at 100 K with H applied along the three main axes. Data corresponds to sample Si/SiO_2/V(6 nm)/SiO_2(5 nm).

Although the HMR can originate from both the SHE and the OHE, we expect that, given the weak SOC in V, it arises mostly from the OHE and not from the SHE. Indeed, theoretical calculations for bcc V predict a large σ_{OH} from 4500 to 6050 ($\hbar$/e) Ω^{-1}cm^{-1} with a much smaller σ_{SH} from −13 to −90 ($\hbar$/e) Ω^{-1}cm^{-1} [111,112,251,252]. Importantly, HMR provides a way to quantify angular momentum transport parameters, which in HMs correspond to spin [62,63], whereas in LMs are mostly orbital [102]. In principle, orbital interfacial effects could also contribute to the HMR but disentangling them from the bulk would be very challenging. For that, we come back to Eqs. (2.23) and (2.24) and focus on $\Delta\rho_1^{HMR}$ and $\Delta\rho_2^{HMR}$, which we can express as a function of the orbital Hall angle θ_{OH} and the orbital diffusion length λ_{OD}, see Eqs. (2.39) and (2.40) [62,63].

To extract the 3 unknown parameters (θ_{OH}, λ_{OD}, and D_O), we can simultaneously fit the longitudinal FDMR to Eq. (2.39) and transverse FDMR to Eq. (2.40), but the use of 3 free fitting parameters with 2 data sets gives correlations between the free parameters. In order to obtain an extra data set, the HMR was measured in samples with different thickness in the range between 4 and 30 nm on Si/SiO_2 substrates (see results in Figure 6.2a and Figure 6.2c for 100 K and 290 K, respectively). For that, we chose a set of samples where ρ_{L0} does not change significantly with thickness (see Figure 6.5a). By using Eq. (2.39), we were able to fit the thickness dependence of the HMR amplitude, obtained from the longitudinal ADMR measurement in α-plane (such as the one shown in Figure 6.1b), at a fixed magnetic field. In this fit, λ_{OD} is uncoupled from the other two parameters, since it is essentially constrained by the position of the observed maximum but not by the amplitude. By fixing the obtained value of λ_{OD}^V, we perform again the simultaneous fit of the longitudinal and transverse FDMR in a 6-nm-thick film (see Figure 6.2b and Figure 6.2d). For that, we subtract the contribution from the weak localization in the longitudinal FDMR by doing $\Delta\rho_{L'}/\rho_{L0} = \Delta\rho_L^x/\rho_{L0} - \Delta\rho_L^y/\rho_{L0}$. This allows us to reliably extract the other two free parameters, θ_{OH} and D_O. Additionally, the orbital relaxation time $\tau_{OD} = \lambda_{OD}^2/D_O$ and the total orbital Hall conductivity $\sigma_{OH} = \theta_{OH}/\rho_{L0}$ can also be derived. The orbital transport parameters of V extracted from the fittings are listed in Table 6.1 for two specific temperatures, with similar values at 100 K and 290 K (λ_{OD}^V~2 nm and θ_{OH}^V~0.020).

Moreover, we also analyze the impact of resistivity on the orbital transport parameters of the V thin films. To do so, we perform a simultaneous triple-variable fit of the thickness-dependent ADMR signal of high-resistivity samples and the longitudinal and transverse FDMR datasets of a 6-nm-thick V sample with a resistivity of $\rho_{L0}\sim 378$ μΩ·cm, at 290 K (for more details, see Sec. 6.5.5). While most of the transport parameters remain unchanged within the error (see Table 6.1), θ_{OH} and σ_{OH} are affected by the change of resistivity. θ_{OH} increases by ~14% with respect to the previous set of samples with $\rho_{L0}\sim 270$ μΩ·cm, while σ_{OH} decreases by ~19%, an interesting result that is discussed below.

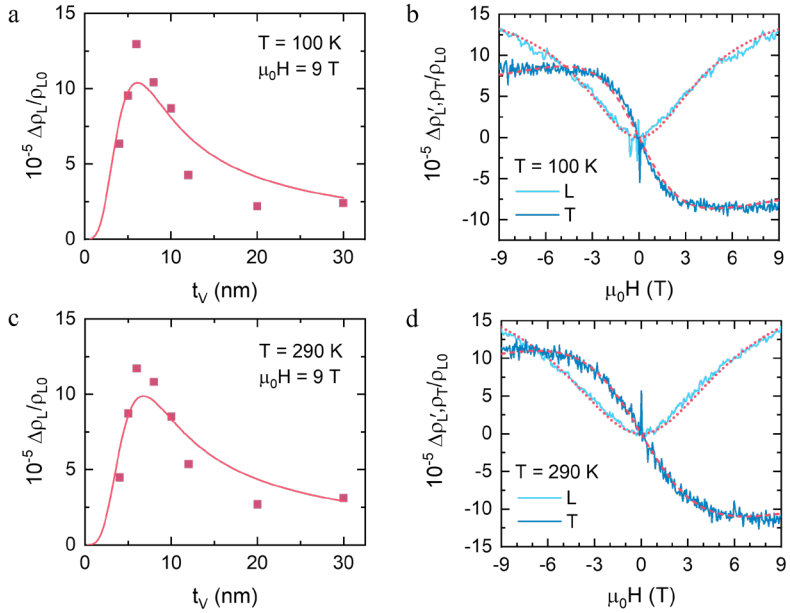

Figure 6.2. HMR thickness and magnetic field dependence in V thin films with fittings to the HMR equations. (a) and (c) Longitudinal HMR amplitude at 9 T extracted from the ADMR measurements in α plane (pink solid squares) as a function of V-film thickness at 100 K and 290 K, respectively, with their corresponding fittings of Eq. (2.39) (red solid lines). (b) and (d) Longitudinal (L) (light blue line) and transverse (T) (dark blue line) FDMR for sample Si/SiO_2/V(6 nm)/SiO_2(5 nm) at 100 K and 290 K, respectively, with their corresponding fittings of Eq. (2.39) (dotted lines) and Eq. (2.40) (dashed lines).

Table 6.1. Orbital transport parameters of V extracted from the fittings at 100 K and 290 K.

T (K)	ρ_{L0} (μΩ·cm)	λ_{OD}^{V} (nm)	θ_{OH}^{V}	D_O^V (mm^2/s)	τ_O^V (ps)	σ_{OH}^{V} [($\hbar$/2e) Ω^{-1}cm^{-1}]
100	264.4	1.8 ± 0.3	0.020 ± 0.001	1.3 ± 0.4	2.5 ± 0.2	76 ± 4
290	270.3	2.1 ± 0.3	0.021 ± 0.001	2.2 ± 0.6	2.0 ± 0.2	78 ± 4
290	378.1	2.1 ± 0.3	0.024 ± 0.001	2.0 ± 0.6	2.2 ± 0.2	63 ± 3

In order to know whether there is any contribution from the SHE in the HMR, we can perform SMR measurements using YIG as an adjacent ferrimagnetic insulator. Since the SMR is modulated by the magnetization of YIG, which can only interact with spin (but not orbital) currents [247], its amplitude will depend on the SHE only. The measurements performed in YIG/V(7 nm)/SiO_2(5 nm) at 100 K are represented in Figure 6.3, where we plot in-plane transverse measurements [equivalent to the longitudinal ones, compare second term in Eq. (2.23) with first term in Eq. (2.24)] because they give a larger signal-to-noise ratio in the otherwise small signal. Figure 6.3a shows the normalized transverse FDMR plotted as $\rho_T/\rho_{L0} = [R_T(H) - R_T(90°)]l/[wR_L(90°)]$, with the magnetic field applied in plane at α = 45º and α = 135º, where the occurrence of the magnetization reversal of YIG is clearly detected around 0.3 mT. The gap between the two curves accounts for the magnitude of the SMR, which is of the order of 10^{-6}, two orders of magnitude lower that in the HMR case. The same amplitude appears in the normalized transverse ADMR measurements, $\Delta\rho_T/\rho_{L0} = [R_T(\alpha) - R_T(90°)]l/[wR_L(90°)]$, at low magnetic fields (20 mT) where a sin α·cos α modulation is present as shown in Fig. 6.3b and expected from the SMR theory [see Eq. (2.20)]. At high magnetic fields, where the HMR may appear, we see again the sin α·cos α modulation but with an amplitude more than one order of magnitude higher, although reduced as compared with Si/SiO_2/V samples of similar thickness (see Figure 6.2a and Sec. 6.5.6 for more details). The presence of a clear SMR signal confirms that we have spin currents generated by SHE, but it is more than one order of magnitude lower than in YIG/Pt [62,253], in which the SMR amplitude and the HMR amplitude at 9 T have been reported to be of the same order.

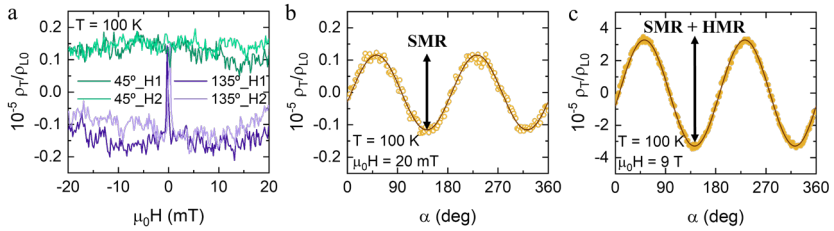

Figure 6.3. Magnetoresistance measurements using YIG. (a) Normalized transverse FDMR measurements performed at 45º and 135º in a-plane in a low magnetic field range. (b) Normalized transverse ADMR measurements at $\mu_0 H$ = 20 mT, where the brown line corresponds to a sin α·cos α fit. The arrow indicates the SMR amplitude $\Delta\rho_1^{SMR}/\rho_{L0}$. (c) Normalized transverse ADMR measurements at $\mu_0 H$ = 9 T. Brown line corresponds to a sin α·cos α fit. The arrow indicates the total amplitude, which contains the HMR ($\Delta\rho_1^{HMR}/\rho_{L0}$) and SMR contributions. Data corresponds to measurements performed at 100 K on sample YIG/V(7 nm)/SiO_2(5 nm).

Whereas the much smaller amplitude of SMR as compared to HMR in YIG/V seem to confirm that HMR is dominated by the OHE contribution, there is still the possibility that a strongly reduced spin-mixing conductance at the YIG/V interface explains the different HMR and SMR amplitudes solely with the presence of SHE. In order to rule out this possibility, we performed FMR on YIG/V samples. FMR allows to extract the real part of the interfacial spin-mixing conductance, $\tilde{g}_r^{\uparrow\downarrow}$, which determines the ability of the interface to transmit spins. Based on the Gilbert damping constants of the YIG single layer, α_{YIG}, and YIG/V bilayer, $\alpha_{YIG/V}$, we can obtain $\tilde{g}_r^{\uparrow\downarrow}$ from Eq. (2.38). By performing a Lorentzian fit of each FMR spectrum (see dotted lines in Fig. 6.4a), we determined M_S and α from the frequency dependencies of the resonant field H_{res} and linewidth ΔH, respectively.

The frequency dependence of H_{res} follows the Kittel formula, Eq. (2.34), and at T = 100 K we found an effective magnetization $\mu_0 M_{eff}$ = 0.2673 ± 0.0001 T, which we can consider that equals the saturation magnetization [95,254]. α can be obtained from the linear increase of ΔH with frequency, f, following Eq. (2.35). Figure 6.4b shows the linear increase of ΔH with frequency, for a YIG film and a YIG/V(20nm)/SiO_2(5nm) film, in the frequency range between 10 and 19 GHz. From the linear fit of the data, the damping obtained is α_{YIG} = (1.9 ± 0.1)×10^{-4} and $\alpha_{YIG/V}$ = (1.0 ± 0.1)×10^{-3} at T = 100 K. By using Eq. (2.38), we calculate $\tilde{g}_r^{\uparrow\downarrow}$ = (4.0 ± 0.3)×10^{19} m^{-2} at 100 K, one order

of magnitude larger than previously reported at 300 K in YIG/V using 20-nm-thick YIG films [255].

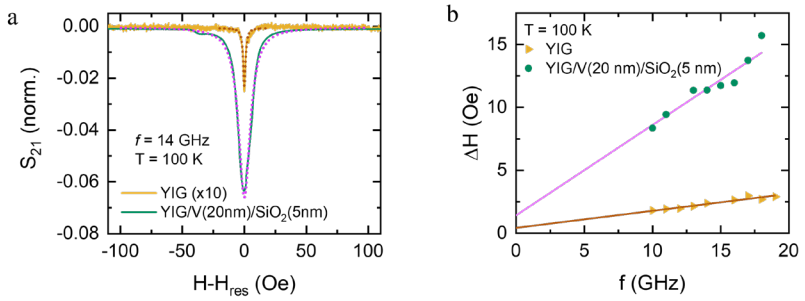

Figure 6.4. (a) Experimental FMR spectra of a YIG film and a YIG/V(20nm)/SiO_2(5nm) film, measured at T = 100 K and f = 14 GHz. Dotted lines represent the fittings to a Lorentzian curve. (b) Frequency dependencies of FMR linewidth of a YIG film and a YIG/V(20nm)/SiO_2(5nm) film, at T = 100 K. Solid lines correspond to a linear fit of the experimental data to Eq. (2.35).

With the extracted value of $\tilde{g}_r^{\uparrow\downarrow}$, and considering the transport parameters shown in Table 6.1 to be of spin origin, we calculate the expected amplitude of the SMR under this hypothesis. The amplitude $\Delta\rho_1^{SMR}$ can be expressed in terms of the spin transport parameters by using Eq. 2.21, which can be simplified as [256]:

$$\frac{\Delta\rho_1^{SMR}}{\rho_{L0}} \approx \theta_{SH}^2 \frac{\lambda_{SD}}{t_{LM}} \frac{2\lambda_{SD}\tilde{G}_r^{\uparrow\downarrow} tanh^2 \frac{t_{LM}}{2\lambda_{SD}}}{\frac{1}{\rho_{L0}} + 2\lambda_{SD}\tilde{G}_r^{\uparrow\downarrow} coth \frac{t_{LM}}{\lambda_{SD}}} \qquad (6.1)$$

By replacing the values of Table 6.1 (low resistivity samples at T = 100 K) in Eq. (6.1), we get $\Delta\rho_1^{SMR}/\rho_{L0} = 7.9\times10^{-5}$, which is two orders of magnitude larger than what we obtain experimentally (see Figure 6.3b). Since the transport parameters obtained from HMR cannot explain the observed amplitude of the SMR, we can confirm that they are not associated with spin angular momentum but with the orbital angular momentum. In contrast, we can use the SMR amplitude to estimate the σ_{SH}^V value. Taking the spin diffusion length of V (λ_{SD}^V), which has been determined experimentally to be $\lambda_{SD}^V \sim 16$ nm for samples with similar resistivity [255,257], and $\tilde{g}_r^{\uparrow\downarrow}$ at the YIG/V interface, obtained from FMR, we can use Eq. (6.1) to estimate the absolute value of σ_{SH}. Our estimation, ~24 ($\hbar$/2e) $\Omega^{-1}cm^{-1}$, lies in the lowest limit of the range of

theoretical values [−13 to −90 ($\hbar$/e) Ω^{-1}cm^{-1}] [111,112,251,252], further evidencing the spin origin of the SMR.

Taking this into account, we will discuss the orbital transport parameters obtained from HMR. We find that they are in the same range as the ones reported for Mn with the same technique [102], with θ_{OH}^{V} being also similar to the value reported for Ti, $\theta_{OH}^{Ti} = 0.015 \pm 0.002$, by MOKE [104]. If we look at σ_{OH}^{V}, its magnitude is 2 orders lower than the theoretical value of the intrinsic orbital Hall conductivity, $\sigma_{OH}^{int} \sim 4500 - 6050$ ($\hbar$/e) Ω^{-1}cm^{-1} [111,112,251,252], a large difference that was also found for Mn [102] and might be explained by the large disorder in our sputtered thin films (see Sec. 6.5.7 for their structural characterization). The first theoretical works showed that, while the value of σ_{OH}^{int} is constant in the moderately dirty regime and does not depend on ρ, σ_{OH}^{int} is predicted to decrease approximately proportional to ρ^{-2} in the high-resistivity regime with large disorder [108], similar to the behaviour for σ_{SH}, in which these two regimes have been observed experimentally [167,258]. Although we observe a decrease of conductivity from $\sigma_{OH}^{V} = 78 \pm 4$ ($\hbar$/2e) Ω^{-1}cm^{-1} to $\sigma_{OH}^{V} = 63 \pm 3$ ($\hbar$/2e) Ω^{-1}cm^{-1} when resistivity increases from ρ_{L0}~270 μΩ·cm to ~380 μΩ·cm, it does not follow the ρ^{-2} trend. This suggests that we are at the stage where σ_{OH}^{int} starts to decrease but it does not justify the low σ_{OH}^{V} as compared with theoretical predictions. The large discrepancy existing between theoretical predictions and our measured σ_{OH} may stem from neglecting disorder-induced vertex corrections, which a recent work [259] shows can strongly suppress the σ_{OH} in certain cases. Furthermore, a newly introduced quantum-kinetic theory of electronic angular-momentum linear response [260,261] restricts the σ_{OH} to intraband contributions. In nonmagnetic, centrosymmetric light metals such as vanadium, this implies an intrinsic σ_{OH} that scales at least quadratically with the weak SOC, in contrast to conventional SOC-independent formulas, and hence naturally yields much smaller σ_{OH} values. A report on OHE in vanadium with lower resistivity ($\rho_{L0} \sim 41$ μΩ·cm) by MOKE quantifies both σ_{OH} and λ_{OD}, but the strong correlation between the two values prevents an independent quantification [20].

We next consider the orbital diffusion constant D_O, which provides complementary insight into the orbital transport dynamics, and we compare it to the charge diffusion constant D_q, which can be estimated using the Einstein relation $D_q = 1/\left(e^2 \rho N(E_F)\right)$. Here, e is the

elementary charge and $N(E_F)$ is the density of states at the Fermi level. Using the reported value for V, $N(E_F) \sim 28\times10^{22}$ $eV^{-1}cm^{-3}$ [262], we obtain $D_q^V \sim 8$ mm^2/s for the samples with lower resistivity ($\rho_{L0} \sim 270$ $\mu\Omega\cdot cm$). This value is four to six times larger than D_O^V extracted from the HMR fittings at the same sample (see Table 6.1). A difference between D_q and D_O has also been observed in Ti [104] and is in fact expected, according to theoretical studies [104,263]. In particular, the general theory of diffusion developed by X. Ning *et al.* [263] predicts that, while charge and spin diffusion constants are typically of similar magnitude, the orbital diffusion constant can be significantly lower, highlighting the distinct dynamics of orbital transport.

Interestingly, we find that D_O exhibits a more complex dependence on temperature and resistivity than initially expected. Specifically, a comparison of the same sample measured at 100 K and 290 K shows a clear increase in D_O with temperature, as given in Table 6.1, despite only a small change in resistivity because of the disordered metal behaviour. On the contrary, when comparing samples with significantly different resistivities (low- and high-resistivity datasets), at 290 K, we obtain nearly identical D_O values. To further investigate the relationship between D_O, resistivity and temperature, and confirm the robustness of the previous result, we performed an additional fitting on an 8-nm-thick film from the low-resistivity set (see Sec. 6.5.8 for more details). The obtained orbital transport parameters are consistent with those from the 6-nm-thick sample (see Table *6.3*). These results collectively suggest that D_O is more sensitive to temperature than to resistivity, which is predominantly determined by disorder. Although the origin of this behaviour remains unclear, it may motivate future theoretical studies.

Regarding the orbital diffusion length, we extract $\lambda_{OD}^V \sim 2$ nm which does not depend on the resistivity, suggesting it is robust against disorder. The obtained value is similar to the reported one by ST-FMR $\lambda_{OD}^V = 3.6$ nm [131]. λ_{OD}^V is also similar to the one reported for Cr, $\lambda_{OD}^{Cr} = 6.6 \pm 0.6$ nm, by MOKE [103] and to the one for Mn, $\lambda_{OD}^{Mn} \sim$ 2 nm, by HMR [102]. According to recent first-principles scattering calculations by M. Rang *et al.*, the orbital current decays rapidly, resulting in λ_{OD} of less than 1 nm, with $\lambda_{OD}^V = 0.5$ nm [54] for the specific case of V, and with no influence of disorder [47]. They suggest that the longer length scales being reported experimentally may arise because orbital current is converted into a spin current in a few atomic layers and what is being observed is the resulting spin diffusion length

(λ_{SD}) after orbital to spin current conversion. Experimental λ_{SD} values for V samples with similar resistivity are reported to be $\lambda_{SD}^{V} \sim 16$ nm [255,257]. Thus, our value $\lambda_{OD}^{V} \sim 2$ nm lies in between the theoretical orbital diffusion length and the experimental spin diffusion length, consistent with the previous hypothesis. Further studies are required to clarify the origin of the measured orbital transport parameters and the huge spread in the orbital diffusion lengths already reported [102–104,106,131,133,134,136,137].

6.4 Conclusions

In summary, we have studied the HMR and SMR effects in V thin films. We find a large HMR amplitude of the order of 10^{-4} in the range of thickness explored from 4 nm to 30 nm, while the SMR amplitude is one to two orders of magnitude smaller. These results, in combination with FMR in YIG/V, can be explained by the fact that V is a light metal with an expected large orbital Hall but small spin Hall contribution, i.e., the measured HMR arises mostly from the OHE. Furthermore, by fitting our results to the HMR equations, we are able to quantify the orbital transport parameters. We determine an orbital Hall conductivity $\sigma_{OH}^{V} \sim 78$ ($\hbar$/2e) $\Omega^{-1}\text{cm}^{-1}$ that slightly decreases when resistivity increases from $\rho_{L0} \sim 270$ to ~ 380 μΩ·cm, while the orbital diffusion length $\lambda_{OD}^{V} \sim 2$ nm remains independent of the resistivity in the same range. The large discrepancy between our experimentally obtained orbital Hall conductivity and the intrinsic one theoretically calculated may be related to the grade of disorder in our V thin films, which is not always fully considered in theoretical studies. Moreover, our study reveals a clear difference between charge and orbital diffusivities, a discrepancy that highlights the fundamentally different transport dynamics of orbital angular momentum. Further investigation is needed to clarify the impact of disorder on the suppression of orbital transport, particularly its role in limiting the magnitude of both the orbital Hall conductivity and the orbital diffusion length observed in disordered thin films.

6.5 Appendices

6.5.1 Resistivity of V thin films

We fabricated vanadium (V) thin films by sputtering following the deposition conditions specified in Sec. 6.2. By changing the pre-sputtering time, resistivities ranging between $\rho_{L0} \sim$ 171–464 μΩ·cm at

290 K were obtained. We chose the set of samples shown in Figure 6.5a in order to have similar resistivities with thicknesses up to 30 nm. The resistivity of the set of V samples remains in the range ρ_{L0}~256–278 μΩ·cm (at 100 K) for $t_V \geq 6$ nm (Figure 6.5a). The samples with thickness $t_V \geq 6$ nm show a metallic behavior with a resistance minimum below 100 K that changes with thickness, indicating a disordered thin film. A characteristic resistivity curve as a function of temperature is shown in Figure 6.5c, for a 6-nm-thick film and in Fig. 6.5d, for a 30-nm-thick film. The resistivity obtained for samples with $t_V < 6$ nm was always higher, showing an increase with decreasing temperature in the whole temperature range (10-300 K), characteristic of a more disordered metal than thicker films (Figure 6.5b). Despite this, we saw an important decrease in the amplitude of the HMR as expected for a diffusive phenomenon (see Figure 6.2a and 6.2c).

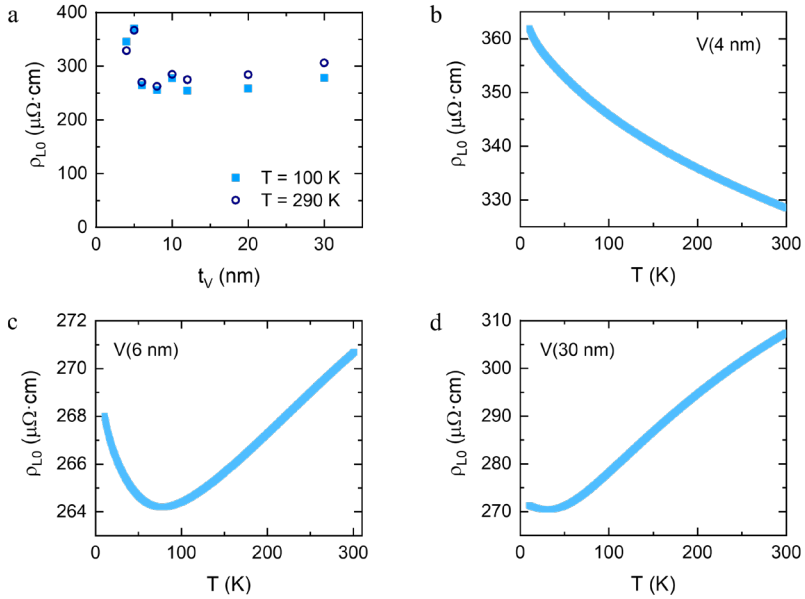

Figure 6.5. Resistivity of V thin films. (a) Resistivity of the set of V thin films with varying thickness, at 100 K and 290 K. (b-d) Resistivity of the 4-, 6-, and 30-nm-thick V films as a function of temperature.

6.5.2 Longitudinal magnetoresistance measurements

Figure 6.6a shows a characteristic longitudinal ADMR measurement, performed in the sample Si/SiO_2/V(8 nm)/SiO_2(5 nm) along the three

rotation planes (α, β, γ). The temperature dependence of each ADMR amplitude is plotted in Figure 6.6b.

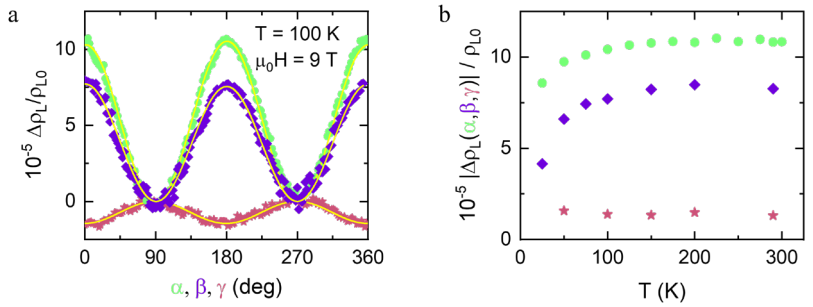

Figure 6.6. Longitudinal magnetoresistance measurements. (a) Longitudinal ADMR measurements at $\mu_0 H$ = 9 T and T = 100 K along the three rotation planes (α, β, γ). Yellow lines correspond to a $cos^2(\alpha, \beta)$ and a $sin^2(\gamma)$ fit. (b) Amplitude of the ADMR as a function of temperature. Data corresponds to the 8-nm-thick V film.

6.5.3 Transverse magnetoresistance measurements

The transverse FDMR measurements with the magnetic field H applied along the three main axes (x, y and z) are shown in Figure 6.7. The transverse resistivity shows a nonlinear relation with the magnetic field along z, with different slopes at low and high magnetic fields. The linear trend at high fields comes from the ordinary Hall effect, expected for a NM metal [63]. To extract the HMR contribution from the transverse FDMR, we perform a linear fit in the high field regime between -7 T and -9 T (see light blue data in Figure 6.7). Then, this linear fit is subtracted from the measured data (blue data in Figure 6.7) to eliminate the ordinary Hall contribution, and Figure 6.1d is obtained.

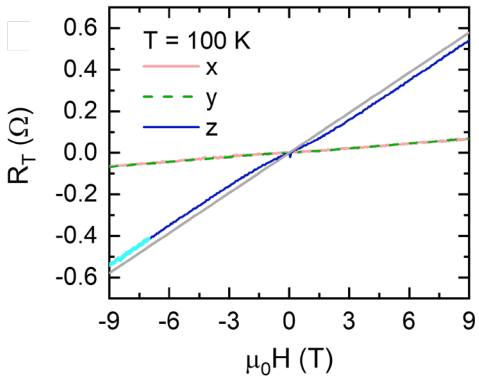

Figure 6.7. Transverse magnetoresistance measurements. Measured transverse FDMR at T = 100 K for the 6-nm-thick sample, with the magnetic field H applied along the three main axes. The light blue data represents the region used to perform the linear fit when H is along z. The grey line is the extrapolation of the linear fit that helps to visualize the change of trend between the low field and high field regime due to the ordinary Hall effect. A constant offset has been subtracted.

6.5.4 Hanle magnetoresistance of high resistive samples

As discussed in Sec. 6.5.1, V films with the same thickness but different resistivities (in the range ρ_{L0}~ 171–464 μΩ·cm) were obtained. We perform ADMR measurements in a set of samples (6-nm-thick and 10-nm-thick) with different resistivities at $\mu_0 H$ = 9 T and T=290 K (Figure 6.8a). A representative result of the ADMR, from a 6-nm-thick film with a resistivity of $\rho_{L0} = 378$ μΩ·cm at 290 K, is plotted as $\Delta\rho_L/\rho_{L0} = \Delta R_L/R_L = [R_L(\alpha,\beta) - R_L(90°)]/R_L(90°)$ in Figure 6.8b. Moreover, the longitudinal and transverse FDMR show the characteristic HMR behavior, as shown in Figure 6.8c and Figure 6.8d.

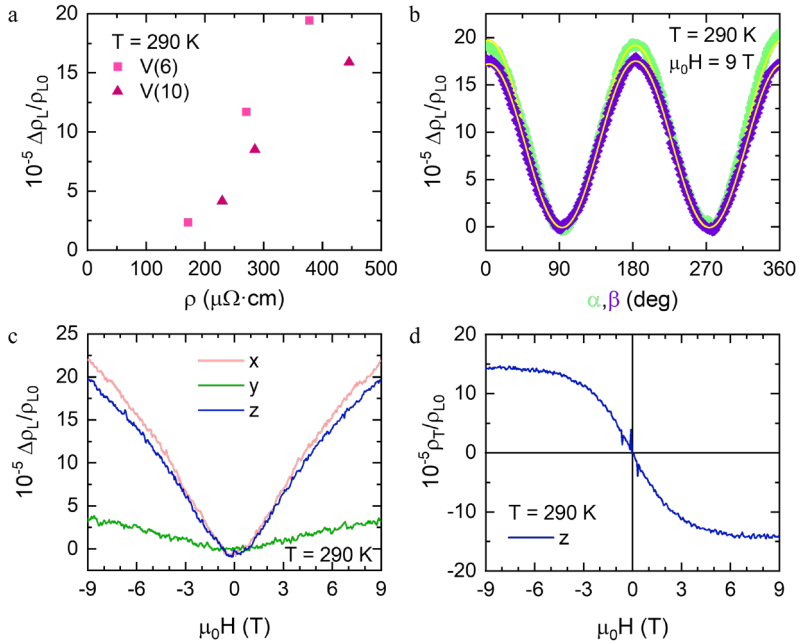

Figure 6.8. Hanle magnetoresistance of high resistive samples. (a) Amplitude of the HMR taken from ADMR measurements, in α plane at T = 290 K and $\mu_0 H$ = 9 T, as a function of the resistivity for different samples with V thicknesses of 6 and 10 nm. (b) ADMR measurement at T = 290 K and $\mu_0 H$ = 9 T in α and β planes. Yellow lines are a $cos^2(\alpha, \beta)$ fit. (c) Longitudinal and (d) transverse FDMR measurements performed at T = 290 K with H applied along the main axes. Data in (b), (c) and (d) correspond to sample Si/SiO_2/V(6 nm)/SiO_2(5 nm) with ρ_{L0} = 378 μΩ·cm.

6.5.5 Orbital transport parameters of high resistivity samples

Taking into consideration the change of HMR amplitude in samples with high resistivity, we use Eqs. (2.39) and (2.40) to analyze the impact of increasing the resistivity in the orbital transport parameters. To do so, we perform a simultaneous fit with 3 free parameters (θ_{OH}, λ_{OD}, and D_O) of the thickness dependence data set of high-resistivity samples (ρ_{L0}~378–464 μΩ·cm) and the longitudinal and transverse FDMRs of a 6-nm-thick sample with a resistivity of ρ_{L0} = 378 μΩ·cm, at 290 K (see Figure 6.9). This allows us to get the orbital transport parameters: θ_{OH}, λ_{OD}, and D_O shown in Table 6.1.

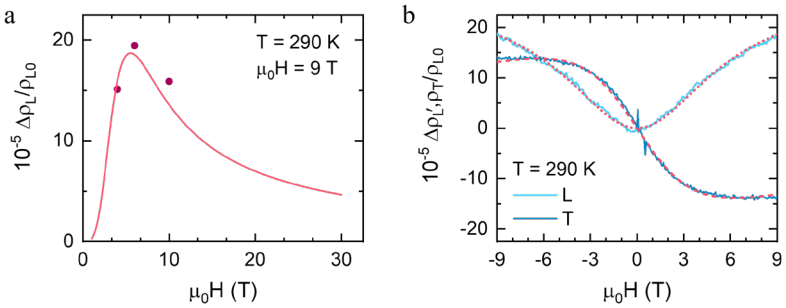

Figure 6.9. HMR thickness and field dependence in V thin films with fittings to the HMR equations. (a) Longitudinal HMR amplitude of high-resistivity samples at 9 T extracted from the ADMR measurements in α plane (pink solid circles) as a function of thickness at 290 K, with its corresponding fitting of Eq. (2.39) (red solid line). (b) Longitudinal (L, light blue line) and transverse (T, dark blue line) FDMR at 290 K of the 6-nm-thick sample with high resistivity ($\rho_{L0} = 378$ μΩ·cm), with their respective fittings of Eq. (2.39) (dotted lines) and Eq. (2.40) (dashed lines).

Furthermore, to assess the impact of the fitting method on the extracted orbital transport parameters, we have also performed a triple-variable fit for the low-resistivity sample and the low-resistivity dataset (results are shown in Table 6.2). This change in fitting procedure does not significatively affect the extracted parameter values. The errors in Table 6.2 correspond to the statistical errors obtained from the fitting procedure, which, in the case of the fitting method described in section 6.3 for the low-resistivity sample ("Method 1") cannot be quantified for certain parameters. The errors used in Table 6.1 correspond to an overall estimated error coming from several sources.

Table 6.2. Orbital transport parameters of V extracted from the fittings at 290 K. Method 1 refers to the fitting procedure where λ_{OD} is first extracted using the thickness dependence dataset, followed by the fitting of the other two parameters (θ_{OH} and D_O) using the longitudinal and transverse FDMR datasets. Method 2 refers to the simultaneous triple-variable fitting approach using the three datasets.

Method	ρ_{L0} (μΩ·cm)	λ_{OD}^V (nm)	θ_{OH}^V	D_O^V (mm²/s)	τ_O^V (ps)	σ_{OH}^V [($\hbar$/2e) Ω⁻¹cm⁻¹]

1	270.3	2.1	0.0214	2.16 ± 0.02	2.04 ± 0.01	79
2	270.3	2.2 ± 0.1	0.021 ± 0.004	2.3 ± 0.1	2.16 ± 0.1	77 ± 1
2	378.1	2.09 ± 0.07	0.0240 ± 0.0003	2.00 ± 0.06	2.18 ± 0.07	63.5 ± 0.8

6.5.6 Magnetoresistance measurements on YIG

As shown in Sec. 6.3, Si/SiO_2/V samples with thickness similar to YIG/V(7nm) shows a higher HMR amplitude (compare amplitudes in Figure 6.1b with Figure 6.3c), even though the samples have comparable resistivities ($\rho_{L0}^{YIG/V(7)} = 295$ μΩ·cm and $\rho_{L0}^{Si/SiO2/V(6)} =$ 264 μΩ·cm at 100 K). This difference arises because of the fabrication process: while YIG/V(7nm) sample was fabricated using an etching process, Si/SiO_2/V samples were fabricated using a lift-off procedure. The change in fabrication method was chosen in order to have a clean interface in the YIG samples, which is crucially important to have a proper transmission of spins (i.e., large spin-mixing conductance) and, consequently, a reliable SMR signal. However, this change of fabrication method results in a reduced HMR signal for the YIG/V samples.

To clarify this point and demonstrate that the observed difference is due to the fabrication method and not to the resistivity or significant changes in the microstructure that could have affected the amplitude of the signal, we show in Figure 6.10 a sister sample deposited and fabricated at the same time, but on a Si/SiO_2 substrate ($\rho_{L0}^{Si/SiO_2/V(7)} = 302$ μΩ·cm). This means that both samples were sputtered and ion-beam etched simultaneously. As shown in Figure 6.10, both samples exhibit similar ADMR amplitudes, but lower than those obtained with the lift-off procedure. The different fabrication method may have introduced some resist residues or solvent degradation that affected the signal. In any case, it is important to note that there is still a difference of more than one order of magnitude between the SMR (Figure 6.3b) and HMR (Figure 6.3c and Figure 6.10) signals.

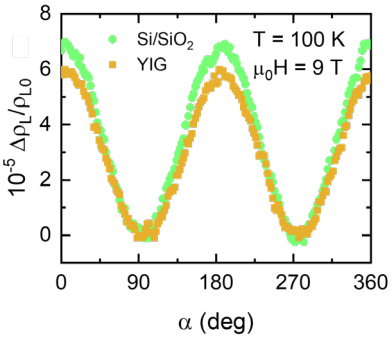

Figure 6.10. Angular-dependent magnetoresistance measurement at T =100 K and $\mu_0 H$ = 9 T in α plane for V(7nm) deposited on two different substrates: Si/SiO_2 and YIG. The two devices are processed with negative lithography and etching.

6.5.7 Structural characterization of V samples

We have performed X-ray diffraction (XRD) and reflectivity (XRR) to know the degree of crystallinity/disorder and thickness of the vanadium films, as well as atomic force microscopy (AFM) to quantify their roughness. Figure 6.11a shows the XRD patterns of $Si/SiO_2/V(t_V$ nm$)/SiO_2$(5 nm) thin films, with $t_V = 5$ and 30 nm, deposited together with the Hall bar samples used for magnetoresistance measurements. The absence of vanadium diffraction peaks indicates that the thin films have a very low crystallinity or are even amorphous, confirming their disordered nature. Figure 6.11b presents the corresponding XRR measurements, used to calibrate the thickness of the films. The similar decay in intensity observed for both thicknesses suggests that the films have comparable roughness. From the AFM scans, shown in Figure 6.11c and Figure 6.11d, the roughness mean square (r.m.s.) of the thin films are estimated to be around 0.5 nm in both cases, corresponding to the two ends of the thickness range used in the present study.

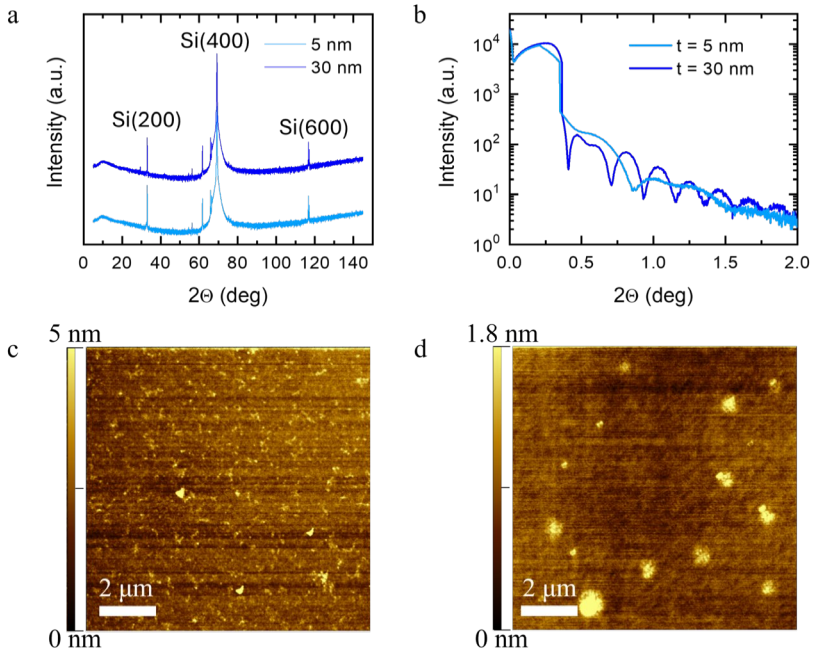

Figure 6.11. Structural characterization of V samples. (a) XRD spectra, (b) XRR, and (c,d) AFM from sputtered thin films of Si/SiO_2/V(t_V nm)/SiO_2 with t_V=5 and 30 nm, respectively.

6.5.8 Orbital transport parameters of 8-nm-thick low-resistivity sample

To further investigate the robustness of the orbital transport parameters, we performed an additional fitting for a low-resistive 8-nm-thick sample (see Figure 6.12). The extracted orbital transport parameters, shown in Table 6.3, are consistent with those obtained for the 6-nm-thick sample. Furthermore, both samples follow the same trend with temperature, reinforcing the robustness of the observed trends.

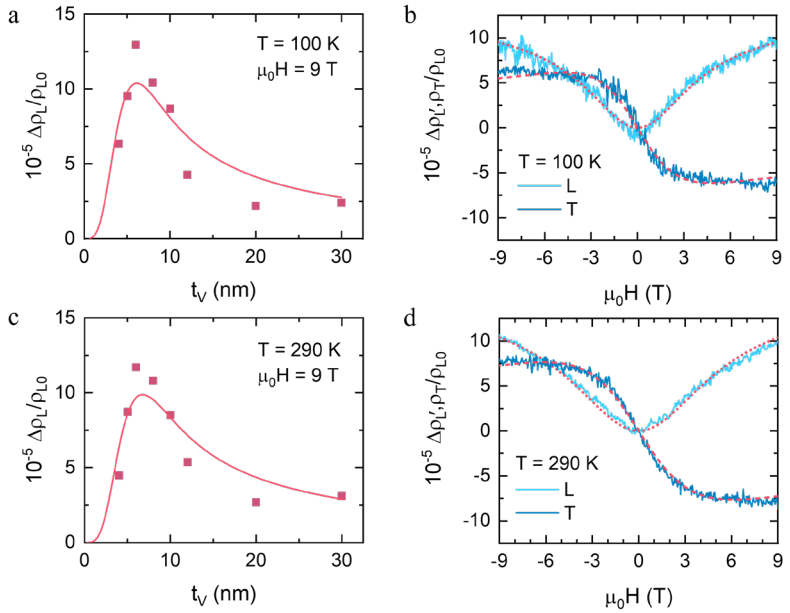

Figure 6.12. HMR thickness and field dependence in V thin films with fittings to the HMR equations. (a) and (c) Longitudinal HMR amplitude at 9 T extracted from the ADMR measurements in α plane (pink solid squares) as a function of thickness at 100 K and 290 K, respectively, with their corresponding fittings of Eq. (2.39) (red solid line). (b) and (d) Longitudinal (L) (light blue line) and transverse (T) (dark blue line) FDMR for sample Si/SiO_2/V(8 nm)/SiO_2(5 nm) at 100 K and 290 K, respectively, with their corresponding fittings of Eq. (2.39) (dotted lines) and Eq. (2.40) (dashed lines).

Table 6.3. Orbital transport parameters of V extracted from the fittings at 100 K and 290 K for sample Si/SiO_2/V(8 nm)/SiO_2(5 nm).

T (K)	ρ_{L0} (μΩ·cm)	λ_{OD}^{V} (nm)	θ_{OH}^{V}	D_O^V (mm^2/s)	τ_O^V (ps)	σ_{OH}^{V} [$(\hbar/2e)\ \Omega^{-1}cm^{-1}$]
100	255.9	1.8 ± 0.3	0.019 ± 0.001	1.51 ± 0.5	2.14 ± 0.2	74 ± 4
290	262.7	2.1 ± 0.3	0.020 ± 0.001	2.46 ± 0.8	1.79 ± 0.2	76 ± 4

Chapter 7
Conclusions and outlook

This thesis focuses on the study of angular momentum transport. Since the emergence of spintronics more than three decades ago with the discovery of GMR, research has largely concentrated on spin transport mediated by conduction electrons. Beyond this, however, it is also possible to take advantage of the collective motion of spins (spin waves or magnons), which can propagate in any magnetically ordered material, including insulators. In parallel, the role of orbital angular momentum, once considered negligible in comparison to spin, is now recognized as an active channel for information transport. Because of this recognition, orbitronics has arisen as a new alternative that exploits the flow of orbital angular momentum. Together, these developments have uncovered a rich variety of phenomena resulting from the generation, propagation and detection of spin and orbital currents, highlighting their potential for future spintronic and orbitronics technologies. Moreover, a significant advantage of these mechanisms is their compatibility with conventional electronics, offering promising routes for integration into future information technologies.

In this thesis, through magnetotransport and ferromagnetic resonance experiments, we explore the transport of spins in a prototypical ferromagnetic insulator, and of orbital angular momentum in a 3d metal, aiming to advance the current understanding of these phenomena. Here, we summarize the main results and discuss future perspectives towards the implementation of functional spin- and orbital-based devices.

First, we carried out a comprehensive study on insulating EuS thin films, a material widely used due to its ability to induce an extremely strong exchange field at interfaces with a broad range of materials. Our approach combined the investigation of SMR, local and non-local magnon transport and the magnetization dynamics of EuS, including Gilbert damping, thereby linking magnon diffusion to the intrinsic magnetic relaxation of the system.

In **Chapter 4**, we observe SMR and demonstrated the transport of incoherent magnon currents in Pt/EuS heterostructures below T_C. The SMR amplitude indicates efficient spin transmission at the EuS/Pt

interface. Motivated by this, we investigated the transport of magnon currents, comparing local and non-local signals. We confirmed the generation and propagation of thermally induced magnon currents through the temperature and field dependence, consistent with the magnetic origin. Finally, the thickness dependence of the non-local signal revealed a decay consistent with thermally generated magnons in the relaxation regime, with a magnon diffusion length of $\lambda_m^{th} = 140 \pm 30$ nm at 2 K and 0.3 T, establishing EuS as a reference ferromagnetic insulator for magnon transport studies.

In **Chapter 5** we investigated the low-temperature magnetization dynamics of EuS thin films grown on different substrates, and therefore, exhibiting different structural properties. The experimental results show that the Gilbert damping decreases by one order of magnitude when the thickness increases from 20 nm to 40 nm, reaching 10^{-3} below 10 K, while the crystallinity of the samples has a comparatively minor effect on the magnetic losses. This thickness dependence is attributed to stoichiometric defects at the substrate/film interface, suggesting that improving interface quality could further reduce damping. The similar values obtained for epitaxial and polycrystalline films indicate that less demanding growth conditions may still be suitable for device fabrication. These results underline the potential of EuS for magnonic and spintronic applications, expanding the range of viable ferromagnetic insulator.

Looking ahead, EuS emerges as a particularly attractive platform for future applications at cryogenic temperatures, where conventional semiconducting or metallic technologies become inefficient. Hybrid EuS/superconductor systems are specially promising. For instance, V/EuS bilayers have recently been used to realize highly efficient superconducting diodes and rectifiers for quantum circuitry, showing that the combination of ferromagnetic exchange fields and superconductivity would help to significantly reduce energy consumption and mitigate decoherence from thermal and electromagnetic noise [264].

Beyond superconducting diodes, the interaction between magnon currents in EuS and superconductivity opens additional possibilities. Spin-split superconductors have been predicted to host thermoelectric

effects that could be harnessed in cryogenic heat engines, converting waste thermal energy into useful electrical signals [265].

Finally, the favourable damping characteristics of EuS, even in polycrystalline films, make it suitable for the fabrication of magnonic waveguides and magnetic nanostructures. The possibility of growing such films on cold substrates compatible with standard lithographic resist such as PMMA, further simplifies its integration in magnonic and spintronic devices.

In summary, EuS proves to be not only suitable for fundamental studies [266], but also for future magnonic, spintronic and superconducting devices at cryogenic temperatures. Furthermore, beyond spin-based transport, EuS related chalcogenides (EuSX) are gaining attention in the emerging field of orbitronics [267]. In this sense, the study of orbital currents in **Chapter 6**, provides a complementary approach to understand and further expand the knowledge of spin- and orbital-based phenomena.

In **Chapter 6** we explored vanadium, a 3d metal with weak spin-orbit coupling, which exhibits a large Hanle magnetoresistance. Combining HMR and FMR measurements, we quantified the key orbital transport parameters ($\sigma_{OH}^{V} \sim 78$ ($\hbar$/2e) Ω^{-1}cm^{-1} and $\lambda_{OD}^{V} \sim 2$ nm), confirming the orbital origin of the observed signals. These results provide a detailed characterization of orbital current propagation in vanadium making HMR a suitable technique to characterize a broad class of materials with either strong or weak spin-orbit coupling.

Despite the potential of orbitronics, fundamental questions remain open. For instance, the orbital diffusion length which is reported to vary from a few nm to several tens of them, requires further clarification. Moreover, unlike conventional spintronics, which typically relies on materials with strong spin-orbit coupling, orbitronics cover a broad class of materials. Orbital contributions have already been shown to play a significant role in systems traditionally associated with spin transport. Understanding the role of spin and orbital degrees of freedom in angular momentum transport requires further exploration.

Overall, this thesis deepens our understanding of spin- and orbital-based phenomena, with EuS as a reference material for cryogenic studies and applications and vanadium as reference material for orbital

studies. Together, they demonstrate their relevance for future research on spin- and orbital- based technologies.

Bibliography

[1] P. A. Wayman, Stoney's Electron, Europhysics News **28**, 159 (1997).

[2] J. D. Meindl, *History of Low Power Electronics: How It Began and Where It's Headed*, in *International Symposium on Low Power Electronics and Design, Digest of Technical Papers* (1997), pp. 149–151.

[3] M. J. Riezenman, Wanlass's Cmos Circuit, IEEE Spectr **28**, 44 (1991).

[4] G. E. Moore, Cramming more components onto integrated circuits, Reprinted from Electronics, volume 38, number 8, April 19, 1965, pp.114 ff., IEEE Solid-State Circuits Society Newsletter **11**, 33 (2009).

[5] G. E. Moore, Progress in digital integrated electronics [Technical literaiture, Copyright 1975 IEEE. Reprinted, with permission. Technical Digest. International Electron Devices Meeting, IEEE, 1975, pp. 11-13.], IEEE Solid-State Circuits Society Newsletter **11**, 36 (2009).

[6] H. F. Sheikh, I. Ahmad, Z. Wang, and S. Ranka, An overview and classification of thermal-aware scheduling techniques for multi-core processing systems, Sustainable Computing: Informatics and Systems **2**, 151 (2012).

[7] E. Le Sueur and G. Heiser, *Dynamic Voltage and Frequency Scaling: The Laws of Diminishing Returns*, in *HotPower 2010 - 2010 Workshop on Power Aware Computing and Systems* (2010).

[8] R. K. Gupta, *Handbook of Semiconductors* (CRC Press, Boca Raton, 2024).

[9] S. Manipatruni, D. E. Nikonov, C. C. Lin, T. A. Gosavi, H. Liu, B. Prasad, Y. L. Huang, E. Bonturim, R. Ramesh, and I. A. Young, Scalable energy-efficient magnetoelectric spin–orbit logic, Nature **565**, 35 (2019).

[10] B. Dieny et al., Opportunities and challenges for spintronics in the microelectronics industry, Nat Electron **3**, 446 (2020).

[11] J. A. C. Incorvia et al., Spintronics for achieving system-level energy-efficient logic, Nature Reviews Electrical Engineering **1**, 700 (2024).

[12] A. Pais, George Uhlenbeck and the discovery of electron spin, Phys Today **42**, 34 (1989).

[13] K. V. Shanavas, Z. S. Popović, and S. Satpathy, Theoretical model for Rashba spin-orbit interaction in d electrons, Phys Rev B **90**, 165108 (2014).

[14] C. Kittel, Introduction to Solid State Physics, 8th edition, Wiley & Sons, New York, NY (2004).

[15] C. Chappert, A. Fert, and F. N. Van Dau, The emergence of spin electronics in data storage, Nat Mater **6**, 813 (2007).

[16] A. V. Chumak, V. I. Vasyuchka, A. A. Serga, and B. Hillebrands, Magnon spintronics, Nat Phys **11**, 453 (2015).

[17] A. Hoffmann and S. D. Bader, Opportunities at the frontiers of spintronics, Phys Rev Appl **4**, 047001 (2015).

[18] D. Jo, D. Go, G.-M. Choi, and H.-W. Lee, Spintronics meets orbitronics: Emergence of orbital angular momentum in solids, Npj Spintronics **2**, 19 (2024).

[19] M. N. Baibich, J. M. Broto, A. Fert, F. Nguyen, V. Dau, F. Petroff, P. Eitenne, G. Creuzet, A. Friederich, and J. Chazelas, Giant Magnetoresistance of (001)Fe/(001)Cr Magnetic Superlattices, Phys Rev Lett **61**, 2472 (1988).

[20] G. Binasch, P. Grünberg, F. Saurenbach, and W. Zinn, Enhanced magnetoresistance in layered magnetic structures with antiferromagnetic interlayer exchange, Phys Rev B **39**, 4828 (1989).

[21] E. E. Fullerton and J. R. Childress, Spintronics, Magnetoresistive Heads, and the Emergence of the Digital World, Proceedings of the IEEE **104**, 1787 (2016).

[22] S. Bhatti, R. Sbiaa, A. Hirohata, H. Ohno, S. Fukami, and S. N. Piramanayagam, Spintronics based random access memory: a review, Materials Today **20**, 530 (2017).

[23] Y. Zhang, W. Zhao, J.-O. Klein, W. Kang, D. Querlioz, Y. Zhang, D. Ravelosona, and C. Chappert, *Spintronics for Low-Power Computing*, in *2014 Design, Automation & Test in Europe Conference & Exhibition* (Dresden, 2014).

[24] A. Brataas, B. van Wees, O. Klein, G. de Loubens, and M. Viret, Spin insulatronics, Phys Rep **885**, 1 (2020).

[25] M. Althammer, All-Electrical Magnon Transport Experiments in Magnetically Ordered Insulators, Physica Status Solidi - Rapid Research Letters **15**, 2100130 (2021).

[26] K. Nakata, P. Simon, and D. Loss, Spin currents and magnon dynamics in insulating magnets, J Phys D Appl Phys **50**, 114004 (2017).

[27] H. J. V. Tyrrell, The origin and present status of fick's diffusion law, J Chem Educ **41**, 397 (1964).

[28] S. M. Rezende, *Fundamentals of Magnonics* (Springer Cham, 2020).

[29] The electrical conductivity of transition metals, Proc R Soc Lond A Math Phys Sci **153**, 699 (1936).

[30] R. J. Weiss and A. S. Marotta, Spin-dependence of the resistivity of magnetic metals, Journal of Physics and Chemistry of Solids **9**, 302 (1959).

[31] I. A. Campbell, A. Fert, and R. Pomeroy, Evidence for two current conduction iron, Philosophical Magazine **15**, 977 (1967).

[32] A. Fert and I. A. Campbell, Two-current conduction in nickel, Phys Rev Lett **21**, 1190 (1968).

[33] J. M. D. Coey, *Magnetism and Magnetic Materials* (Cambridge University Press, 2010).

[34] W. Han, S. Maekawa, and X. C. Xie, Spin current as a probe of quantum materials, Nat Mater **19**, 139 (2020).

[35] P. Pirro, V. I. Vasyuchka, A. A. Serga, and B. Hillebrands, Advances in coherent magnonics, Nat Rev Mater **6**, 1114 (2021).

[36] L. J. Cornelissen, K. J. H. Peters, G. E. W. Bauer, R. A. Duine, and B. J. van Wees, Magnon spin transport driven by the magnon chemical potential in a magnetic insulator, Phys Rev B **94**, 014412 (2016).

[37] Y. Tserkovnyak, A. Brataas, and G. E. W. Bauer, Spin pumping and magnetization dynamics in metallic multilayers, Phys Rev B **66**, 224403 (2002).

[38] Y. Tserkovnyak, A. Brataas, and G. E. W. Bauer, Enhanced Gilbert Damping in Thin Ferromagnetic Films, Phys Rev Lett **88**, 117601 (2002).

[39] E. I. Rashba, Theory of electrical spin injection: Tunnel contacts as a solution of the conductivity mismatch problem, Phys Rev B **62**, R16267(R) (2000).

[40] H. Adachi, K. I. Uchida, E. Saitoh, and S. Maekawa, Theory of the spin Seebeck effect, Reports on Progress in Physics **76**, 036501 (2013).

[41] K. Uchida, S. Takahashi, K. Harii, J. Ieda, W. Koshibae, K. Ando, S. Maekawa, and E. Saitoh, Observation of the spin Seebeck effect, Nature **455**, 778 (2008).

[42] M. I. Dyakonov and V. I. Perel, Current-induced spin orientation of electrons in semiconductors, Phys Lett A **35**, 459 (1971).

[43] A. Hoffmann, Spin Hall Effects in Metals, IEEE Trans Magn **49**, 5172 (2013).

[44] M. Althammer, Pure spin currents in magnetically ordered insulator/normal metal heterostructures, J Phys D Appl Phys **51**, 313001 (2018).

[45] T. Kimura, Y. Otani, T. Sato, S. Takahashi, and S. Maekawa, Room-temperature reversible spin hall effect, Phys Rev Lett **98**, 156601 (2007).

[46] A. Manchon and A. Belabbes, *Spin-Orbitronics at Transition Metal Interfaces*, in *Solid State Physics - Advances in Research and Applications*, Vol. 68 (2017), pp. 1–89.

[47] M. Weiler et al., Experimental test of the spin mixing interface conductivity concept, Phys Rev Lett **111**, 176601 (2013).

[48] T. Valet and A. Fert, Theory of the perpendicular magnetoresistance in magnetic multilayers, Phys Rev B **48**, 7099 (1993).

[49] J. Bass and W. P. Pratt, Spin-diffusion lengths in metals and alloys, and spin-flipping at metal/metal interfaces: An experimentalist's critical review, Journal of Physics Condensed Matter **19**, 183201 (2007).

[50] L. J. Cornelissen, J. Liu, R. A. Duine, J. ben Youssef, and B. J. van Wees, Long-distance transport of magnon spin information in a magnetic insulator at room temperature, Nat Phys **11**, 1022 (2015).

[51] X.-Y. Wei, O. A. Santos, C. H. S. Lusero, G. E. W. Bauer, J. Ben Youssef, and B. J. van Wees, Giant magnon spin conductivity in ultrathin yttrium iron garnet films, Nat Mater **21**, 1352 (2022).

[52] W. Yuan et al., Experimental signatures of spin superfluid ground state in canted antiferromagnet Cr2O3 via nonlocal spin transport, Sci Adv **4**, eaat1098 (2018).

[53] P. Muduli, R. Schlitz, T. Kosub, R. Hübner, A. Erbe, D. Makarov, and S. T. B. Goennenwein, Local and nonlocal spin Seebeck effect in lateral Pt-Cr2O3-Pt devices at low temperatures, APL Mater **9**, 021122 (2021).

[54] R. Lebrun, A. Ross, S. A. Bender, A. Qaiumzadeh, L. Baldrati, J. Cramer, A. Brataas, R. A. Duine, and M. Kläui, Tunable long-distance spin transport in a crystalline antiferromagnetic iron oxide, Nature **561**, 222 (2018).

[55] R. Lebrun, A. Ross, O. Gomonay, V. Baltz, U. Ebels, A. L. Barra, A. Qaiumzadeh, A. Brataas, J. Sinova, and M. Kläui, Long-distance spin-transport across the Morin phase transition up to room temperature in ultra-low damping single crystals of the antiferromagnet α-Fe2O3, Nat Commun **11**, 6332 (2020).

[56] Y. T. Chen, S. Takahashi, H. Nakayama, M. Althammer, S. T. B. Goennenwein, E. Saitoh, and G. E. W. Bauer, Theory of spin Hall magnetoresistance, Phys Rev B **87**, 144411 (2013).

[57] T. Kosub, S. Vélez, J. M. Gomez-Perez, L. E. Hueso, J. Fassbender, F. Casanova, and D. Makarov, Anomalous Hall-like transverse magnetoresistance in Au thin films on Y3Fe5O12, Appl Phys Lett **113**, 222409 (2018).

[58] S. Vélez, A. Bedoya-Pinto, W. Yan, L. E. Hueso, and F. Casanova, Competing effects at Pt/YIG interfaces: Spin Hall magnetoresistance, magnon excitations, and magnetic frustration, Phys Rev B **94**, 174405 (2016).

[59] M. Althammer et al., Quantitative study of the spin Hall magnetoresistance in ferromagnetic insulator/normal metal hybrids, Phys Rev B **87**, 224401 (2013).

[60] N. Vlietstra, J. Shan, V. Castel, J. Ben Youssef, G. E. W. Bauer, and B. J. Van Wees, Exchange magnetic field torques in YIG/Pt bilayers observed by the spin-Hall magnetoresistance, Appl Phys Lett **103**, 032401 (2013).

[61] M. I. Dyakonov, Magnetoresistance due to edge spin accumulation, Phys Rev Lett **99**, 126601 (2007).

[62] S. Vélez, V. N. Golovach, A. Bedoya-Pinto, M. Isasa, E. Sagasta, M. Abadia, C. Rogero, L. E. Hueso, F. S. Bergeret, and F. Casanova, Hanle Magnetoresistance in Thin Metal Films with Strong Spin-Orbit Coupling, Phys Rev Lett **116**, 016603 (2016).

[63] J. Li, A. H. Comstock, D. Sun, and X. Xu, Comprehensive demonstration of spin Hall Hanle effects in epitaxial Pt thin films, Phys Rev B **106**, 184420 (2022).

[64] K. Uchida, M. Ishida, T. Kikkawa, A. Kirihara, T. Murakami, and E. Saitoh, Longitudinal spin Seebeck effect: From fundamentals to applications, Journal of Physics Condensed Matter **26**, 343202 (2014).

[65] S. Bosu, Y. Sakuraba, K. Uchida, K. Saito, T. Ota, E. Saitoh, and K. Takanashi, Spin Seebeck effect in thin films of the Heusler compound Co2MnSi, Phys Rev B **83**, 224401 (2011).

[66] K. Uchida et al., Spin Seebeck insulator, Nat Mater **9**, 894 (2010).

[67] K. I. Uchida, H. Adachi, T. Ota, H. Nakayama, S. Maekawa, and E. Saitoh, Observation of longitudinal spin-Seebeck effect in magnetic insulators, Appl Phys Lett **97**, 172505 (2010).

[68] N. Ito, T. Kikkawa, J. Barker, D. Hirobe, Y. Shiomi, and E. Saitoh, Spin Seebeck effect in the layered ferromagnetic insulators CrSiTe3 and CrGeTe3, Phys Rev B **100**, 060402 (2019).

[69] K. I. Uchida, Transport phenomena in spin caloritronics, Proc Jpn Acad Ser B Phys Biol Sci **97**, 69 (2020).

[70] K. Ganzhorn, T. Wimmer, J. Cramer, R. Schlitz, S. Geprägs, G. Jakob, R. Gross, H. Huebl, M. Kläui, and S. T. B. Goennenwein, Temperature dependence of the non-local spin Seebeck effect in YIG/Pt nanostructures, AIP Adv **7**, 085102 (2017).

[71] J. M. Gomez-Perez, S. Vélez, L. E. Hueso, and F. Casanova, Differences in the magnon diffusion length for electrically and thermally driven magnon currents in Y3 F e5 O12, Phys Rev B **101**, 184420 (2020).

[72] J. Shan, L. J. Cornelissen, J. Liu, J. Ben Youssef, L. Liang, and B. J. Van Wees, Criteria for accurate determination of the magnon relaxation length from the nonlocal spin Seebeck effect, Phys Rev B **96**, 184427 (2017).

[73] E. L. L. LANDAU, On the theory of dispersion of magnetic permeabilty in ferromagnetic bodies, Phys. Zeitsch. Der Sow. **8**, 153 (1935).

[74] T. L. Gilbert, A phenomenological theory of damping in ferromagnetic materials, IEEE Trans Magn **40**, 3443 (2004).

[75] S. Wu et al., Room-temperature intrinsic and extrinsic damping in polycrystalline Fe thin films, Phys Rev B **105**, 174408 (2022).

[76] S. Mankovsky, D. Ködderitzsch, G. Woltersdorf, and H. Ebert, First-principles calculation of the Gilbert damping parameter via the linear response formalism with application to magnetic transition metals and alloys, Phys Rev B **87**, 014430 (2013).

[77] H. Yu, R. Huber, T. Schwarze, F. Brandl, T. Rapp, P. Berberich, G. Duerr, and D. Grundler, High propagating velocity of spin waves and temperature dependent damping in a CoFeB thin film, Appl Phys Lett **100**, 262412 (2012).

[78] A. Widom, C. Vittoria, and S. D. Yoon, Gilbert ferromagnetic damping theory and the fluctuation-dissipation theorem, J Appl Phys **108**, 073924 (2010).

[79] S. Emori and P. Li, Ferrimagnetic insulators for spintronics: Beyond garnets, J Appl Phys **129**, 020901 (2021).

[80] O. Yalcin, *Ferromagnetic Resonance - Theory and Applications* (IntechOpen, 2013).

[81] S. Azzawi, A. T. Hindmarch, and D. Atkinson, Magnetic damping phenomena in ferromagnetic thin-films and multilayers, J Phys D Appl Phys **50**, 473001 (2017).

[82] V. Franco and B. Dodrill, editors, *Magnetic Measurement Techniques for Materials Characterization* (Springer International Publishing, Cham, 2021).

[83] C. Kittel, On the theory of ferromagnetic resonance absorption, Physical Review **73**, 155 (1948).

[84] M. C. Hickey and J. S. Moodera, Origin of intrinsic Gilbert damping, Phys Rev Lett **102**, 137601 (2009).

[85] A. Barman and J. Sinha, *Spin Dynamics and Damping in Ferromagnetic Thin Films and Nanostructures* (Springer Cham, 2017).

[86] V. Kamberský, On ferromagnetic resonance damping in metals, Czechoslovak Journal of Physics **26**, 1366 (1976).

[87] Z. Xu, K. Zhang, and J. Li, Disentangling intrinsic and extrinsic Gilbert damping, Phys Rev B **104**, 224404 (2021).

[88] M. Sparks, R. Loudon, and C. Kittel, Ferromagnetic relaxation. I. Theory of the relaxation of the uniform precession and the degenerate spectrum in insulators at low temperatures, Physical Review **122**, 791 (1961).

[89] R. Arias and D. L. Mills, Extrinsic contributions to the ferromagnetic resonance response of ultrathin films, Phys Rev B **60**, 7395 (1999).

[90] P. Pincus, Excitation of spin waves in ferromagnets: eddy current and boundary condition effects, Physical Review **118**, 658 (1960).

[91] J. M. Lock, Eddy current damping in thin metallic ferromagnetic films, British Journal of Applied Physics **17**, 1645 (1966).

[92] B. Khodadadi et al., Conductivitylike Gilbert Damping due to Intraband Scattering in Epitaxial Iron, Phys Rev Lett **124**, 157201 (2020).

[93] M. M. Qaid, T. Richter, A. Müller, C. Hauser, C. Ballani, and G. Schmidt, Radiation damping in ferromagnetic resonance induced by a conducting spin sink, Phys Rev B **96**, 184405 (2017).

[94] M. A. W. Schoen, D. Thonig, M. L. Schneider, T. J. Silva, H. T. Nembach, O. Eriksson, O. Karis, and J. M. Shaw, Ultra-low magnetic damping of a metallic ferromagnet, Nat Phys **12**, 839 (2016).

[95] F. Yang and P. Chris Hammel, FMR-driven spin pumping in Y3Fe5O12-based structures, J Phys D Appl Phys **51**, 253001 (2018).

[96] A. Bera, N. Jana, A. Agarwal, and S. Mukhopadhyay, Anisotropic magnetization dynamics in Fe5GeTe2 at room temperature, Phys Rev B **110**, 224401 (2024).

[97] B. A. Bernevig, T. L. Hughes, and S. C. Zhang, Orbitronics: The intrinsic orbital current in p-doped silicon, Phys Rev Lett **95**, 066601 (2005).

[98] S. Zhang and Z. Yang, Intrinsic spin and orbital angular momentum hall effect, Phys Rev Lett **94**, 066602 (2005).

[99] G. Y. Guo, Y. Yao, and Q. Niu, Ab initio calculation of the intrinsic spin hall effect in semiconductors, Phys Rev Lett **94**, 226601 (2005).

[100] G. Sala, Magnetization Dynamics Induced by Spin and Orbital Currents in Ferro- and Ferrimagnets, Thesis, 2022.

[101] S. Lee et al., Efficient conversion of orbital Hall current to spin current for spin-orbit torque switching, Commun Phys **4**, 234 (2021).

[102] G. Sala, H. Wang, W. Legrand, and P. Gambardella, Orbital Hanle Magnetoresistance in a 3d Transition Metal, Phys Rev Lett **131**, 156703 (2023).

[103] I. Lyalin, S. Alikhah, M. Berritta, P. M. Oppeneer, and R. K. Kawakami, Magneto-Optical Detection of the Orbital Hall Effect in Chromium, Phys Rev Lett **131**, 156702 (2023).

[104] Y. G. Choi, D. Jo, K. H. Ko, D. Go, K. H. Kim, H. G. Park, C. Kim, B. C. Min, G. M. Choi, and H. W. Lee, Observation of the orbital Hall effect in a light metal Ti, Nature **619**, 52 (2023).

[105] T. S. Seifert, D. Go, H. Hayashi, R. Rouzegar, F. Freimuth, K. Ando, Y. Mokrousov, and T. Kampfrath, Time-domain observation of ballistic orbital-angular-momentum currents with giant relaxation length in tungsten, Nat Nanotechnol **18**, 1132 (2023).

[106] H. Hayashi, D. Jo, D. Go, T. Gao, S. Haku, Y. Mokrousov, H. W. Lee, and K. Ando, Observation of long-range orbital transport and giant orbital torque, Commun Phys **6**, 32 (2023).

[107] M. Rang and P. J. Kelly, Orbital relaxation length from first-principles scattering calculations, Phys Rev B **109**, 214427 (2024).

[108] T. Tanaka, H. Kontani, M. Naito, T. Naito, D. S. Hirashima, K. Yamada, and J. Inoue, Intrinsic spin Hall effect and orbital Hall effect in 4d and 5d transition metals, Phys Rev B Condens Matter Mater Phys **77**, 165117 (2008).

[109] H. Kontani, T. Tanaka, D. S. Hirashima, K. Yamada, and J. Inoue, Giant orbital hall effect in transition metals: Origin of large spin and anomalous hall effects, Phys Rev Lett **102**, 016601 (2009).

[110] D. Go, D. Jo, C. Kim, and H. W. Lee, Intrinsic Spin and Orbital Hall Effects from Orbital Texture, Phys Rev Lett **121**, 086602 (2018).

[111] D. Jo, D. Go, and H. W. Lee, Gigantic intrinsic orbital Hall effects in weakly spin-orbit coupled metals, Phys Rev B **98**, 214405 (2018).

[112] L. Salemi and P. M. Oppeneer, First-principles theory of intrinsic spin and orbital Hall and Nernst effects in metallic monoatomic crystals, Phys Rev Mater **6**, 095001 (2022).

[113] H. Kontani, T. Tanaka, D. S. Hirashima, K. Yamada, and J. Inoue, Giant intrinsic spin and orbital hall effects in Sr2MO4 (M=Ru, Rh, Mo), Phys Rev Lett **100**, 096601 (2008).

[114] L. M. Canonico, T. P. Cysne, T. G. Rappoport, and R. B. Muniz, Two-dimensional orbital Hall insulators, Phys Rev B **101**, 075429 (2020).

[115] T. P. Cysne, M. Costa, L. M. Canonico, M. B. Nardelli, R. B. Muniz, and T. G. Rappoport, Disentangling Orbital and Valley Hall Effects in Bilayers of Transition Metal Dichalcogenides, Phys Rev Lett **126**, 056601 (2021).

[116] P. Sahu, J. K. Bidika, B. Biswal, S. Satpathy, and B. R. K. Nanda, Emergence of giant orbital Hall and tunable spin Hall effects in centrosymmetric transition metal dichalcogenides, Phys Rev B **110**, 054403 (2024).

[117] D. Go, J. P. Hanke, P. M. Buhl, F. Freimuth, G. Bihlmayer, H. W. Lee, Y. Mokrousov, and S. Blügel, Toward surface orbitronics: Giant orbital magnetism from the orbital Rashba effect at the surface of sp-metals, Sci Rep **7**, 46742 (2017).

[118] H. Hayashi, D. Go, S. Haku, Y. Mokrousov, and K. Ando, Observation of orbital pumping, Nat Electron **7**, 646 (2024).

[119] D. Go, K. Ando, A. Pezo, S. Blügel, A. Manchon, and Y. Mokrousov, Orbital pumping by magnetization dynamics in ferromagnets, Phys Rev B **111**, L140409 (2025).

[120] X. Ning, H. Jaffres, W. Zhao, and A. Manchon, Phenomenology of orbital torque, pumping and mixing conductance in metallic bilayers, ArXiv:2412.08340 (2025).

[121] G. Sala and P. Gambardella, Giant orbital Hall effect and orbital-to-spin conversion in 3d, 5d, and 4f metallic heterostructures, Phys Rev Res **4**, 033037 (2022).

[122] H. An, Y. Kageyama, Y. Kanno, N. Enishi, and K. Ando, Spin-torque generator engineered by natural oxidation of Cu, Nat Commun **7**, 13069 (2016).

[123] S. Ding et al., Harnessing Orbital-to-Spin Conversion of Interfacial Orbital Currents for Efficient Spin-Orbit Torques, Phys Rev Lett **125**, 177201 (2020).

[124] S. Ding, M.-G. Kang, W. Legrand, and P. Gambardella, Orbital Torque in Rare-Earth Transition-Metal Ferrimagnets, Phys Rev Lett **132**, 236702 (2024).

[125] J. Kim, D. Go, H. Tsai, D. Jo, K. Kondou, H.-W. Lee, and Y. Otani, Nontrivial torque generation by orbital angular momentum injection in ferromagnetic-metal/Cu/Al2O3, Phys Rev B **103**, L020407 (2021).

[126] A. Rothschild, N. Am-Shalom, N. Bernstein, M. Meron, T. David, B. Assouline, E. Frohlich, J. Xiao, B. Yan, and A. Capua, Generation of spin currents by the orbital Hall effect in Cu and Al and their measurement by a Ferris-wheel ferromagnetic resonance technique at the wafer level, Phys Rev B **106**, 144415 (2022).

[127] J. Kim et al., Oxide layer dependent orbital torque efficiency in ferromagnet/Cu/oxide heterostructures, Phys Rev Mater **7**, L111401 (2023).

[128] S. Ding, H. Wang, W. Legrand, P. Noël, and P. Gambardella, Mitigation of Gilbert Damping in the CoFe/CuO_x Orbital Torque System, Nano Lett **24**, 10251 (2024).

[129] Q. K. Huang, S. Liu, T. Yang, R. Xie, L. Cai, Q. Cao, W. Lü, L. Bai, Y. Tian, and S. Yan, Current-Induced Magnetization Switching in Light-Metal-Oxide/Ferromagnetic-Metal Bilayers via Orbital Rashba Effect, Nano Lett **23**, 11323 (2023).

[130] F. Liu, B. Liang, J. Xu, C. Jia, and C. Jiang, Giant efficiency of long-range orbital torque in Co/Nb bilayers, Phys Rev B **107**, 054404 (2023).

[131] X. Liu, F. Liu, and C. Jiang, Harnessing orbital Hall effect for efficient orbital torque in light metal vanadium, J Magn Magn Mater **610**, 172585 (2024).

[132] R. Fukunaga, S. Haku, H. Hayashi, and K. Ando, Orbital torque originating from orbital Hall effect in Zr, Phys Rev Res **5**, 023054 (2023).

[133] Y. Marui, M. Kawaguchi, S. Sumi, H. Awano, K. Nakamura, and M. Hayashi, Spin and orbital Hall currents detected via current-induced magneto-optical Kerr effect in V and Pt, Phys Rev B **108**, 144436 (2023).

[134] J. C. Idrobo, J. Rusz, G. Datt, D. Jo, S. Alikhah, D. Muradas, U. Noumbe, M. V. Kamalakar, and P. M. P. M. Oppeneer, Direct observation of nanometer-scale orbital angular momentum accumulation, ArXiv:2403.09269 (2024).

[135] P. Wang et al., Inverse orbital Hall effect and orbitronic terahertz emission observed in the materials with weak spin-orbit coupling, NPJ Quantum Mater **8**, 28 (2023).

[136] Y. Xu, F. Zhang, A. Fert, H. Y. Jaffres, Y. Liu, R. Xu, Y. Jiang, H. Cheng, and W. Zhao, Orbitronics: light-induced orbital currents in Ni studied by terahertz emission experiments, Nat Commun **15**, 2043 (2024).

[137] H. Hayashi and K. Ando, Orbital Hall magnetoresistance in Ni/Ti bilayers, Appl Phys Lett **123**, 172401 (2023).

[138] D. Lee et al., Orbital torque in magnetic bilayers, Nat Commun **12**, 6710 (2021).

[139] H. Sun and G. Vignale, Orbital magnetic moment dynamics and Hanle magnetoresistance in multilayered two-dimensional materials, Phys Rev B **111**, L180408 (2025).

[140] C. González Orellana, Exploring the Frontiers of Ferromagnetic Insulator/Superconductor-Based Devices: Surface Science Developments to Explain Mesoscopic Properties, Thesis, Universidad del País Vasco-Euskal Herriko Unibertsitatea, 2023.

[141] M. Sardela, *Practical Materials Characterization* (Springer New York, 2014).

[142] H. Kiessig, Interferenz von Röntgenstrahlen an dünnen Schichten, Ann Phys **402**, 769 (1931).

[143] I. Neudecker, G. Woltersdorf, B. Heinrich, T. Okuno, G. Gubbiotti, and C. H. Back, Comparison of frequency, field, and time domain ferromagnetic resonance methods, J Magn Magn Mater **307**, 148 (2006).

[144] J. Shan, P. Bougiatioti, L. Liang, G. Reiss, T. Kuschel, and B. J. Van Wees, Nonlocal magnon spin transport in NiFe2O4 thin films, Appl Phys Lett **110**, 132406 (2017).

[145] W. Xing, L. Qiu, X. Wang, Y. Yao, Y. Ma, R. Cai, S. Jia, X. C. Xie, and W. Han, Magnon Transport in Quasi-Two-Dimensional van der Waals Antiferromagnets, Phys Rev X **9**, 011026 (2019).

[146] S. Qi et al., Giant electrically tunable magnon transport anisotropy in a van der Waals antiferromagnetic insulator, Nat Commun **14**, 2526 (2023).

[147] D. K. De Wal, A. Iwens, T. Liu, P. Tang, G. E. W. Bauer, and B. J. Van Wees, Long-distance magnon transport in the van der Waals antiferromagnet CrPS4, Phys Rev B **107**, L180403 (2023).

[148] P. Yuan, B. Martín-García, E. Modin, M. X. Aguilar-Pujol, F. Casanova, and L. E. Hueso, Unconventional Magnon Transport in Antiferromagnet NiPS3 Induced by an Anisotropic Spin-Flop Transition, Nano Lett **25**, 5350 (2025).

[149] K. Mallick, A. A. Wagh, A. Ionescu, C. H. W. Barnes, and P. S. Anil Kumar, Magnetoresistance effects in Pt/EuO1-x, Appl Phys Lett **116**, 202405 (2020).

[150] P. Rosenberger, M. Opel, S. Geprägs, H. Huebl, R. Gross, M. Müller, and M. Althammer, Quantifying the spin mixing conductance of EuO/W heterostructures by spin Hall magnetoresistance experiments, Appl Phys Lett **118**, 192401 (2021).

[151] J. M. Gomez-Perez et al., Strong Interfacial Exchange Field in a Heavy Metal/Ferromagnetic Insulator System Determined by Spin Hall Magnetoresistance, Nano Lett **20**, 6815 (2020).

[152] T. R. McGuire, B. E. Argyle, M. W. Shafer, and J. S. Smart, Magnetic properties of some divalent europium compounds, J Appl Phys **34**, 1345 (1963).

[153] L. Passell, O. W. Dietrich, and J. Als-Nielsen, Neutron scattering from the Heisenberg ferromagnets EuO and EuS. I. The exchange interactions, Phys Rev B **14**, 4897 (1976).

[154] K. Y. Ahn, M. W. Shafer, and T. J. Watson, Preparation and properties of eus films and effects of fe doping, IEEE Trans Magn **7**, 394 (1971).

[155] P. Wei et al., Strong interfacial exchange field in the graphene/EuS heterostructure, Nat Mater **15**, 711 (2016).

[156] A. Hijano et al., Coexistence of superconductivity and spin-splitting fields in superconductor/ferromagnetic insulator bilayers of arbitrary thickness, Phys Rev Res **3**, 023131 (2021).

[157] J. S. Moodera, X. Hao, G. A. Gibson, and R. Meservey, Electron-spin polarization in tunnel junctions in zero applied field with ferromagnetic EuS barriers, Phys Rev Lett **61**, 637 (1988).

[158] X. Hao, J. S. Moodera, and R. Meservey, Spin-filter effect of ferromagnetic europium sulfide tunnel barriers, Phys Rev B **42**, 8235 (1990).

[159] E. Strambini et al., Superconducting spintronic tunnel diode, Nat Commun **13**, 2431 (2022).

[160] Y. Liu et al., Semiconductor-Ferromagnetic Insulator-Superconductor Nanowires: Stray Field and Exchange Field, Nano Lett **20**, 456 (2020).

[161] G. De Simoni, E. Strambini, J. S. Moodera, F. S. Bergeret, and F. Giazotto, Toward the Absolute Spin-Valve Effect in Superconducting Tunnel Junctions, Nano Lett **18**, 6369 (2018).

[162] S. Diesch, P. Machon, M. Wolz, C. Sürgers, D. Beckmann, W. Belzig, and E. Scheer, Creation of equal-spin triplet superconductivity at the Al/EuS interface, Nat Commun **9**, 5248 (2018).

[163] E. Strambini, V. N. Golovach, G. De Simoni, J. S. Moodera, F. S. Bergeret, and F. Giazotto, Revealing the magnetic proximity effect in EuS/Al bilayers through superconducting tunneling spectroscopy, Phys Rev Mater **1**, 054402 (2017).

[164] S. Vaitiekėnas, Y. Liu, P. Krogstrup, and C. M. Marcus, Zero-bias peaks at zero magnetic field in ferromagnetic hybrid nanowires, Nat Phys **17**, 43 (2021).

[165] Y. Liu et al., Coherent Epitaxial Semiconductor-Ferromagnetic Insulator InAs/EuS Interfaces: Band Alignment and Magnetic Structure, ACS Appl Mater Interfaces **12**, 8780 (2020).

[166] Z. Geng et al., Superconductor-ferromagnet hybrids for non-reciprocal electronics and detectors, Supercond Sci Technol 123001 (2023).

[167] E. Sagasta, Y. Omori, M. Isasa, M. Gradhand, L. E. Hueso, Y. Niimi, Y. Otani, and F. Casanova, Tuning the spin Hall effect of Pt from the moderately dirty to the superclean regime, Phys Rev B **94**, 060412 (2016).

[168] J. M. Gómez Pérez, Spin Transport in Magnetic Insulator/Heavy Metal Heterostructures, Thesis, Universidad del País Vasco-Euskal Herriko Unibertsitatea, 2020.

[169] H. Nakayama et al., Spin Hall Magnetoresistance Induced by a Nonequilibrium Proximity Effect, Phys Rev Lett **110**, 206601 (2013).

[170] M. Isasa, A. Bedoya-Pinto, S. Vélez, F. Golmar, F. Sánchez, L. E. Hueso, J. Fontcuberta, and F. Casanova, Spin Hall magnetoresistance at Pt/CoFe2O4 interfaces and texture effects, Appl Phys Lett **105**, 142402 (2014).

[171] R. Schlitz, S. Vélez, A. Kamra, C. H. Lambert, M. Lammel, S. T. B. Goennenwein, and P. Gambardella, Control of Nonlocal Magnon Spin Transport via Magnon Drift Currents, Phys Rev Lett **126**, 257201 (2021).

[172] M. Schreier, N. Roschewsky, E. Dobler, S. Meyer, H. Huebl, R. Gross, and S. T. B. Goennenwein, Current heating induced spin Seebeck effect, Appl Phys Lett **103**, 242404 (2013).

[173] J. Shan, L. J. Cornelissen, N. Vlietstra, J. Ben Youssef, T. Kuschel, R. A. Duine, and B. J. Van Wees, Influence of yttrium iron garnet thickness and heater opacity on the nonlocal transport of electrically and thermally excited magnons, Phys Rev B **94**, 174437 (2016).

[174] X. J. Zhou, G. Y. Shi, J. H. Han, Q. H. Yang, Y. H. Rao, H. W. Zhang, L. L. Lang, S. M. Zhou, F. Pan, and C. Song, Lateral transport properties of thermally excited magnons in yttrium iron garnet films, Appl Phys Lett **110**, 062407 (2017).

[175] L. J. Cornelissen, J. Shan, and B. J. van Wees, Temperature dependence of the magnon spin diffusion length and magnon spin conductivity in the magnetic insulator yttrium iron garnet, Phys Rev B **94**, 180402 (2016).

[176] S. T. B. Goennenwein, R. Schlitz, M. Pernpeintner, K. Ganzhorn, M. Althammer, R. Gross, and H. Huebl, Non-local magnetoresistance in YIG/Pt nanostructures, Appl Phys Lett **107**, 172405 (2015).

[177] K. Oyanagi et al., Paramagnetic spin Hall magnetoresistance, Phys Rev B **104**, 134428 (2021).

[178] X. P. Zhang, F. S. Bergeret, and V. N. Golovach, Theory of Spin Hall Magnetoresistance from a Microscopic Perspective, Nano Lett **19**, 6330 (2019).

[179] H. Adachi, Y. Yamamoto, and M. Ichioka, Spin Seebeck effect in a simple ferromagnet near T c: A Ginzburg-Landau approach, J Phys D Appl Phys **51**, 144001 (2018).

[180] G. X. Miao and J. S. Moodera, Controlling magnetic switching properties of EuS for constructing double spin filter magnetic tunnel junctions, Appl Phys Lett **94**, 182504 (2009).

[181] T. Kikkawa, K. I. Uchida, S. Daimon, Z. Qiu, Y. Shiomi, and E. Saitoh, Critical suppression of spin Seebeck effect by magnetic fields, Phys Rev B Condens Matter Mater Phys **92**, 064413 (2015).

[182] K. Oyanagi, T. Kikkawa, and E. Saitoh, Magnetic field dependence of the nonlocal spin Seebeck effect in Pt/YIG/Pt systems at low temperatures, AIP Adv **10**, 015031 (2020).

[183] T. Kikkawa, K. I. Uchida, S. Daimon, and E. Saitoh, Complete suppression of longitudinal spin Seebeck effect by frozen magnetization dynamics in Y3Fe5O12, J Physical Soc Japan **85**, 065003 (2016).

[184] L. J. Cornelissen and B. J. Van Wees, Magnetic field dependence of the magnon spin diffusion length in the magnetic insulator yttrium iron garnet, Phys Rev B **93**, 020403 (2016).

[185] J. Gao, C. H. Lambert, R. Schlitz, M. Fiebig, P. Gambardella, and S. Vélez, Magnon transport and thermoelectric effects in ultrathin Tm3Fe5 O12 /Pt nonlocal devices, Phys Rev Res **4**, 043214 (2022).

[186] T. B. Noack et al., Spin Seebeck effect and ballistic transport of quasi-acoustic magnons in room-temperature yttrium iron garnet films, J Phys D Appl Phys **51**, 234003 (2018).

[187] E. Chavez-Angel, R. A. Zarate, S. Fuentes, E. J. Guo, M. Kläui, and G. Jakob, Reconstruction of an effective magnon mean free path distribution from spin Seebeck measurements in thin films, New J Phys **19**, 013011 (2017).

[188] A. Kehlberger et al., Length Scale of the Spin Seebeck Effect, Phys Rev Lett **115**, 096602 (2015).

[189] U. Ritzmann, D. Hinzke, and U. Nowak, Propagation of thermally induced magnonic spin currents, Phys Rev B **89**, 024409 (2014).

[190] K. R. Jeon, J. C. Jeon, X. Zhou, A. Migliorini, J. Yoon, and S. S. P. Parkin, Giant transition-state quasiparticle spin-Hall effect in an exchange-spin-split superconductor detected by nonlocal magnon spin transport, ACS Nano **14**, 15874 (2020).

[191] L. G. Johnsen, H. T. Simensen, A. Brataas, and J. Linder, Magnon Spin Current Induced by Triplet Cooper Pair Supercurrents, Phys Rev Lett **127**, 207001 (2021).

[192] F. Giazotto and F. S. Bergeret, Very large thermal rectification in ferromagnetic insulator-based superconducting tunnel junctions, Appl Phys Lett **116**, 192601 (2020).

[193] F. Giazotto, P. Solinas, A. Braggio, and F. S. Bergeret, Ferromagnetic-Insulator-Based Superconducting Junctions as Sensitive Electron Thermometers, Phys Rev Appl **4**, 044016 (2015).

[194] Z. Geng, A. P. Helenius, T. T. Heikkilä, and I. J. Maasilta, Superconductor-Ferromagnet Tunnel Junction Thermoelectric Bolometer and Calorimeter with a SQUID Readout, J Low Temp Phys **199**, 585 (2020).

[195] P. Machon, M. Eschrig, and W. Belzig, Giant thermoelectric effects in a proximity-coupled superconductor- ferromagnet device, New J Phys **16**, 073002 (2014).

[196] P. K. Muduli, M. Kimata, Y. Omori, T. Wakamura, S. P. Dash, and Y. Otani, Detection of the interfacial exchange field at a ferromagnetic insulator-nonmagnetic metal interface with pure spin currents, Phys Rev B **98**, 024416 (2018).

[197] R. C. LeCraw, E. G. Spencer, and C. S. Porter, Ferromagnetic resonance line width in yttrium iron garnet single crystals, Physical Review **110**, 1311 (1958).

[198] S. Martínez-Losa Del Rincón, I. Gimeno, J. Pérez-Bailón, V. Rollano, F. Luis, D. Zueco, and M. J. Martínez-Pérez, Measuring the Magnon-Photon Coupling in Shaped Ferromagnets: Tuning of the Resonance Frequency, Phys Rev Appl **19**, 014002 (2023).

[199] S. Guo, B. McCullian, P. Chris Hammel, and F. Yang, Low damping at few-K temperatures in Y3Fe5O12 epitaxial films isolated from Gd3Ga5O12 substrate using a diamagnetic Y3Sc2.5Al2.5O12 spacer, J Magn Magn Mater **562**, 169795 (2022).

[200] L. Mihalceanu, V. I. Vasyuchka, D. A. Bozhko, T. Langner, A. Y. Nechiporuk, V. F. Romanyuk, B. Hillebrands, and A. A. Serga, Temperature-dependent relaxation of dipole-exchange magnons in yttrium iron garnet films, Phys Rev B **97**, 214405 (2018).

[201] S. Knauer et al., Propagating spin-wave spectroscopy in a liquid-phase epitaxial nanometer-thick YIG film at millikelvin temperatures, J Appl Phys **133**, 143905 (2023).

[202] E. G. Spencer, R. C. Lecraw, and A. M. Clogston, Low-temperature line-width maximum in yttrium iron garnet, Phys Rev Lett **3**, 32 (1959).

[203] C. L. Jermain, S. V. Aradhya, N. D. Reynolds, R. A. Buhrman, J. T. Brangham, M. R. Page, P. C. Hammel, F. Y. Yang, and D. C. Ralph, Increased low-temperature damping in yttrium iron garnet thin films, Phys Rev B **95**, 174411 (2017).

[204] Y. Zhao, Q. Song, S. H. Yang, T. Su, W. Yuan, S. S. P. Parkin, J. Shi, and W. Han, Experimental Investigation of Temperature-Dependent Gilbert Damping in Permalloy Thin Films, Sci Rep **6**, 22890 (2016).

[205] S. Büttner and M. März, Profitability of low-temperature power electronics and potential applications, Cryogenics (Guildf) **121**, 103392 (2022).

[206] R. K. Kirschman, Low-temperature electronics, IEEE Circuits and Devices Magazine **6**, 12 (1990).

[207] J. Linder and J. W. A. Robinson, Superconducting spintronics, Nat Phys **11**, 307 (2015).

[208] K. Chen and D. P. Landau, Spin-dynamics study of the dynamic critical behavior of the three-dimensional classical Heisenberg ferromagnet, Phys Rev B **49**, 3266 (1994).

[209] H. G. Bohn, A. Kollmar, and W. Zinn, Spin dynamics in the cubic Heisenberg ferromagnet EuS, Phys Rev B **30**, 6504 (1984).

[210] R. R. Bartkowski, Spin-wave relaxation in EuS, Phys Rev B **2**, 3791 (1970).

[211] S. Von Molnar and A. W. Lawson, Ferromagnetic and paramagnetic resonance in EuS, Physical Review **139**, A1598 (1965).

[212] M. C. Franzblau, G. E. Everett, and A. W. Lawson, Temperature dependence of the ferromagnetic resonance linewidth of europium sulfide, J Appl Phys **38**, 4462 (1967).

[213] Y. Hou et al., Ubiquitous Superconducting Diode Effect in Superconductor Thin Films, Phys Rev Lett **131**, 027001 (2023).

[214] P. Wei, F. Katmis, B. A. Assaf, H. Steinberg, P. Jarillo-Herrero, D. Heiman, and J. S. Moodera, Exchange-coupling-induced symmetry breaking in topological insulators, Phys Rev Lett **110**, 186807 (2013).

[215] M. Haidar, M. Ranjbar, M. Balinsky, R. K. Dumas, S. Khartsev, and J. Åkerman, Thickness- and temperature-dependent magnetodynamic properties of yttrium iron garnet thin films, J Appl Phys **117**, 117D119 (2015).

[216] S. He and C. Panagopoulos, A broadband ferromagnetic resonance dipper probe for magnetic damping measurements from 4.2 K to 300 K, Review of Scientific Instruments **87**, 043100 (2016).

[217] S. Azzawi, A. T. Hindmarch, and D. Atkinson, Magnetic damping phenomena in ferromagnetic thin-films and multilayers, J Phys D Appl Phys **50**, 473001 (2017).

[218] I. Neudecker, G. Woltersdorf, B. Heinrich, T. Okuno, G. Gubbiotti, and C. H. Back, Comparison of frequency, field, and time domain ferromagnetic resonance methods, J Magn Magn Mater **307**, (2006).

[219] I. S. Maksymov and M. Kostylev, *Broadband Stripline Ferromagnetic Resonance Spectroscopy of Ferromagnetic Films, Multilayers and Nanostructures*, Physica E: Low-Dimensional Systems and Nanostructures.

[220] C. Kittel, On the theory of ferromagnetic resonance absorption, Physical Review **73**, (1948).

[221] W. Zinn, Microscopic studies of magnetic properties and interactions recent results on europium-monochalcogenides, J Magn Magn Mater **3**, 23 (1976).

[222] P. Tischer, Ferromagnetic Domains in EuS Investigated by Low-Temperature Lorentz Microscopy, IEEE Trans Magn **9**, 9 (1973).

[223] A. Y. Sipatov, C. H. W. Swüste, H. J. M. Swagten, and W. J. M. de Jonge, Ferromagnetic transition in eus-pbs multilayers, Phys Rev B Condens Matter Mater Phys **60**, 15220 (1999).

[224] R. Świrkowicz and T. Story, Spin waves and temperature dependence of magnetization in strained EuS films, Journal of Physics Condensed Matter **12**, 8511 (2000).

[225] B. Heinrich, J. F. Cochran, and R. Hasegawa, FMR linebroadening in metals due to two-magnon scattering, J Appl Phys **57**, 3690 (1985).

[226] S. S. Kalarickal, P. Krivosik, M. Wu, C. E. Patton, M. L. Schneider, P. Kabos, T. J. Silva, and J. P. Nibarger, Ferromagnetic resonance linewidth in metallic thin films: Comparison of measurement methods, J Appl Phys **99**, 093909 (2006).

[227] E. Schlömann, Inhomogeneous broadening of ferromagnetic resonance lines, Physical Review **182**, 632 (1969).

[228] K. Lenz, H. Wende, W. Kuch, K. Baberschke, K. Nagy, and A. Jánossy, Two-magnon scattering and viscous Gilbert damping in ultrathin ferromagnets, Phys Rev B Condens Matter Mater Phys **73**, 144424 (2006).

[229] M. G. Balinskii, V. V. Danilov, A. Y. Nechiporuk, and V. M. Talalaevskii, Damping of magnetostatic spin waves in substrates, Radiophysics and Quantum Electronics **29**, 954 (1986).

[230] Y. Li et al., Strong coupling between magnons and microwave photons in on-chip ferromagnet-superconductor thin-film devices, Phys Rev Lett **123**, (2019).

[231] Y. Wei, W. Zhang, B. Lv, X. Xu, S. Xi, and Z. Ma, Ultralow magnetic damping of a common metallic ferromagnetic film, Sci Adv **7**, eabc5053 (2021).

[232] S. Knauer et al., Propagating spin-wave spectroscopy in a liquid-phase epitaxial nanometer-thick YIG film at millikelvin temperatures, J Appl Phys **133**, 143905 (2023).

[233] C. Bilzer, T. Devolder, J. von Kim, G. Counil, C. Chappert, S. Cardoso, and P. P. Freitas, Study of the dynamic magnetic properties of soft CoFeB films, J Appl Phys **100**, (2006).

[234] J. Sinova, S. O. Valenzuela, J. Wunderlich, C. H. Back, and T. Jungwirth, Spin Hall effects, Rev Mod Phys **87**, 1213 (2015).

[235] J. E. Hirsch, Spin Hall Effect, Phys Rev Lett **83**, 1834 (1999).

[236] A. Manchon, J. Železný, I. M. Miron, T. Jungwirth, J. Sinova, A. Thiaville, K. Garello, and P. Gambardella, Current-induced spin-orbit torques in ferromagnetic and antiferromagnetic systems, Rev Mod Phys **91**, 035004 (2019).

[237] Q. Shao et al., Roadmap of Spin-Orbit Torques, IEEE Trans Magn **57**, 1 (2021).

[238] A. Fert, R. Ramesh, V. Garcia, F. Casanova, and M. Bibes, Electrical control of magnetism by electric field and current-induced torques, Rev Mod Phys **96**, 015005 (2024).

[239] D. C. Vaz et al., Voltage-based magnetization switching and reading in magnetoelectric spin-orbit nanodevices, Nat Commun **15**, 1902 (2024).

[240] H. L. Wang, C. H. Du, Y. Pu, R. Adur, P. C. Hammel, and F. Y. Yang, Scaling of spin hall angle in 3d, 4d, and 5d metals from Y3Fe5 O12 /metal spin pumping, Phys Rev Lett **112**, 197201 (2014).

[241] D. D. Sarma, Nature of dependence of spin-orbit splittings on atomic number, Proceedings of the Indian Academy of Sciences - Chemical Sciences **90**, 19 (1981).

[242] Y. Niimi and Y. Otani, Reciprocal spin Hall effects in conductors with strong spin-orbit coupling: A review, Reports on Progress in Physics **78**, 124501 (2015).

[243] O. Mosendz, V. Vlaminck, J. E. Pearson, F. Y. Fradin, G. E. W. Bauer, S. D. Bader, and A. Hoffmann, Detection and quantification of inverse spin Hall effect from spin pumping in permalloy/normal metal bilayers, Phys Rev B Condens Matter Mater Phys **82**, 214403 (2010).

[244] M. Morota, Y. Niimi, K. Ohnishi, D. H. Wei, T. Tanaka, H. Kontani, T. Kimura, and Y. Otani, Indication of intrinsic spin Hall effect in 4d and 5d transition metals, Phys Rev B Condens Matter Mater Phys **83**, 174405 (2011).

[245] Y. Maruyama, R. Ohshima, E. Shigematsu, Y. Ando, and M. Shiraishi, Modulation of Hanle magnetoresistance in an ultrathin platinum film by ionic gating, Applied Physics Express **16**, 023004 (2023).

[246] H. Wu, X. Zhang, C. H. Wan, B. S. Tao, L. Huang, W. J. Kong, and X. F. Han, Hanle magnetoresistance: The role of edge spin accumulation and interfacial spin current, Phys Rev B **94**, 174407 (2016).

[247] D. Go, D. Jo, H. W. Lee, M. Kläui, and Y. Mokrousov, Orbitronics: Orbital currents in solids, EPL **135**, 37001 (2021).

[248] G. Bergmann, Weak localization in thin films. a time-of-flight experiment with conduction electrons, Phys Rep **107**, 1 (1984).

[249] C. Barone et al., Nonequilibrium fluctuations as a distinctive feature of weak localization, Sci Rep **5**, 10705 (2015).

[250] S. Maekawa and H. Fukuyama, Magnetoresistance in Two-Dimensional Disordered Systems: Effects of Zeeman Splitting and Spin-Orbit Scattering, J Physical Soc Japan **50**, 2516 (1981).

[251] D. Go, H.-W. Lee, P. M. Oppeneer, S. Blügel, and Y. Mokrousov, First-principles calculation of orbital Hall effect by Wannier interpolation: Role of orbital dependence of the anomalous position, Phys Rev B **109**, 174435 (2024).

[252] M. Rang and P. J. Kelly, Orbital Hall effect in transition metals from first-principles scattering calculations, Phys Rev B **111**, 125121 (2025).

[253] C. Hahn, G. De Loubens, O. Klein, M. Viret, V. V. Naletov, and J. Ben Youssef, Comparative measurements of inverse spin Hall effects and

magnetoresistance in YIG/Pt and YIG/Ta, Phys Rev B Condens Matter Mater Phys **87**, 174417 (2013).

[254] M. B. Jungfleisch, A. V. Chumak, A. Kehlberger, V. Lauer, D. H. Kim, M. C. Onbasli, C. A. Ross, M. Kläui, and B. Hillebrands, Thickness and power dependence of the spin-pumping effect in Y3Fe5 O12 /Pt heterostructures measured by the inverse spin Hall effect, Phys Rev B Condens Matter Mater Phys **91**, 134407 (2015).

[255] C. Du, H. Wang, F. Yang, and P. C. Hammel, Systematic variation of spin-orbit coupling with d -orbital filling: Large inverse spin Hall effect in 3d transition metals, Phys Rev B Condens Matter Mater Phys **90**, 140407 (2014).

[256] Y. T. Chen, S. Takahashi, H. Nakayama, M. Althammer, S. T. B. Goennenwein, E. Saitoh, and G. E. W. Bauer, Theory of spin Hall magnetoresistance (SMR) and related phenomena, Journal of Physics Condensed Matter **28**, 103004 (2016).

[257] T. Wang, W. Wang, Y. Xie, M. A. Warsi, J. Wu, Y. Chen, V. O. Lorenz, X. Fan, and J. Q. Xiao, Large spin Hall angle in vanadium film, Sci Rep **7**, 1306 (2017).

[258] S. Dushenko, M. Hokazono, K. Nakamura, Y. Ando, T. Shinjo, and M. Shiraishi, Tunable inverse spin Hall effect in nanometer-thick platinum films by ionic gating, Nat Commun **9**, 3118 (2018).

[259] P. Tang and G. E. W. Bauer, Role of Disorder in the Intrinsic Orbital Hall Effect, Phys Rev Lett **133**, 186302 (2024).

[260] T. Valet and R. Raimondi, Quantum kinetic theory of the linear response for weakly disordered multiband systems, Phys Rev B **111**, L041118 (2025).

[261] T. Valet, H. Jaffrès, V. Cros, and R. Raimondi, Quantum Kinetic Anatomy of Electron Angular Momenta Edge Accumulation, ArXiv:2507.06771 (2025).

[262] V. Palenskis and E. Žitkevičius, Phonon Mediated Electron-Electron Scattering in Metals, World Journal of Condensed Matter Physics **08**, 115 (2018).

[263] X. Ning, A. Pezo, K.-W. Kim, W. Zhao, K.-J. Lee, and A. Manchon, Orbital Diffusion, Polarization, and Swapping in Centrosymmetric Metals, Phys Rev Lett **134**, 026303 (2025).

[264] J. Ingla-Aynés, Y. Hou, S. Wang, E.-D. Chu, O. A. Mukhanov, P. Wei, and J. S. Moodera, Efficient superconducting diodes and rectifiers for quantum circuitry, Nat Electron **8**, 411 (2025).

[265] C. I. L. de Araujo, P. Virtanen, M. Spies, C. González-Orellana, S. Kerschbaumer, M. Ilyn, C. Rogero, T. T. Heikkilä, F. Giazotto, and E. Strambini, Superconducting spintronic heat engine, Nat Commun **15**, 4823 (2024).

[266] I. Kolokolov, V. S. L'vov, and A. Pomyalov, Precritical anomalous scaling and magnetization temperature dependence in cubic ferromagnetic crystals, Phys Rev B **111**, 104433 (2025).

[267] M. Zeer, D. Go, M. Kläui, W. Wulfhekel, S. Blügel, and Y. Mokrousov, Orbital torques and orbital pumping in two-dimensional rare-earth dichalcogenides, ArXiv:2502.00449 (2025).

List of Publications

This thesis is based on the following publications:

- Magnon currents excited by the spin Seebeck effect in ferromagnetic EuS thin films. **M. Xochitl Aguilar-Pujol***, Sara Catalano*, Carmen González-Orellana, Witold Skowronski, Juan M. Gómez-Pérez, Maxim Ilyn, Celia Rogero, Marco Gobbi, Luis E. Hueso and Fèlix Casanova. *Phys. Rev. B* **108**, 224420 (2023).

  * Equal contribution

  (Chapter 4)

- Gilbert damping in EuS thin films by ferromagnetic resonance spectroscopy. **M. Xochitl Aguilar-Pujol**, Sara Catalano, David Caldevilla, Samuel Kerschbaumer, Kamil Staszek, Maxim Ilyn, Marco Gobbi, Celia Rogero, Luis E. Hueso, Witold Skowroński and Fèlix Casanova. Submitted to *Appl. Phys. Lett*.

  (Chapter 5)

- Orbital Hall conductivity and orbital diffusion length of Vanadium thin films by Hanle magnetoresistance. **M. Xochitl Aguilar-Pujol**, Isabel C. Arango, Eoin Dolan, You Ba, Marco Gobbi, Luis E. Hueso, and Fèlix Casanova. Accepted in Newton. arXiv:2506.06546 (2025).

  (Chapter 6)

Other publications:

- Spin Hall magnetoresistance effect from a disordered interface. Sara Catalano, Juan M. Gomez-Perez, **M. Xochitl Aguilar-**

Pujol, Andrey Chuvilin, Marco Gobbi, Luis E. Hueso, and Fèlix Casanova. *ACS Applied Materials & Interfaces* **14**, 8598 (2022)

- Interfacial Magnetic Features of La_2CoMnO_6/Pt Bilayers Studied by Using Spin Hall Magnetoresistance Sergi Martín-Rio, Carlos Frontera, Juan M. Gómez-Pérez, **Montserrat X. Aguilar-Pujol**, Sara Catalano, Jaume Gázquez, Fèlix Casanova, Lluis Balcells, Alberto Pomar, and Benjamin Martinez. *Advanced Materials Interfaces* **9**, 2201171 (2022).

- Unconventional magnon transport in antiferromagnet $NiPS_3$ induced by an anisotropic spin-flop transition Peisen Yuan, Beatriz Martín-García, Evgeny Modin, **M. Xochitl Aguilar-Pujol**, Fèlix Casanova, and Luis E. Hueso. *Nano Letters* **25**, 5350 (2025).

Acknowledgements

First of all, I would like to acknowledge my supervisors, Fèlix Casanova and Luis Hueso, for offering me the wonderful opportunity to continue my scientific career in their research group. In particular, I would like to thank Fèlix for all the patience and time he has dedicated to me.

I would also like to thank Sara Catalano for being my guide during my first period at nanoGUNE. I learned a lot from you about science, writing, equipment, and life. Another thanks to Witold Skowroński for showing me so much about magnetization dynamics and ferromagnetic resonance experiments. Of course, special thanks to Ralph and Roger for their help during difficult days in the lab and for all the knowledge they shared. Many thanks as well to Eli for always helping with administrative tasks and computer issues. I sincerely thank all the members of the Nanodevices Group, whom I had the pleasure to meet and share workspace with. Also, thanks to Mari, Yaiza, and Jone for helping me practise my conference presentations.

Finally, I would like to express my gratitude to those who helped me reach this point. Special thanks to Alberto Bollero, who decided to send my CV to Luis Hueso because he liked it and thought it would be a good place for me. Sometimes we choose; other times, destiny does.

My sincere thanks also go to Carlos Prieto, who gave me my first opportunity in science by allowing me to walk once more through the corridors I knew from my childhood.

Lastly, I would like to thank my family, my mum and brother, and also my father, who continues to inspire me, for showing me that even when life is difficult, there is always a reward. I also wish to thank my husband for encouraging me to come to Donostia, and to Nathan, whose questions about the PPMS at home always made me smile.